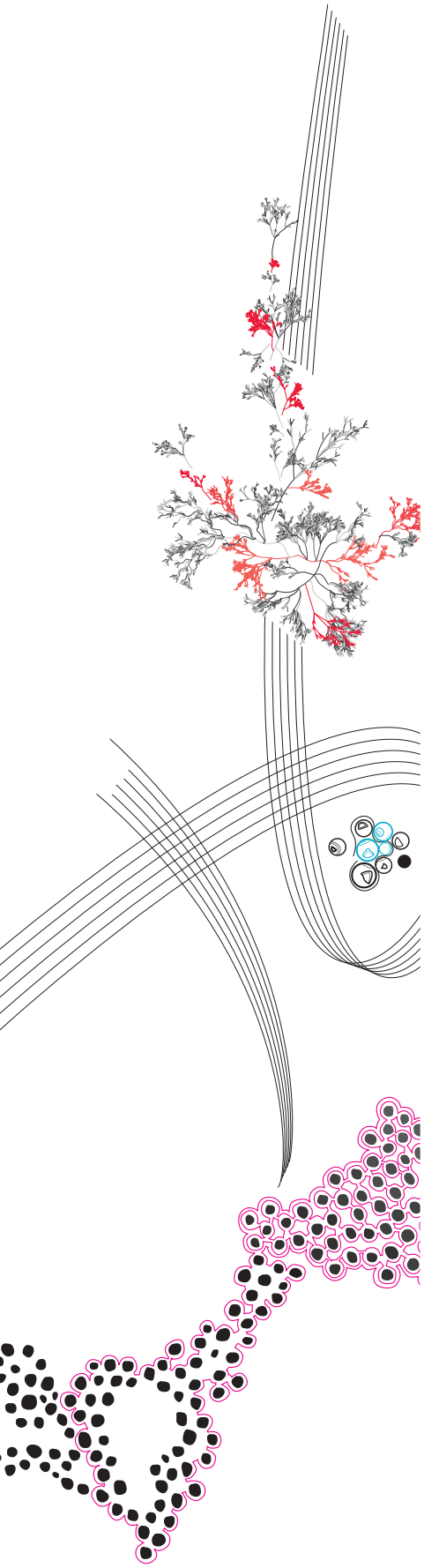

Master Thesis

Towards a testing standard for intralaminar fracture toughness of CFRPs

Determining the longitudinal Mode I intralaminar fracture toughness and crack growth consistency of a Continuous Fiber Reinforced Polymer with a Linear Elastic Fracture Mechanics (LEFM) approach

D. Uil

Supervisor: Dr. Ir. L. Warnet

July, 2023

Production Technology Group,
Faculty of Engineering Technology,
Mechanical Engineering

UNIVERSITY OF TWENTE.

Determining the longitudinal Mode I intralaminar fracture toughness and crack growth consistency of a Continuous Fiber Reinforced Polymer with a Linear Elastic Fracture Mechanics (LEFM) approach

This document concerns the master thesis of Dennis Uil belonging to the High Tech Systems & Materials (HTSM) specialization of the Mechanical Engineering (ME) master. The project has been performed within the University of Twente, more specifically, the Production Technology (PT) department.

Acknowledgements

After 8 months of reading, experimenting, testing, adjusting and, most of all, learning, the time has now come to conclude this research and graduate from the University of Twente. These last few months have made me realize the importance of persistence even though the end seems so far away, it is always nearer than it appears. I would like to thank a few people that made this piece of research possible, and with whom I enjoyed my time during the graduation phase.

First, I would like to thank my supervisor Dr. L. Warnet for the possibility of combining multiple courses towards one interesting topic, being composite materials. I also would like to thank him for his guidance, the helpful insights and overall supervision over the last few months. Our weekly meetings have directed me towards the research that lies in front of you right now. Furthermore, I'd like to thank BSc. N. Helthuis for his help and knowledge in the laboratory.

Next, I'd like to thank Arthur and Friso. Our daily struggle towards the same goal of graduation within a reasonable time has made it much more easier to accomplish and, above all, more enjoyable. Next to them, I'd like to thank other members of the PT group, providing me with useful feedback and ideas during the monthly presentation sessions. I felt at home within the PT group due to the overall sober mindset which is something I share as well.

Lastly, I'd like to thank my family and friends. I cherish your love, support and effort in keeping me motivated at all times.

Dennis Uil

July, 2023

Summary

Continuous Fiber Reinforced Polymers (CFRPs) are layered structures and made of highly anisotropic thin plies, leading to complex, often interconnected damage mechanisms. One of the early damage mechanisms concerns the inter layer cohesion, leading to so-called delamination. It is recognised that these cracks are initiated by matrix cracks, running parallel to the fibers in the adjacent layer. This failure mechanism, related to the delamination failure, is longitudinal intralaminar cracking (also known as transverse cracking) which usually follows the extent of delamination.

Though the mechanical characterisation of delamination is well described and even supported by standard testing methods, that of the longitudinal intralaminar cracking is not. The objective of this research is to propose a testing method and protocol for the experimental evaluation of Mode I longitudinal intralaminar fracture toughness and crack propagation resistance of CFRPs under quasi-static loading. This, similarly to, and partly based on the existing testing standards for the fracture toughness of polymers (ISO 13586) and the standard for determining interlaminar fracture toughness of CFRPs (ISO 15024). The addition of this new test would add on these existing methods, necessary to, for example, model damage evolution in composite structures and determine/predict premature failure.

Several test setups were analysed for their suitability whereafter a Single Edge Notched Bending (SENB) setup was chosen. Furthermore, the applicability of a Linear Elastic Fracture Mechanics (LEFM) approach has been researched, whereafter ISO 13586 was taken as guideline. The dimension parameters of these SENB specimens have been experimentally determined by data-, literature- and FEM analysis. Regarding the preparation of these specimens, experimental methods have resulted in recommendations for: specimen machining, pre-crack cutting using a microtome, pre-crack depth, and microscopic analysis by constantly iterating between testing the setup and designing the setup. Furthermore, an algorithm using a camera to track the crack tip position in LabVIEW was designed, whereafter the determination of crack propagation resistance was done using an energy analysis method and a corrected compliance based method. Based on these experimental methods, a testing protocol has been written with clear formulation, forming a guidance in the longitudinal Mode I intralaminar fracture toughness testing of Continuous Fiber Reinforced Polymers.

Ten specimens were tested on fracture toughness and on crack propagation resistance as part of a Round Robin. The use of a LabVIEW algorithm for crack tip tracking and an adapted microtome for pre-crack cutting ensure high precision and reproducibility. The critical Mode I energy release rate at initiation G_{Ic} has a Relative Standard Deviation (%STD) of $\sim$10%, with a %STD of 1.59% on the precision. Next, the critical stress intensity factor at initiation K_{Ic} has a %STD of $\sim$6%, with a %STD of 0.74% on the precision. Furthermore, the pre-crack Notch Tip Diameter (NTD) and maximum force reached have a %STD of $\sim$23% and $\sim$6% respectively, with the latter having a %STD of 0.03% on the precision. These results, having a low variance, show a good repeatability of the test methodology used.

Assignment description

The objective of this project is to propose a protocol for the experimental evaluation of the intralaminar fracture toughness of continuous fiber reinforced polymers. The addition of such a testing method would add to existing methods on interlaminar fracture toughness, necessary to for example model damage evolution in composite structures. The project will include a literature research on possible testing geometry and corresponding analysis to quantify the toughness. Such an analysis may require the use of numerical tools. A testing setup will be designed and evaluated, forming with the analysis the basis for a testing protocol which is due to be tested within a Round-Robin.

Contents

Nomenclature

Abbreviations

CBT	Corrected Beam Theory
CF/LMPAEK	Carbon Fiber/Low Melting PolyArylEtherKetone
CFRP	Continuous Fiber Reinforced Polymer
CT	Compact Tension
CTP	Crack Tip Position
DCB	Double Cantilever Beam
IFT	Intralaminar Fracture toughness
LEFM	Linear Elastic Fracture Mechanics
NTD	Notch Tip Diameter
NTR	Notch Tip Radius
ROI	Region Of Interest
RR	Round Robin
SENB	Single Edge Notched Bending
UD	Uni-Directional

Symbols

$\overline{r}$	Characteristic length
G_{Ic}	Mode I critical energy release rate
K_{Ic}	Mode I critical stress intensity factor
U_1	Work energy input
U_2	Released energy
U_3	Stored elastic energy
U_5	Unrecoverable plastic deformation energy
I,II,III	crack propagation modes

1 | Introduction

Continuous Fiber Reinforced Polymers (CFRPs) are used in many applications and are becoming more advanced every day. CFRPs are often used in high tech industries like aerospace, superstructures of ships, automotive and civil engineering. An important part of design for these industries is the prediction of component failure by one of the many failure modes present in CFRPs and the subsequent design limits.

CFRPs consist of several layers (plies) stacked on top op each other and are consolidated afterwards, forming a composite material. These layers are placed in different orientations to withstand different forces in certain directions dependent on the intended purpose of the material. The presence of fibers with different directions within the matrix materials results in a composite being a highly anisotropic material with complex damage mechanisms, often progressing each other. Usually, matrix failure, requiring little energy, is the start of it all. With advancing technology, there is a growing need to characterize these materials on a deeper level, for example, when it comes to resistance to crack growth. This includes having a better understanding of the material properties of CFRPs.

1.1 Crack propagation characterization

A widely studied and periodically checked for failure mechanism, largely concerning matrix failure, is delamination. Delamination is the separation of layers itself, breaking the basic connection of the layers. Several methods to detect delamination failure (e.g., ultrasonic scanning) but also crack propagation characterizations methods have been developed.

A less widely studied failure mechanism, but related to delamination failure, is longitudinal intralaminar cracking (also known as transverse cracking). As can be seen in **Figure 1.1**, a [0,90] laminate is presented in which a longitudinal and transverse intralaminar crack and delamination failure are presented. In this laminate, the intralaminar crack propagates in transversal direction (indicated with the red arrow in -3 direction) of the laminate, but is stopped by a layer with a different direction, after which the crack forms the start for a delamination (blue) and starts to propagate between the two layers in the resin rich inter-ply region. However, where a propagating transverse crack can be stopped by a layer with different fiber orientation, this is not the case in the layer itself. Here the crack can continue to grow in the longitudinal direction parallel to the fibers (indicated with the red arrow in -1 direction).

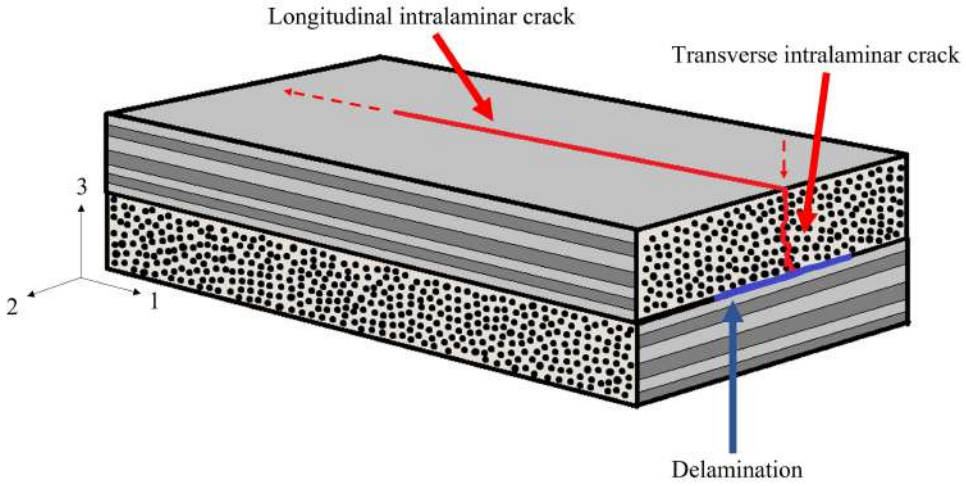

Figure 1.1: Longitudinal and transverse intralaminar crack and delamination failure

The propagation and initiation of cracks are a result of forces and resulting stresses on the laminate. In the characterization of those forces, 3 different Modes can be distinguished as depicted in **Figure 1.2**. The fracture toughness of a material can be expressed in one, or a combination of these Modes. Mode I, is called the 'opening' Mode and is characterized by a symmetrical crack opening, whereas Mode II and Mode III exhibit anti-symmetric behaviour.

The propagation of a crack in a laminate is usually a combination of the Modes. A lot of experiments and corresponding test setups, as well as the ones mentioned in this thesis, are set-up in such a way that Mode II and Mode III are eliminated and only Mode I remains. Therefore, only Mode I will be mentioned from here after. Modes are denoted by a subscript like the following: G_{Ic}. This is the critical Mode I Energy Release Rate.

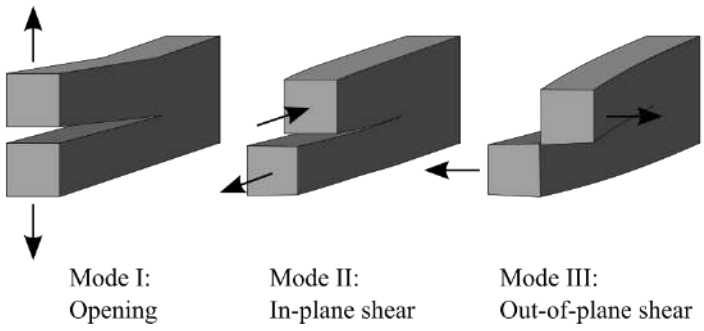

Figure 1.2: Different loading modes [1]

1.2 Objective, motivation and scope

The objective of this master thesis project is to propose a protocol for the experimental evaluation of the Mode I longitudinal intralaminar fracture toughness of CFRPs under quasi-static loading, based on the existing ISO 13586 standard [2] for the determination of Mode I fracture toughness in plastics and plastics containing short fibers, and next to that, the crack propagation resistance, characterized by the R-curve and documented in the ISO 15024 standard [3] as will be explained later in **Section 2.2**.

Previously, the ISO 13586 has been used as a basis for the ISO 17281 standard [4] which extended

the usable load-point displacement rates from 0.1m/s up to 1 m/s and is used for determining the fracture toughness of plastics in the crack-opening mode (Mode I) by a Linear Elastic Fracture Mechanics (LEFM) approach. This formed the basis in the idea of using this same ISO 13586 standard for the Intralaminar Fracture Toughness (IFT) of CFRPs.

The addition of this new test method for Mode I intralaminar fracture toughness and crack propagation resistance would add to existing test methods on interlaminar fracture toughness (ISO 15024), necessary to, for example, model damage evolution in composite structures and determine/predict premature failure. The project includes a literature research on possible testing geometry and corresponding analysis to quantify the toughness. Such an analysis may require the use of numerical tools. Furthermore, a testing setup will be designed and evaluated, forming with the analysis the basis for a testing protocol which is due to be tested within a Round-Robin (RR).

A Round-Robin program aids to form the basis of a new testing standard. In a Round-Robin test, a number of laboratories/universities test identical samples with a proposed test method, to determine the precision (i.e., repeatability and reproducibility) of each reported parameter in a test method. Thus, a Round-Robin program is an analysis technique which uses the Analysis of Variance (ANOVA) random effects model to assess a measurement system. Round-Robin tests help to bring to light systematic sources of error and can give rise to the necessary corrective action [5].

The outcomes of this project will include:

- a protocol or appendix for the ISO 13586 standard for the experimental evaluation of the Mode I intralaminar fracture toughness of continuous fiber reinforced polymers (CFRPs) concerning the fracture toughness K_{Ic}, and critical Mode I energy release rate G_{Ic} under quasi-static loading as will be explained later on. Furthermore, it should contain the determination of the R-curve (based on the ISO 15024 standard), requiring the monitoring of crack length during crack propagation, which will be explained later on as well. This protocol or appendix should be with clear formulation, without ambiguity and easy to follow.

- a Master thesis, explaining all the work done, preliminary research and final deliverables in academic writing.

- a LabVIEW implementation for monitoring the parameters used in the determination of longitudinal Mode I intralaminar fracture toughness and crack propagation resistance of CFRPs.

- a database (e.g., MS Excel) with (Round-Robin) test results and other important documents/results.

Finally, it is important to characterize the material that will be used in the design of the protocol. The laminate is a $[0]_{30}$ uni-directional Carbon Fiber/Low Melting PolyArylEtherKetone (CF/LMPAEK) composite manufactured by press-consolidation of Toray Cetex® TC1225 fabric pre-preg layers.

Toray Cetex® TC1225 is a high-end thermoplastic composite material, utilizing a semi-crystalline engineered low-melt PAEK resin for excellent mechanical performance and superior processability due to a low-melt viscosity and reduction in processing temperature of up to 60°C. This yields a high-quality product used in Automated Tape Laying/Automated Fiber Placement (ATL/AFP) processes. It also speeds up cycle times, enabling cost-efficient production. The material is available as a Uni Directional (UD) tape, a fabric pre-preg, and as Reinforced Thermoplastic Laminates (RTLs) of varying thicknesses [6].

The matrix material is the Victrex® AE250 LMPAEK polymer and the fibers are Toray Cetex® T700 carbon fibers. The data sheet of a single pre-preg of this CF/LMPAEK material is appended in **Appendix H-1**. Furthermore, the data sheet of the matrix material is found in **Appendix H-2**.

1.3 Research questions

This section will provide the main question and several sub-questions that formed the guideline for the research in this master thesis and will be answered in **Chapter 7**.

Main-question:

- How can the longitudinal Mode I intralaminar fracture toughness and subsequent R-curve of CFRPs be determined with high precision and reproducibility at quasi-static loading rates?

Sub-questions:

- What testing setups for polymer-, interlaminar-, or experimental intralaminar fracture toughness are used and are there testing standards that can aid in the design of a standard for the longitudinal intralaminar fracture toughness?
- How does an experimental test setup (specimen preparation and testing) to determine longitudinal Mode I IFT of CFRPs look like and how can fracture toughness and crack propagation resistance be calculated from this?
- What phenomena influence the results of the experimental longitudinal Mode I IFT test?
- How can the crack growth be measured with the use of image processing while performing a longitudinal Mode I IFT test of a CFRP?
- How can a protocol ensure high precision and reproducibility for longitudinal Mode I IFT testing be designed?

1.4 Report outline

This report is divided into several parts. First, the topic will be explained and a relevant background will be provided since this research requires knowledge of the ISO 13586 standard and the underlying fracture mechanics and therewith corresponding crack initiation. These topics are presented in the background in **Chapter 2**. Then, in **Chapter 3**, the methods used to design the testing protocol will be explained. Here, the effects of changing several parameters will be examined to build upon the experimental methods by choosing a pre-crack depth and other important parameters for the final protocol. Next, the experimental methods used in the machining of the specimen and the creation of the pre-crack are documented. Furthermore, it documents the preliminary results regarding, among others, the K_{Ic}, G_{Ic} and crack propagation resistance of the tested specimens prior to Round-Robin testing. Furthermore, the chapter explains the test setup used and briefly elaborates on the LabVIEW crack tip following algorithm. The workings of the this algorithm to be used in determining the crack growth resistance curve, can be found in **Appendix B**. Then, **Chapter 4** documents the results of the Round-Robin Mode I longitudinal intralaminar fracture toughness testing using the designed test method and discusses them. **Chapter 5** will set forth the differences and agreements between the designed protocol and existing standards used during this design. Finally, **Chapter 6** will provide feedback on the test protocol and the experimental methods used and **Chapter 7** will conclude this report by answering the research questions stated before finishing with several recommendations.

2 | Background and relevant theory

This chapter will provide a background for the present research. It is important to have a profound understanding of the state of the art in testing of fracture initiation crack growth in CFRPs. As preliminary work a literature review has been performed to gain more insight into IFT testing [7]. First, Linear Elastic Fracture Mechanics (LEFM) will be introduced, whereafter the energy release rate and corresponding R-curve will be introduced by an analysis of the energy balance in fracture propagation. Then, an LEFM approach to determine K_{Ic} and G_{Ic} for fracture initiation, as used in ISO 13586, is explained. Besides, the different fracture mechanisms in play in intralaminar cracks have been researched. Next, the influence of loading rate and crystallinity on the IFT is presented, whereafter the applicability of an LEFM approach for the IFT will be discussed. Lastly, various, in literature documented, experimental test methods that have been used in determining IFT and other important key developments in the field are mentioned.

2.1 Linear elastic fracture mechanics

Linear Elastic Fracture Mechanics (LEFM) is a theory to determine a materials resistance to fracture that has been developed over the course of a century. It is built upon the work done by: Kirsch who created a solution to determine stresses around a hole in 1898 [8], Inglis who created a solution for stress around an elliptical hole, more closely resembling a crack in 1913 [9], Griffith who first introduced the term energy release rate G in 1920 [10], Westergaard who created a solution to determine stresses around a crack in 1939 [11], and finally Irwin who came up with the definition of the stress intensity factor K in 1957 [12].

According to LEFM, Mode I plane-strain fracture toughness is characterized by the critical stress intensity factor K_c (MPa·m$^{1/2}$) of a sharp crack where propagation of the crack suddenly becomes rapid and unlimited [13]. Furthermore, the critical energy release rate G_c is defined as the value of the energy release rate G (J/m^2) in a pre-cracked specimen under plane-strain loading conditions, when the crack starts to grow [2]. The G_c and K_c show a certain relationship which will be treated later on.

When the plastic zone around the crack tip is significantly small relative to the crack length, the stress state around the crack tip can be assumed plane-strain and is the result of elastic forces acting within the material. However, when the plastic zone around the crack tip becomes increasingly large, showing significant plastic deformation, the Elastic-Plastic Fracture Mechanics (EPFM) theory applies. Within this theory, J-integrals are used to approximate the fracture toughness K.

The condition of plane-strain is an important property in fracture mechanics. When the plane-strain condition is present, the, in testing determined value of fracture toughness K_c, will not change with increasing thickness. This means that the material response of a small laboratory specimen may be used to study the material response of a large structure to the same stress intensity, allowing for general design and failure prediction.

2.2 Energy release rate and corresponding crack propagation resistance

An important visualization of a material's resistance against crack propagation is the R-curve, short for resistance curve where the critical energy release rate G_c is plotted against the crack length a. An R-curve may be used to study the stability of crack propagation, it shows the transition between stable and unstable crack growth.

2.2.1 Energy balance analysis

To start the understanding of the R-curve, the first step is to have a proper understanding of the energy release rate itself and how it changes. The energy release rate G is the rate of energy needed to propagate a crack over a certain area A. This is explained by the following fracture mechanics energy analysis. Consider an arbitrary body and place a closed contour Γ around it, as can be seen in **Figure 2.1**. Over the border an energy flow dU_1 takes place, which is split into 3 components. dU_2 is the released energy by crack propagation. dU_3 is the stored elastic energy within the boundary of the body, considering an isothermal system. Furthermore, dU_4 is the kinetic energy in the system. In case of crack initiation, the body is in rest, meaning dU_4 is equal to zero. finally, dU_5 is the plastic or viscous deformation of the material, transformed to heat.

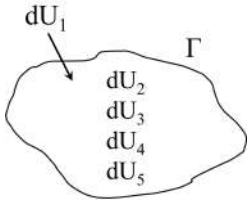

Figure 2.1: Change of energy in a closed system

When incremental crack growth occurs, the energy relation can be given by **Equation (2.1)**, where A is equal to the fractured surface, usually Bda, where B is the material thickness and da the increment in crack length.

$$\frac{dU_2}{dA} = \frac{dU_1}{dA} - \frac{dU_3}{dA} \tag{2.1}$$

Here the fraction $\frac{dU_2}{dA}$ is the change in crack growth propagation, indicated with R (a materials resistance to crack growth by dA). This relation is presented by **Equation (2.2)**.

$$R = \frac{dU_2}{dA} \tag{2.2}$$

Then, the change of energy over the contour of the body is equal to $\frac{dU_1}{dA} - \frac{dU_3}{dA}$, and is the change of external work minus the change of internal work over crack extension dA. This relation is presented by **Equation (2.3)**. This change in energy is called energy release rate and is denoted by G. It is important to notice that a simple balance between internal and external work does not suffice in fracture mechanics since a crack breaks bonds between atoms, a phenomenon that can only occur by a change in energy.

$$G = \frac{dU_1}{dA} - \frac{dU_3}{dA} \tag{2.3}$$

By **Equation (2.1)**, we can now write **Equation (2.4)** for equilibrium.

$$G = R \tag{2.4}$$

For a crack to propagate, $G - R \geq 0$ applies. After crack initiation $\frac{dU_4}{dA}$ has to be positive since the crack growth speed is non-zero. In short, G increases until $G = R$, whereafter crack growth occurs. The evaluation of R itself will be treated later in **Section 3.6**.

Between G and K (being the fracture toughness) exists a relationship, which is presented in **Equation (2.5)** for plane-strain conditions where $\frac{E}{1-\upsilon^2}$ is the Young's modulus of the material. This is a direct consequence of an effective stiffness increase experienced when an object is pulled in tension, but with one lateral plane constrained from contracting under Poisson effects [14]. As can be seen, the two are directly related by the Young's modulus of the material, which, in a case of a highly anisotropic CFRP, is a bit of grey area due to the relationship depending on direction and micro-structure.

$$G_c = \frac{K_c^2}{\frac{E}{1-\upsilon^2}} \tag{2.5}$$

2.2.2 Crack growth resistance

When testing the fracture toughness of intralaminar cracks in Single Edge Notched Bending (SENB) specimens, it became apparent that, in contrary to a polymer, the crack propagation seemed rather controlled and stable and much more similar to the crack propagation of a Double Cantilever Beam (DCB) specimen. Therefore, the interest was awakened to characterize the R-curve for intralaminar cracks as well after this had been done before by polymers.

Although, the ISO 13586 standard does provide a guideline for the testing of fracture initiation with K_{Ic} and G_{Ic}, it does not provide a method for the characterization of the R-curve. This, since the standard is meant for the fracture toughness testing of polymers. When testing a polymer SENB specimen on fracture toughness, the fracture will usually be brittle and instantaneous and will not exhibit a stable crack growth, thus eliminating the need to create an R-curve.

When G_c stays relatively consistent over the course of the crack length, it can be said that the crack growth is consistent, thus stable. The R-curve is obtained by calculating the critical energy release rate G_c at several points during crack propagation. The unit of G_c is J/m^2. A consistent crack growth is characterized by the fact that the increase in energy required to propagate the crack dU_2 divided by the increase in fractured area dA, is consistent over the crack length such that the ratio J/m^2 is consistent and subsequently G_c.

A typical R-curve in, for example, a DCB test for interlaminar fracture toughness, will show an increasing delamination resistance with delamination length. An example of such an R-curve can be seen in **Figure 2.2**. The increase of the required critical energy release rate to propagate the crack is due to a phenomenon called fiber bridging and partly due to toughening mechanisms present in the material.

2.3 Intralaminar fracture toughness with a LEFM approach

For the fracture toughness testing of polymers under quasi-static loading, the ISO 13586 standard provides a method to determine this material property. The idea is to design the intralaminar test standard as a protocol based on this published standard by using the same specimen type and same direction of crack propagation as will be explained later on. However, the degree of conformity between an intralaminar crack and a crack in a polymer material is, as of yet, unknown. This section will provide some insight in the research needed to determine the degree of conformity and the areas where extra attention is needed because of deviations on the LEFM method due to composites simply not being polymers. This can be, for example, a wrongly assumed state of stress/strain in the calculation of the Mode I longitudinal intralaminar fracture toughness.

The LEFM approach, as explained in **Section 2.1**, can be used to determine the fracture toughness of a, by approximation, linear elastic thermoplastic or thermosetting polymer. Since the matrix material in CFRPs is usually a polymer, the ISO 13586 standardised test [2] to determine the fracture toughness of polymers will be used in this theoretical approach for longitudinal Mode I intralaminar fracture toughness of CFRPs. A plane-strain condition is assumed at the crack tip and the method assumes linear

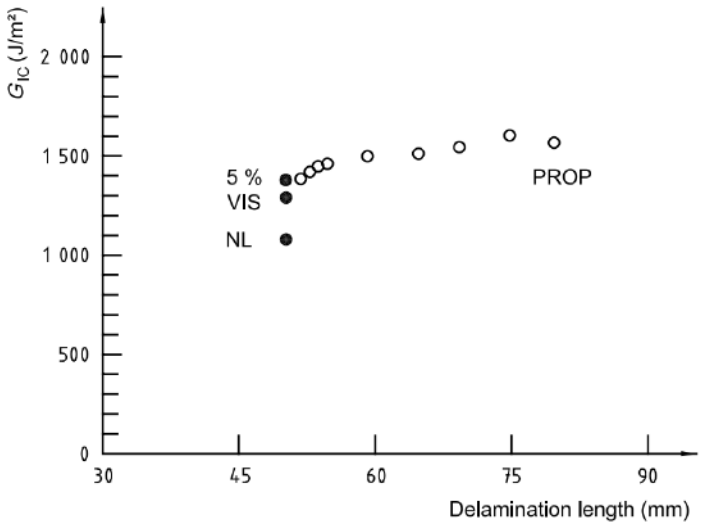

Figure 2.2: Typical R-curve with increasing crack propagation resistance [2]

elastic behaviour of the cracked material. The specimen dimension guidelines for SENB specimens are presented in **Figure 2.3** on the left and for Compact Tension (CT) specimens, on the right. When determining longitudinal Mode I IFT, the fiber direction in SENB and CT specimens would be parallel to the crack length a and stack-up direction would be in height direction h.

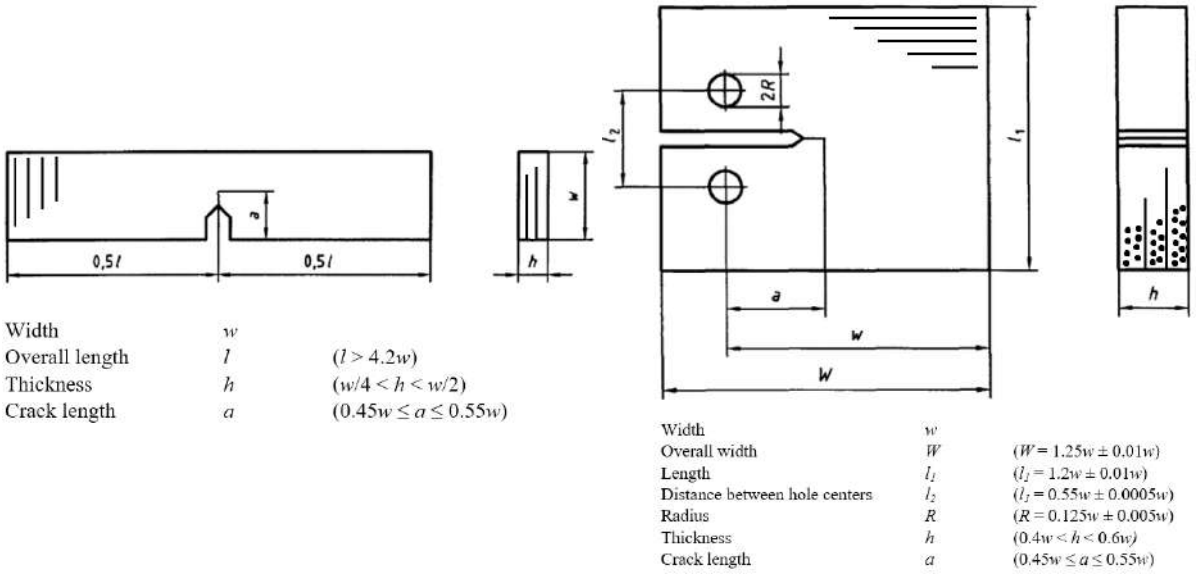

Figure 2.3: Left: Single Edge Notched Bending (SENB) specimen, Right: Compact Tension (CT) specimen [2]

The critical Mode I energy release rate G_{Ic} is defined in **Equation (2.6)** where W_B is the energy to fracture (i.e. the product of force times displacement in the force-displacement plot of the specimen at point of crack initiation, divided by 2). The thickness and width of the specimen are h and w respectively. Then $\phi(a/w)$ is the energy calibration factor, dependent on the crack length a. This factor is added to account for the crack length dependent stiffness of the test specimen and accounts for changing load-line compliance For simplicity, the formula for this factor is omitted, but can be found in the ISO 13586 standard for both the SENB and CT tests in **Appendix C**.

$$G_{Ic} = \frac{W_B}{h \cdot w \cdot \phi(a/w)} \tag{2.6}$$

The critical Mode I stress intensity factor K_{Ic} is given by **Equation (2.7)** where F_{Ic} is the load at crack growth initiation, h is the test specimen thickness, w the test specimen width and $f(a/w)$ is the geometry calibration factor, depending on the crack length a. This factor is added to account for the configuration and the dimensions of the test specimen. Again, for simplicity, the formula for this factor is omitted, but can be found in the ISO 13586 standard in **Appendix C**.

$$K_{Ic} = f(a/w) \cdot \frac{F_{Ic}}{h\sqrt{w}} \tag{2.7}$$

The load at crack growth initiation F_{Ic} is subject to the definition of 'initiation'. To define initiation, two lines are drawn in the force-displacement plot as depicted in **Figure 2.4**. The first one being the zero-point secant and the second one the 95%-stiffness secant. If the maximum of the load displacement curve falls within these lines, then $F_{Ic} = F_{max}$. If the second tangent intersects the load curve at F_s, prior to the maximum, then $F_{Ic} = F_s$. In other words, $F_{max}/F_s < 1.1$, which translates to the fact that the conditions of LEFM are met when maximum 10% non-linearity is present in the, linearly assumed, deformation.

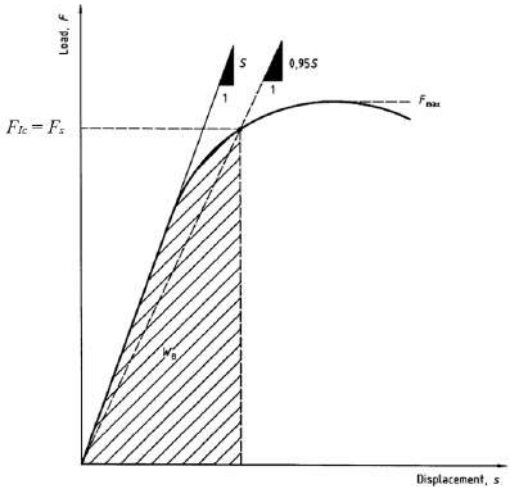

Figure 2.4: Force-displacement plot with zero-point secant and 95%-stiffness secant [2]

Small test specimens usually influence the result of the fracture toughness test by non-linearity. This occurs, for example, when the size of the plastic zone around the crack tip is significantly large with regard to the specimen size and the LEFM method is not valid anymore as explained in **Section 2.1**. Therefore, the specimen size needs to be significantly larger than the plastic zone around the crack tip such that plane-strain can be assumed. This plastic zone is characterized by the length $\overline{r}$.

The linearity assumption is valid if the following 3 points are satisfied:

1. thickness $h \geq 2.5 \cdot \overline{r}$
2. crack length $a \geq 2.5 \cdot \overline{r}$
3. ligament width $(w - a) \geq 2.5 \cdot \overline{r}$

The characteristic length $\overline{r}$ is given by **Equation (2.8)**, or **Equation (2.9)**, where h is the test specimen thickness, $f(a/w)$ is the geometry calibration factor, $\phi(a/w)$ is the energy calibration factor, S is the test specimen stiffness (being the initial slope of the force-displacement diagram) and σ_y is the uni-axial tensile yield stress or, alternatively, 0.7 times the compressive yield stress.

$$\vec{r} = \frac{2f(a/w)^2 \cdot \phi(a/w) \cdot S \cdot G_{Ic}}{h \cdot \sigma_y^2} \tag{2.8}$$

$$\vec{r} = \frac{K_{Ic}^2}{\sigma_y^2} \tag{2.9}$$

The results for G_{Ic} and K_{Ic} can be cross-checked by use of the Young's modulus E since it is related to the stiffness S and to the mechanical fracture properties G_{Ic} and K_{Ic} as follows in **Equations (2.10)** and **(2.11)**. Usually E_{stiff} is slightly larger than E_{fract}. If the difference exceeds 15%, the results obtained for G_{Ic} and K_{Ic} should be examined for possible errors.

$$E_{stiff} = \frac{2f(a/w)^2 \cdot \phi(a/w) \cdot S}{h} \tag{2.10}$$

$$E_{fract} = \frac{K_{Ic}^2}{G_{Ic}} \tag{2.11}$$

2.4 Intralaminar fracture mechanisms

The different fracture mechanisms in play in intralaminar fracture toughness have been looked into. This, to eventually gain insight in what the effect of these mechanisms is on fracture initiation and crack propagation. Iwamoto et al [15] have investigated the fracture mechanisms present in a longitudinal intralaminar crack under Mode I loading using a Double Cantilever Beam (DCB) setup and reported longitudinal splitting where the matrix splits parallel to the fibers, fiber-matrix debonding in direction of crack propagation and matrix cracking as the present fracture mechanisms (**Figure 2.5**).

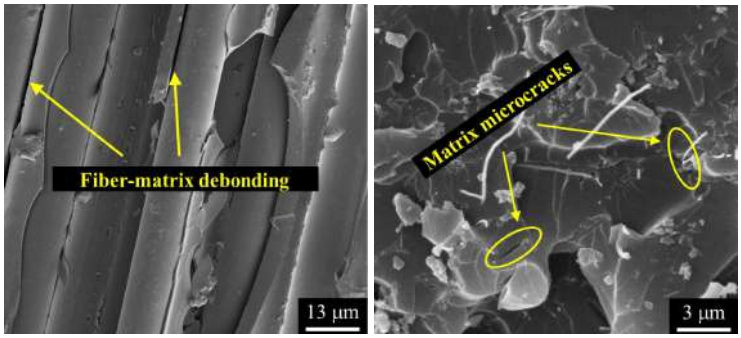

Figure 2.5: Different fracture mechanisms in intralaminar cracks [16]

Several papers stated the matrix material to be stronger than the fiber-matrix interface [17, 18, 19]. Therefore, the fracture toughness of a matrix material will also be larger than the fracture toughness of the fiber-matrix interface, resulting in the fiber-matrix interface failing first in intralaminar fracture toughness tests. Besides, Tanoglu et al [20] have reported the fiber-matrix debonding to become increasingly dominant under increasing loading. With other words, the fiber-matrix interface is dominant, whereas the matrix and fibers play a secondary role in intralaminar fracture [17, 21].

Falzon et al [22] suggested the Mode I transverse intralaminar fracture toughness to be similar to the Mode I interlaminar fracture toughness for the same material due to similarity in fracture mode. However, longitudinal intralaminar cracks show different damage mechanisms on close inspection since a phenomenon known as fiber bridging is present in varying degrees [15].

Iwamoto et al. concluded that the fibers had a huge influence on the energy-to-fracture as well. Fiber bridging is where the crack front 'jumps' one or multiple fibers and continuous on the other side. As shown in **Figure 2.6**, this results in one or a bundle of fibers bridging the crack opening in the specimen used in Iwamoto et al. their intralaminar DCB setup. The effect of bridging fibers could be countered by cutting the fibers with a sharp razor, thereafter it was possible to obtain the intralaminar fracture toughness without the influence of fiber bridging. When the fibers were not cut, the fracture toughness increased with increasing crack length due to decreasing compliance and was found to be approximately twice as large as that without fibers [15].

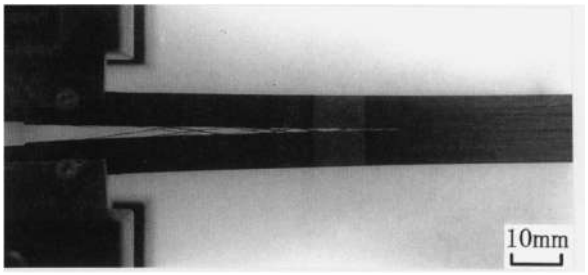

Figure 2.6: Example of intralaminar fiber bridging [15]

Next to that, Pappas et al. concluded that the morphology of longitudinal intralaminar fiber bridging is completely different than that of DCB fiber bridging, containing larger bundles and a rather irregular fracture cross section [21]. Hence, the same intralaminar-to-interlaminar similarity is nonexistent for longitudinal cracks and it is paramount to distinguish between transverse and longitudinal intralaminar fracture toughness.

2.5 Influence of loading rate and crystallinity on fracture toughness

It is widely known that polymers are rate sensitive in determining the fracture toughness. Since polymers are used in CFRPs as well, there is probably an influence of loading rate on the determination of longitudinal Mode I intralaminar fracture toughness. Literature research has shown a research gap regarding the effect of loading rate on determining the intralaminar Mode I fracture toughness of CFRPs.

When looking at the damage mechanisms that occur while performing a longitudinal Mode I intralaminar loading test as explained in **Section 2.4**, it can be seen that the CFRPs specimens fail by matrix cracking, fiber-matrix debonding, or longitudinal splitting, as reported by Iwamoto et al [15]. By separately looking into the effect of loading rate on the previously mentioned fracture mechanisms, the effect on fiber-matrix interface strength, and the effect on matrix fracture toughness, this part of research aims to provide some insight into the matter.

The data belonging to this research is presented in **Figure 2.7**. All the data are derived from the available research done over the last decades. Here, the loading rate is presented as a change of fracture toughness K_{Ic} over time (MPa·m$^{1/2}$·s^{-1}) as a parameter independent of specimen size, known as stress intensity factor rate. As a means for extrapolation, functions are fitted through the various data points and through missing strain rate regions to characterize the likely transition of fracture toughness without performing actual loading tests at these strain rates. This for the sake of completeness and better visualization of the change of fracture toughness K_{Ic} over loading rate.

It is not straightforward to display a relation between strain rate (1·s^{-1}) and the stress intensity factor

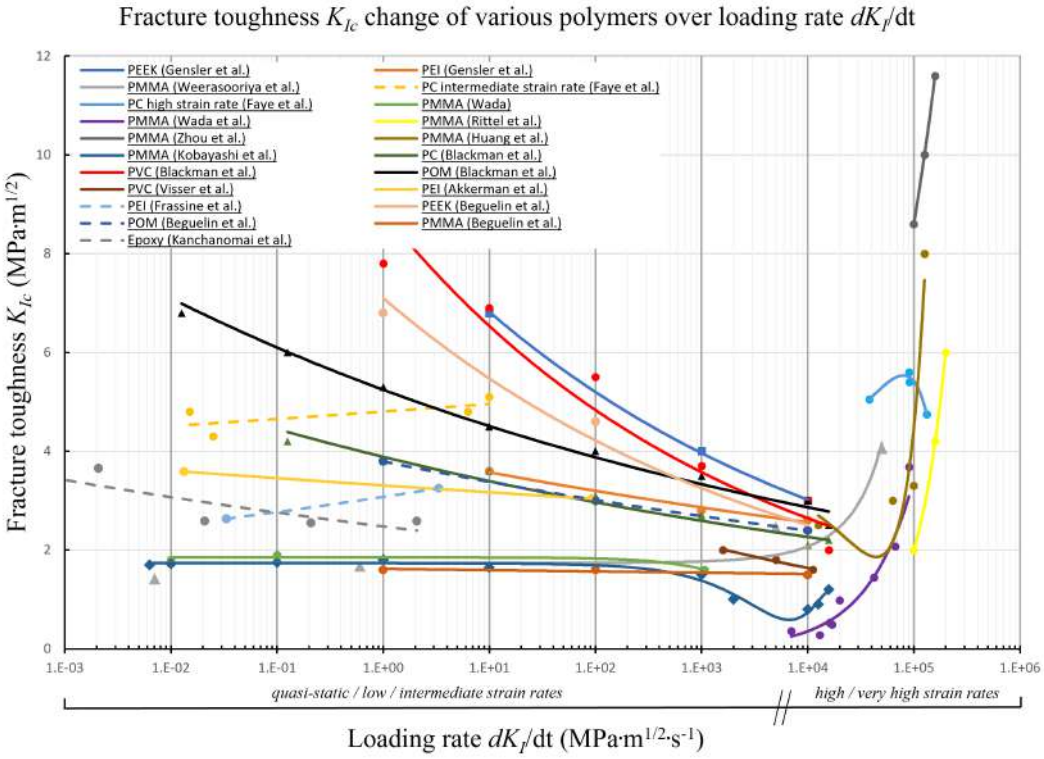

Figure 2.7: Overview of fracture toughness K_{Ic} variation of various polymers with changing loading rate (quasi-static to high rates)

rate (MPa·m$^{1/2}$·s^{-1}). This, since different tests have strain in different directions, different specimen sizes are used and strain distribution is uneven in different specimens. However, an increase in strain rate and the approximate transition of quasi-static/low/intermediate strain rates to high/very high strain rates are presented on a second x-axis, based on the values reported by S. Nemat-Nasser [23] and the strain rates in the presented research.

A general trend was found that the matrix fracture toughness decreases with increasing loading rate under quasi-static/low rate loading [24, 25, 26, 27, 28]. It was also observed that the fracture toughness of the polymer increases under high/very high rate loading [29, 30, 28, 24, 26, 27, 31, 25, 32, 33, 34]. Similarly, the fiber-matrix interface strength decreases with increasing loading rate under quasi-static loading [35] when performing single fiber pull-out tests. The opposite trend is true for dynamic loading [36, 37, 38]. Besides, the higher the amount of crystallinity, the more the fracture toughness of the polymer decreases under increasing quasi-static loading [39, 40, 41, 42]. The opposite is true for dynamic loading [41].

Since longitudinal Mode I intralaminar fracture is characterized by matrix cracking and fiber-matrix debonding, it can be concluded that it is highly likely that the same trends can be expected as well for the FRP fracture toughness. More research into the application of LEFM is needed to gain insight into the unknown extents of anisotropic material properties and non-linearity effects.

2.6 On the applicability of an LEFM approach in determining Mode I intralaminar fracture toughness of CFRPs

The LEFM approach to determine fracture toughness, as described in **Section 2.1** makes use of the following assumptions:

1. Linear elasticity

2. plane-strain condition at the crack tip

This section will provide some insight in whether these assumptions can be met, if the LEFM approach, and subsequently the ISO 13586 standard, may serve as a basic procedure to determine the Mode I longitudinal intralaminar fracture toughness when taking into account the effects of varying loading rate and the anisotropic nature of CFRPs.

When considering linear elasticity, it should be noted that a polymer exhibits visco-elasticity. This may violate the assumption of linear elasticity at insignificantly low loading rates due to time dependent creep. Furthermore, the fracture toughness testing of polymers at high loading rates introduces crack tip blunting due to adiabatic effects, causing local plastic deformation, violating this assumption as well [43]. With SENB and CT specimens one would of course want to keep specimen size to a minimum to minimize costs and allow for the evaluation of a small batch of a material during its development phase. A smaller specimen size translates to a decrease in maximum allowed loading rate since dynamic effects may cause increasingly large errors in smaller specimens. Furthermore, the use of servo-hydraulic machines is limited to 10^{-2} s^{-1}, since adequate damping cannot be assured [23]. With this knowledge, high rate testing is excluded when performing servo-hydraulic testing. The maximum loading rate is then dependent on specimen size and the limit of 0.1 m/s set by the ISO 13586 [2], which translates to a loading rate of 6000 mm/min.

A CFRP is a highly anisotropic material. The LEFM approach, however, assumes linear elastic material behaviour and subsequently isotropic material properties [44], but is used in determining Mode I interlaminar fracture toughness of UD laminates [3]. Shahani et al [45] reported the LEFM approach to be a good approximation to determine growth resistance curves of a glass/epoxy UD laminate with this DCB test, but it may grossly underestimate the fracture resistance of multi directional laminates due to non-linear effects. The non-linear zone ahead of the crack tip, denoted by the characterized length $\overline{r}$ in the LEFM approach in **Section 2.1**, must be small compared to the specimen size. Here, the anisotropic nature may influence the size of this non-linear (plastic) zone, in turn effecting the assumption on plane-strain as explained in **Section 2.1**.

The plastic zone differs for example due to presence of fibers in the matrix material, matrix-rich zones and uneven distribution of fibers and matrix material. Furthermore, when applying this approach to determine the fracture toughness for intralaminar crack propagation in an anisotropic material like a CFRP, the isotropic assumption could be violated by the following phenomena: First, stable crack propagation in longitudinal intralaminar cracks is limited due to the nature of a CFRP material. A crack could initiate by fiber-matrix debonding, encounter matrix-rich regions, and require a higher energy release rate G to propagate. Or a crack jumps a fiber or fiber bundle, and debonds along the other direction of the fiber or fiber bundle since it requires less energy, and causes fiber-bridging. This, in turn, halts the crack propagation when the strong fiber or fiber bundles encounter tension. Next, the co-linearity of the crack direction, and the direction perpendicular to the direction of the applied stress, cannot be guaranteed. This is due to the aforementioned phenomena as well. More research into the effect of anisotropic CFRP materials on the assumption of the isotropic material behaviour related ratio of the non-linear zone size and specimen dimensions, is necessary to provide answers to all the unknown extents of the above mentioned effects and would be subject for future work.

2.7 Different test geometries used in determining longitudinal Mode I IFT

Research has been done into suitable testing geometries for the testing of longitudinal Mode I IFT. This by investigating what geometries have been used by other authors and see what remarks they made about their testing setups and results after testing. First, Frossard et al [46] used a DCB geometry (h=6mm, b=10mm) and CT geometry in determining the intralaminar fracture toughness. They made the remark

that the average energy release rate at initiation was the same for both specimens geometries. However, the steady-state energy release rate was approximately 3 times higher than corresponding interlaminar values. They reported the issue of fiber bridging in both geometries.

Furthermore, Czabaj et al [47] used DCB and CT geometries as well in determining both interlaminar and intralaminar FT. They added starter cracks by thick Teflon inserts (12.5µm). The use of these starter cracks resulted in initially unstable crack growth for both geometries and artificially high FT at initiation. For CT and DCB specimens with fatigue pre-cracks, the intralaminar and interlaminar initiation fracture toughnesses were approximately equal. However, during propagation, the CT specimens exhibited more extensive fiber bridging, and rapidly increasing R-curve behavior than compared to the DCB specimens.

Furthermore, Pappas et al [21] used the DCB geometry with the same dimension as Frossard et al. as well. They reported the intralaminar FT to be approximately 2.3 times higher than the interlaminar FT for the same material, although they have the same initial fracture toughness. Next to this finding, they reported large scale fiber bridging as well. Similarly to Pappas et al., Iwamoto et al [48] performed intralaminar DCB tests on a very thin specimen of 1mm and a height of 12.7mm, reporting fiber bridging too.

2.8 Key developments

Over the past decades, several testing standards have been published to determine the fracture toughness of different materials in different ways. The first relevant standard for this research is the ISO 13586 [2] standard to determine the fracture toughness (G_{Ic} and K_{Ic}) for plastics based on an LEFM approach (ASTM equivalent: ASTM D5045 [49]). This standard makes use of a Single Edge Notched Bending (SENB) or Compact Tension (CT) setup. Later on, an amendment was made, making it possible to determine the fracture toughness of injection-moulded plastics containing discontinuous fibers with the same approach as well. A similar standard, the ISO 17281 [4], was released for the determination of fracture toughness in high rate (>1m/s) testing. Furthermore, the ISO 15024 standard [3] has been released. This document describes a standard to determine the interlaminar fracture toughness (G_{Ic}) of CFRPs for unidirectional composite materials and makes use of the DCB setup.

Furthermore, an ongoing development by the ESIS TC04 group (European Structural Integrity Society) [50] is the creation of pre-cracks with use of an adapted microtome instead of razor tapping or razor sliding as used in ISO 13586 [2]. This method is thought to be more consistent and to create sharper cracks than the method proposed in ISO 13586. More on this method will be presented later on. Finally, next to mechanical pre-cracking, the use of fatigue pre-cracking is more and more present in fracture toughness testing, enabling a better relation to reality and laboratory testing. In fatigue pre-cracking the specimen is cyclically loaded until a pre-crack of a certain length is formed, whereafter the specimen is tested as normal.

3 | Experimental methods: intralaminar fracture toughness test method design

This section will elaborate on the experimental methods used to eventually establish a testing method for the Mode I longitudinal intralaminar fracture toughness and crack propagation resistance. The design of a testing standard is not a straightforward process. It involves a lot of trial and error and a lot of different tests, usually with a lot of changes, adjustments and rejected methods.

In order to create structure in the design process, it has been chosen to review testing standards that have proven themselves already and are relevant for the longitudinal intralaminar fracture toughness as well. One of these standards is the ISO 13586 [2] (with ASTM equivalent: ASTM D5045 [49]), which is the testing standard for the determination of fracture toughness (G_{Ic} and K_{Ic}) in plastics or Short Fiber Reinforced Plastics (SFRPs) based on a Linear Elastic Fracture Mechanics (LEFM) approach. Next, the ISO 15024 standard [3] is relevant. This standard is for the determination of Mode I interlaminar fracture toughness, G_{Ic}, for unidirectionally reinforced materials and makes use of the Double Cantilever Beam (DCB) test.

Several elements of these standards will find its way in the final testing protocol for the longitudinal intralaminar fracture toughness as well as in this chapter. The choices made during the design process of this testing will be explained and when relevant, background information will be provided so that the choices made in the design can be substantiated. This chapter will elaborate on the testing method chosen, the specific dimensions for the composite specimens based on an analysis of previous testing results with changing parameters, the LEFM assumption of plane-strain with a FEM approximation and finally the production of the composite samples itself including: sawing, machining and cutting.

3.1 Test method geometry

When designing a test method for the longitudinal intralaminar fracture toughness, one of the first steps is to decide on a test geometry itself. When selecting a geometry some important factors are the ease of testing, easy of monitoring the crack length, nominal size of specimens and manufacturability of specimens.

The ISO 13586 standard recommends either the SENB geometry where a specimen is subjected to an edge load in the middle while supported on two sides or the CT geometry where a specimen is subjected to a tension load by two pins, without support. The ISO 15024 standard makes use of the DCB configuration, having a similar tensile load between two pins as the CT geometry and no further support. Further research into the state of the art of experimental test for intralaminar fracture toughness revealed that a Compact Compression (CC) geometry has been used as well. However, it has been chosen to design the protocol based on proven test standards to create a solid base. **Figure 3.1** shows the three different test specimens geometries, as if they were being used for the Mode I intralaminar fracture toughness test.

When taking into account the important factors in selecting a method to test the Mode I intralaminar fracture toughness, the first factor to consider is the ease of testing and preparation. For the CT test, tension holes have to be created such that the specimen can be tested. Next to this extra step in specimen preparation, the risk of failure at these tension holes exists. For the DCB test two 'load blocks' or piano hinges have to be glued to the specimen in order to be able to perform the test. This, again, is prone to failure due to failure of the adhesive at the connection of the load blocks. With a SENB test these two known failures and extra specimen preparation steps are not present.

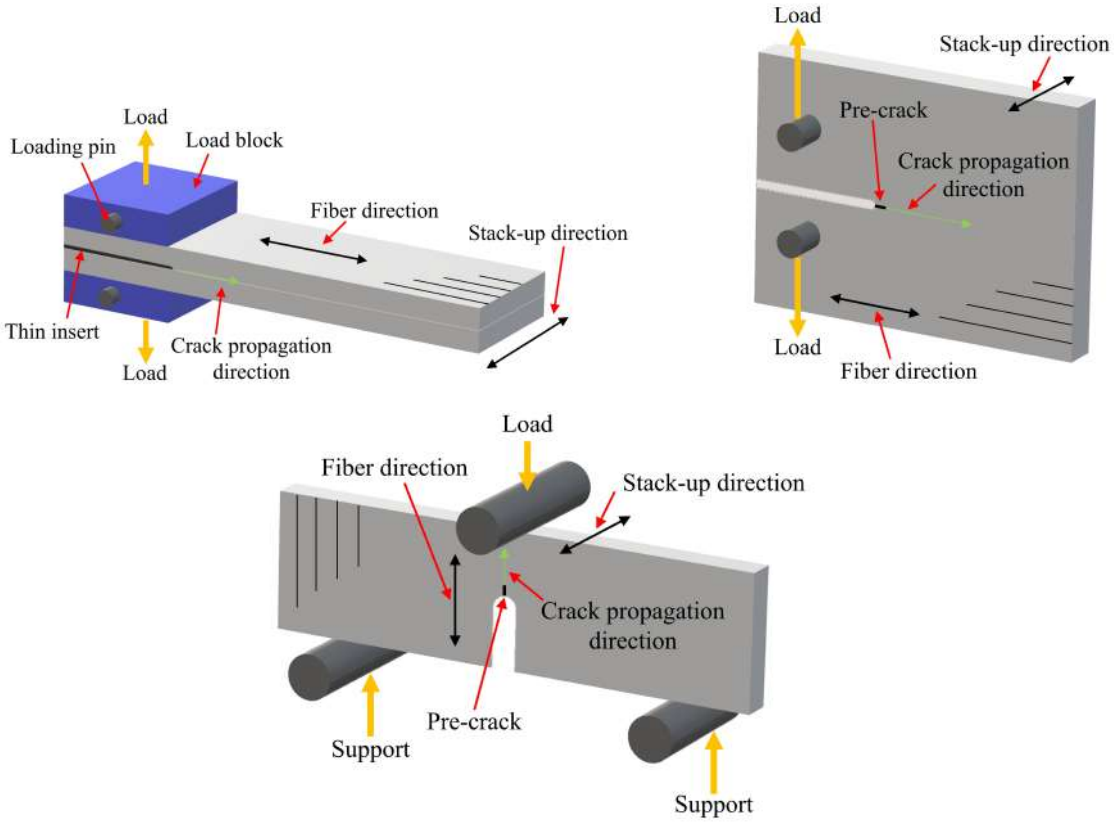

Figure 3.1: DCB specimen (top left), CT specimen (top right) and SENB specimen (bottom) geometry, with indicated fiber direction and stack-up, if they were used in longitudinal intralaminar FT testing

Generally, for ease of monitoring the crack length, it can be stated that a longer crack allows a longer tracking of the crack itself, making it easier to create a more accurate resistance curve when having more data points. For the CT and SENB test, the tracking of the crack itself is limited because of the limited specimen dimensions. However, if a camera is used with a resolution high enough, an accurate resistance curve should be able to be constructed as well.

When considering the size of the specimens and their manufacturability, the CT specimen, as mentioned before, requires an extra manufacturing step in manufacturing the tension holes. Furthermore, the DCB test requires an extra step in placing an insert in the laminate to create a start for the interlaminar crack to form. When translating this to an intralaminar crack, problems arise. First of all, it is very difficult to manufacture a DCB specimen with a layup suitable to test the longitudinal intralaminar fracture toughness (see **Figure 3.1** on the bottom). This would require a very thick laminate, as specimens have to be cut sideways out of the laminate. Furthermore thin inserts (usually Teflon) have to be placed prior to pressing and consolidating the laminate, being an extra step and less straightforward than placing an insert between 2 layers, if not very difficult. Finally, a suitable DCB setup would be prone to Mode I-Mode 3 loading and buckling, due to its relatively thin width compared to its height.

Taking all these findings into account, it has been chosen to continue the design of the test method with a SENB setup since it requires less material than a DCB geometry, and eases the manufacturing process compared to CT and DCB geometries, having no insert or extra machining steps, only leaving the initial notching/pre-cracking.

3.2 Specimen dimensions

After having chosen the SENB test method, the ISO 13586 test standard can be considered as guideline for the further design of the test standard for the Mode I intralaminar fracture toughness. The ISO 13586 guidelines regarding these specimen dimensions are presented in **Table 3.1**. The mentioned symbols are depicted in **Figure 3.2**.

Table 3.1: Specimen dimension guidelines set by ISO 13586 [2]

Parameter	Symbol	Chosen dimensions [mm]	Guideline limits [mm]
overall length	l	70	$l > 4.2w \Rightarrow 70 > 58.8$
thickness	h	4.3	$w/4 < h < w/2 \Rightarrow 3.5 < 4.3 < 7$
crack length	a	6.5 excl. pre-crack	$0.45 \leq a/w \leq 0.55 \Rightarrow 0.45 \leq 6.5/14 \leq 0.55$
width	w	14	$w = 2h \Rightarrow 14 = 8.6$

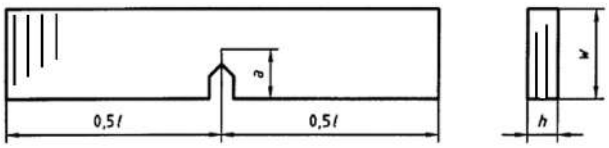

Figure 3.2: Recapitulation of SENB specimen dimensions and corresponding symbols

Furthermore, as a material, a Toray Cetex© 1225 laminate with a thickness of 4.3mm has been chosen, such that the length of a specimen has been set to 70mm, with a span of 65mm, a thickness of 4.3mm, a height of 14mm, and an initial crack length of 6.5mm (i.e., excluding pre-crack cutting). All these values are within the ranges set by the standard and should therefore, theoretically provide accurate and reliable results for K_{Ic} and G_{Ic}. This section and corresponding subsections will dive into the phenomena that played a role on setting these specimen dimensions.

3.2.1 Size criteria

Next to the dimension limits, the entire calculation of K_{Ic} and G_{Ic} in the ISO 13586 standard is based on the LEFM method. Within linear elastic fracture mechanics, a plane-strain condition is assumed at the crack tip and the method assumes linear elastic behaviour of the isotropic cracked material. This plane-strain condition is an important factor.

When a SENB specimen is loaded, plastic deformations will develop when the yield stress of the material is exceeded in the crack tip region prior to cracking. Part of the material near the crack tip and close to a free surface can deform in thickness direction of the specimen due to stresses normal to the free surface, since there is no excess material to prevent this. Therefore, the plastic zone increases and the fracture energy is spread over this larger area, increasing the value of K_{Ic}.

The value of K_{Ic} decreases with thickness until the thickness exceeds some critical dimension. This can be seen by the red line in **Figure 3.3** where a generic relation between the specimen thickness and the fracture toughness, illustrated with the change in plane-strain related zone, is presented [51]. At this point the value of K_{Ic} becomes relatively constant and is a true material property called the plane-strain fracture toughness and independent of actual specimen thickness. Although there will always be a small strain component in the thickness direction, it is negligible compared to the other strain components.

The ISO 13586 as well as the ASTM D5045 standard mention three size criteria.

1. thickness h: $h > 2.5 * \overline{r}$
2. crack length a: $a > 2.5 * \overline{r}$

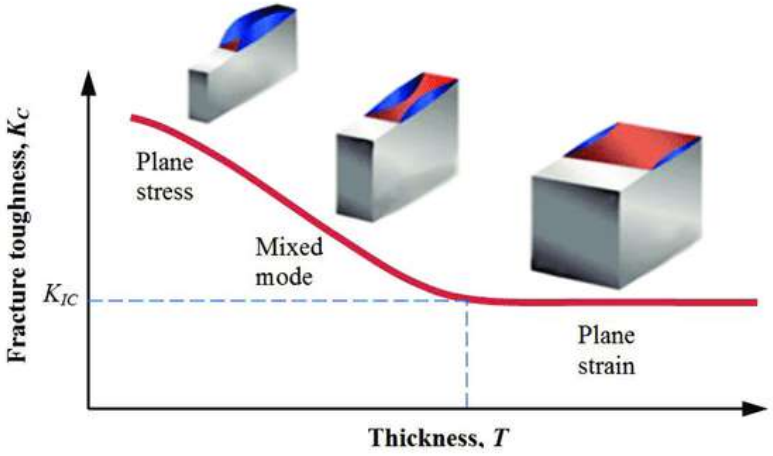

Figure 3.3: Plane stress to plane-strain transition [51]

3. ligament width $(w - a_0)$: $(w - a_0) > 2.5 * \overline{r}$

This, to ensure the condition of plane-strain or prevent certain phenomena from influencing this condition by ensuring the dimensions are significantly larger than the plastic zone around the crack tip, characterized by the characteristic length $\overline{r}$. The characteristic length $\overline{r}$ can be calculated by two methods. The formulae for methods are presented in **Equation (2.8)** and **Equation (2.9)** respectively.

In the design of the testing protocol for the Mode I intralaminar fracture toughness, the question arises what the factor 2.5 in the size criteria is based on and why a characteristic length is defined at all. Research has shown that the value of 2.5 is a semi-emperical value, remnant from testing of metal specimens [52]. This means it has been determined by lots a practical tests. When the calculated $\overline{r}$ is small enough, with respect to h,a, and $w - a_0$, it can be stated that the plane-strain condition applies. The value of $\overline{r}$ is the theoretical size of the plastic zone around the crack tip. The letter r refers to radius, since the shape of the plastic zone usually is a contour around the crack tip. The contour itself does not have to be a perfect circle but can be approximated by an expression of $\overline{r}$. **Figure 3.4** depicts such a contour. When $\overline{r}$ increases, $\frac{r}{\frac{1}{\pi}\left(\frac{K_I}{\sigma_y}^2\right)}$ increases towards the case of plane stress.

3.3 Plastic zone models

When considering the shape and size of the plastic zone, it is mostly agreed upon in the research field that the basic shape is the shape of a so called 'dog-bone' for its similarity to an actual dog bone. The plastic zone model shows the extent of plastic deformation in a material around the crack seam. Towards the free surfaces of the material the size of the plastic zone increases due to the phenomena of non-zero stress in the direction normal to the free surface as explained in **Section 3.2.1**.

This dog bone model is presented in **Figure 3.4**. Here the 2D case is presented on the left, where the outer contour represents the case of plane stress and the inner contour represents a plane-strain case. The right part represents a 3D model of the plastic zone.

However, when researching further on the shape of the plastic zone, several authors have stated that the size of the plastic zone differs from the dog-bone shape when performing FEM simulations for crack initiation/propagation cases [54, 55]. The extent of increment in its size towards the free surfaces was found to be less compared to the traditional dog-bone shape and towards the middle of the plastic zone, an increase was found. Whether, this is due to chosen elements, meshing conditions or general FEM ambiguities is unknown.

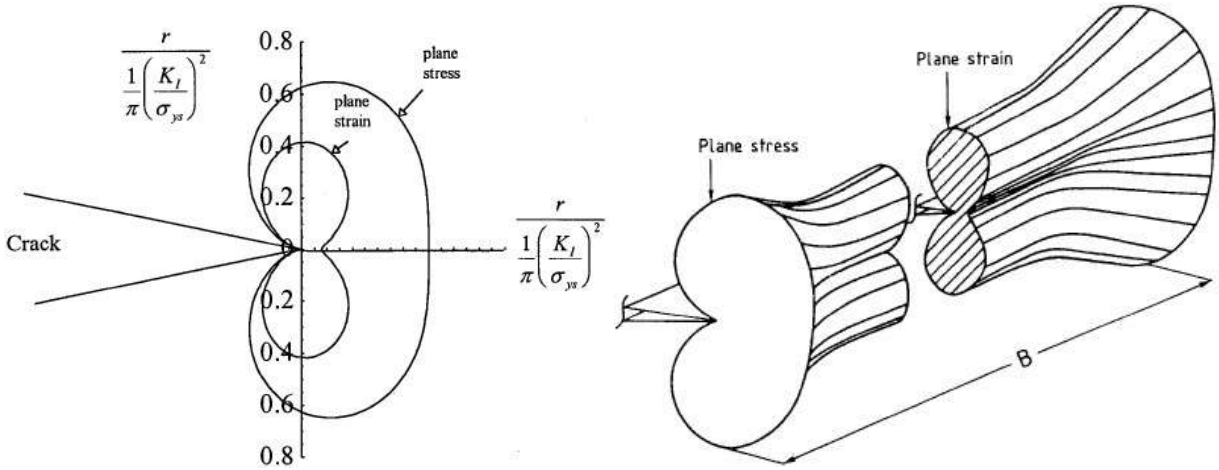

Figure 3.4: Left: 2D case showing plane-strain and plane stress surfaces, Light: 3D depiction of plastic zone 'dog bone' shape [53]

3.3.1 FEM analysis

To investigate the size of a plastic zone and subsequently the necessity of size criteria, it has been chosen to subject the SENB specimen to a FEM analysis. It is widely known that composites are highly anisotropic materials with, in the case of an unidirectional material, orthotropic macroscopic properties; or for a more simple description: transversely isotropic. Investigating the influence of these transversely isotropic properties and corresponding micro mechanics with a FEM analysis is a computationally intensive task since fibers and matrix need to be modeled separately with different properties, let alone the modelling of a composite with in-homogeneous fiber distribution. Furthermore, the randomness and dispersion of the fibers around the crack tip will likely influence the size of the plastic zone and can be a subject of a master thesis on its own. Therefore, it has been chosen to leave this out of the scope of this research.

The orthotropic material properties can be simulated in a FEM analysis by modeling with an element that enables the possibility to use a non-symmetric stiffness matrix. These material properties are presented in **Table 3.2**. Due to the fibers in a longitudinal SENB setup facing upwards in the y-direction, the properties are rotated in Abaqus where the simulation is carried out. More information on the laminate used in the design of the final test protocol and the CF/LMPAEK material in general can be found in **Appendix H**.

Table 3.2: LM/PAEK directional properties

Abaqus	General	Value	Unit	Source/Formulae
E_y	E_{22}	135	GPa	TC1225 data sheet
$E_x = E_z$	$E_{11} = E_{33}$	10	GPa	TC1225 data sheet
$G_{yx} = G_{yz}$	$G_{21} = G_{23}$	4.30	GPa	TC1225 data sheet
G_{xz}	G_{13}	3.80	GPa	$G_{23} = E_{22}/(2 * (1 + \nu_{23}))$
$\nu_{yx} = \nu_{yz}$	$\nu_{21} = \nu_{23}$	0.32	-	$\nu_{12} = V_f * \nu_f + V_m * \nu_m$
$\nu_{xy} = \nu_{zy}$	$\nu_{12} = \nu_{32}$	0.02	-	$\nu_{21} = \nu_{12} * (E_{22}/E_{11})$
$\nu_{xz} = \nu_{zx}$	$\nu_{13} = \nu_{21}$	0.32	-	$\nu_{12} = V_f * \nu_f + V_m * \nu_m$

A CF/LMPAEK SENB specimen has been modeled in Abaqus. The meshed model can be seen in **Figure 3.5**. A plane of symmetry has been applied on the plane of loading, indicated with the blue arced area. Therefore, half the SENB specimen can be modeled. The crack itself is not modeled in the analysis. Instead, a feature in Abaqus called 'Crack Seam' is inserted on the SENB specimen. This feature enables the user to determine the direction of crack propagation. During the meshing of the model, double nodes

will be placed on the crack seam. This allows the mesh to move freely around this crack seam as if these were not fixed to one-another with one node moving to the left and another node, with same coordinates, moving to the right, pulling the crack apart. This crack seam can be seen in **Figure 3.5** as well and is shown by the red line. The blue arrows indicate the direction of crack propagation.

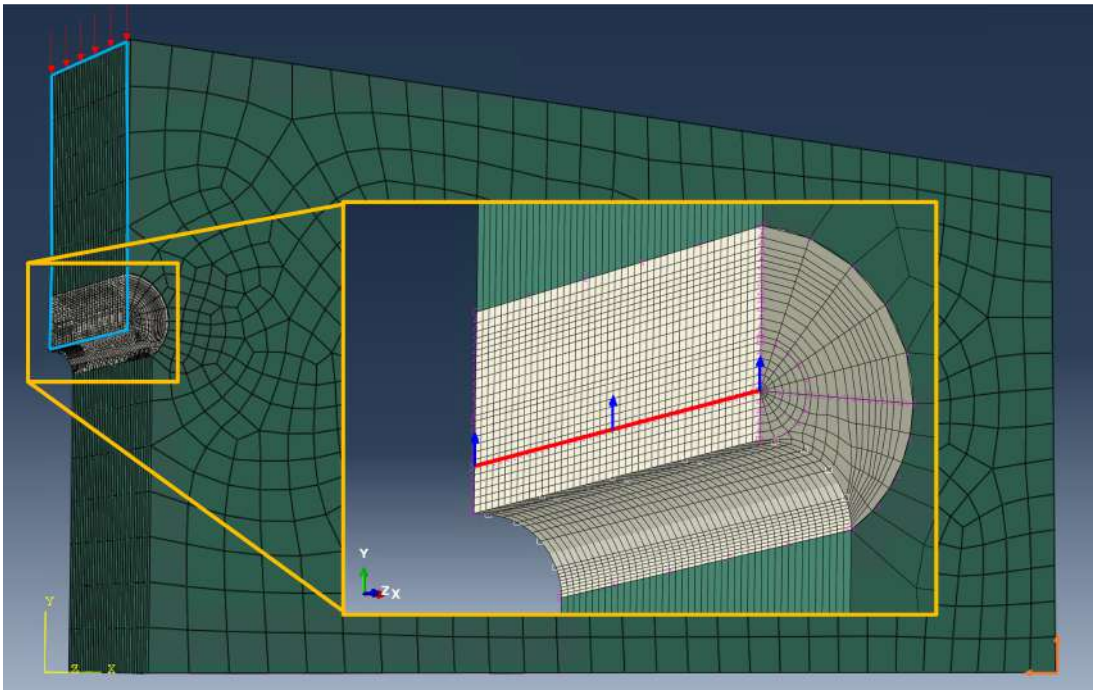

Figure 3.5: Contour integral and coarse mesh including crack seam, crack propagation direction, load and fixtures of a SENB specimen

The elements used in this analysis are a 20-node quadratic brick element for the contour integral mesh (indicated with the beige colour in **Figure 3.5** and encapsulating the plastic region, allowing for a contour analysis) and 8-node linear brick elements for the coarse mesh (indicated by the dark green colour in **Figure 3.5** and defining the rest of the model outside the plastic zone area). The element size used for the course mesh is 1mm and the element size used for the contour integral mesh is 50 µm. The contours used in the same contour integral mesh are split in 10 wedges, placed around the crack tip line. A contour analysis that makes use of the J-integral method (thus suitable for plastic deformation) will take several contours on the mesh and calculate the Virtual Crack Closure (VCC) energy. Furthermore, the model has been loaded with prescribed displacement on the plane of symmetry. This prescribed displacement was devised from real world tests with the same CF/LMPAEK material and dimensions by averaging the displacement at crack initiation, being 0.242mm and indicated in **Figure 3.5** with the red arrows. The model is fixed on the bottom right edge by prescribing the displacement to be zero in all directions, while still allowing for rotations, indicated by the orange arrows in **Figure 3.5**.

The size of the plastic zone is characterized by the volume of material that has yielded. Within an isotropic material, this can be approximated by the volume that has exceeded the yield stress of the material. However, when dealing with CF/LMPAEK, or composites in general, this becomes increasingly difficult due to the random dispersion of fibers in the matrix material. For this analysis it has been chosen to model the SENB specimen as an isotropic material, with transversal isotropic properties as in **Table 3.2**.

The plastic zone in the case of CF/LMPAEK is identified by the volume where the yield of LMPAEK is exceeded, being approximately 90MPa. This value has been obtained out of the data sheet of the matrix material used in Toray Cetex® TC1225, being Victrex® AE250 and can be found in **Appendix H-2**. The resulting shape of the plastic zone is depicted in **Figure 3.6** on the left. It can be seen that, as stated in

Section 3.3, the plastic zone is larger in the middle than the original dog-bone shape. Furthermore, the extent of increment in its size towards the free surfaces was found to be less compared to the traditional dog-bone shape and the overall change in thickness is way less present.

Next to the plastic zone simulation of a transverse isotropic CFRP, a similar simulation has been carried out with only the isotropic LMPAEK polymer matrix material itself. All boundary conditions, loading and way of solving the problem are kept the same. However, the material itself has changed from being a isotropic material with transversely isotropic properties to an isotropic material with isotropic properties. This, to see whether the plastic zone is influenced by this change in material. The resulting shape of this plastic zone is presented in **Figure 3.6** on the right. It can be seen that shape stays practically the same with the plastic zone increasing towards the free surfaces of the specimen. What can be noted as well, is that the size of the plastic zone in crack propagation direction, stays constant over the entire thickness, apart from the free surfaces. For the LMPAEK polymer simulation, the height of the yielded area in between the free surfaces turned out to be larger than that of the CFRP simulation. This can be explained by the fact that isotropic material properties for the simulation of the polymer have been applied, whereas transversely isotropic properties have been applied for the CFRP, having a way larger Young's modulus in the height direction of the specimen due to that direction being the fiber direction. The lower Young's modulus for the isotropic polymer, resulted in more yielded material in the height direction with the same applied deformation.

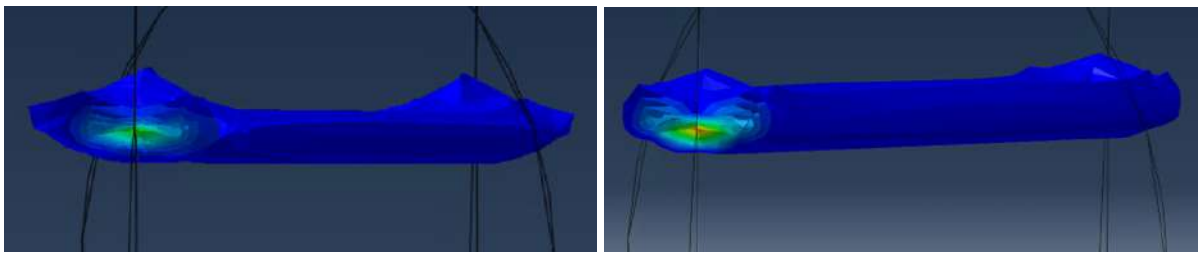

Figure 3.6: Left: CFRP plastic zone simulation. Right: Polymer plastic zone simulation. The iso-surfaces show the Equivalent Plastic Strain (PEEQ), a scalar measure of all the components of equivalent plastic strain at each position in the model, somewhat like the Von Mises stress is a scalar measure of the shear stress at a point.

Figure 3.7 shows a 2D side view of the plastic zones of both the CFRP material and the polymer material. The contours, being isolines of equivalent plastic strain, indicate the 2D shape and size of the plastic zone. It can be seen that the width of both plastic zones is relatively similar due to the same Young's modulus in this direction for both materials. Furthermore, the polymer specimen exhibits more plastic strain in height direction due to it's lower Young's modulus in this direction as stated before.

By taking the size of the plastic zones, characterized by the characteristic length $\overline{r}$ and indicated by the dimensions in the figure, the characteristic length $\overline{r}$ is 400 µm for the CFRP specimen and 350 µm for the polymer specimen. When checking the size criteria as stated in **Section 3.2.1**, the thickness $h(i.e, 4.5mm) > 2.5 * \overline{r}(i.e,\ 0.8mm)$, the crack length $a(i.e., 6.5mm) > 2.5 * \overline{r}(i.e.,\ 0.8mm)$, and the ligament width $(w - a_0)(i.e., 7.5mm) > 2.5 * \overline{r}(i.e.,\ 0.8mm)$. Thus, it can be stated that all size criteria are satisfied for both materials.

The ISO 13586 standard has an annex describing the fracture toughness testing of Short Fiber Reinforced Polymers (SFRPs). To cite the standard: "With plastics containing short fibres it is questionable whether the notion of plastic yielding can apply to the material as a whole and hence whether the size of a 'plastic zone' can be identified at all. Experience has shown that, for materials of this kind, results obtained for K_{Ic} and G_{Ic} are practically invariant with specimen dimensions varying in the range suggested by this document. Size criteria need therefore not be checked with this class of materials." [2]. In reality, when testing CFRPs, the size criteria might not always be met due the fact that for a specific specimen a higher maximum force was needed to initiate the crack which is all dependent on the local micro-structure of the material and corresponding properties. Whether the size criteria become obsolete

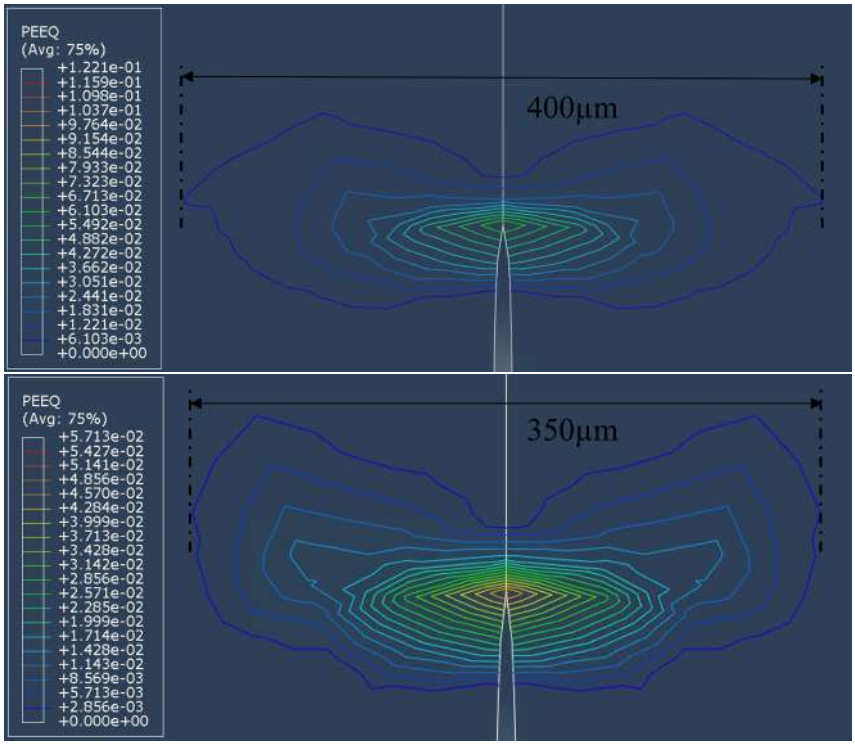

Figure 3.7: Left: plastic zone of a CFRP with 2D isolines. Right: plastic zone of a LMPAEK with 2D isolines. Again, the isolines show the equivalent plastic strain. A value of > 0 indicates, the material has yielded.

for intralaminar SENB specimens, can only be proven empirically by checking whether the results for K_{Ic} and G_{Ic} differ for this class of materials within the specimen dimension ranges given in the ISO 13586 standard. This is something that is not in the scope of this research.

3.3.2 Analysis of previous SENB tests of CF/LMPAEK samples

After analyzing the size of the plastic zone with FEM, test results can also give insight in the size of this plastic zone and subsequent without the need of complex models. Preliminary SENB specimens cut from a similar laminate made from the same CF/LMPAEK material have been tested on Mode I fracture toughness before at the University of Twente [56]. The data of these specimens have been analyzed by calculating the characteristic length $\overline{r}$ for each of the 12 tested specimens. It became apparent that the value of the characteristic length $\overline{r}$, differed a lot between specimens (i.e., a relative standard deviation of approximately 18%).

What is of particular interest is the way the several dimensions of a SENB specimen (i.e., height, width, length, crack length and, resulting specimen stiffness) influence this value of the characteristic length, and subsequently the plastic zone, theoretically. According to the ISO 13586 standard, the characteristic length can be calculated in 2 ways as explained in **Section 2.1** and **Equation (2.8)** and **Equation (2.9)** respectively.

Table 3.3 shows the theoretical characteristic length $\overline{r}$ for the 12 tested specimens, calculated according to the relation proposed in ISO 13586 and reproduced in **Appendix C**. Next, a safety factor of 1.5 has been applied on the characteristic length $\overline{r}$ as a means of separating values close and over $2.5\overline{r}$ from values further below $2.5\overline{r}$. This since, according to the size criteria, h and a and $(w - a_0)$ should all be larger than $2.5\overline{r}$. The separation has been done to find out whether certain parameters were the cause of the larger $\overline{r}$. The specimens that did not meet this factor are presented in **Table 3.4a** and all the specimens that did meet this factor are presented in **Table 3.4b**. Next, several parameter ratios have

been calculated. It has been chosen to investigate dimension ratios since individual dimensions did not show a noticeable change with changing values of $\overline{r}$. When looking at the averages of the ratios h/w and a/w for both tables, it is present that the difference in characteristic length $\overline{r}$, is not due to this since the difference is insignificant.

Furthermore, the stiffness of specimens has been added. This stiffness is calculated by taking the slope in the linear-elastic area of the force-displacement plots of each specimen. What can be seen is that the average specimen stiffness in **Table 3.4a** is higher than that in **Table 3.4b**. Thus, it can be concluded that specimen stiffness is the main contributor to a changing characteristic length.

Table 3.3: Characteristic length $\overline{r}$ for 12 analyzed samples calculated in 2 ways and safety factor check

Specimen	$\overline{r}_1$ **[mm]**	$\overline{r}_2$ **[mm]**	$\delta\overline{r}_{1,2}$	$2.5 * \overline{r}_1$ **[mm]**	h **[mm]**	$(2.5 * \overline{r}_1)/h$	**within** s_f **of 1.5 on** $\overline{r}$
1	1.180	1.077	-9%	2.950	4.440	66%	yes
2	1.020	0.932	-9%	2.550	4.440	57%	yes
3	1.306	1.207	-8%	3.260	4.445	73%	no
4	1.050	0.928	-12%	2.630	4.435	59%	yes
5	0.808	0.776	-4%	2.020	4.435	46%	yes
6	1.097	0.954	-13%	2.740	4.435	62%	yes
7	1.382	1.295	-6%	3.450	4.430	78%	no
8	1.567	1.469	-6%	3.920	4.425	89%	no
9	1.081	0.989	-9%	2.700	4.420	61%	yes
10	0.918	0.946	3%	2.300	4.415	52%	yes
11	1.020	1.049	3%	2.550	4.415	58%	yes
12	1.192	1.141	-4%	2.980	4.415	67%	yes
rel. std. dev.	**18.29%**	**17.81%**					

Table 3.4: Ratios and stiffness average of specimens within and outside 1.5 s_f on $\overline{r}$

(a) All values outside 1.5 s_f on $\overline{r}$

Specimen	**Ratio** h/w	**Ratio** a/w	S **[N/mm]**
3	0.315	0.458	773
7	0.315	0.451	735
8	0.315	0.457	733
average	**0.315**	**0.455**	**747**

(b) All values within 1.5 s_f on $\overline{r}$

Specimen	**Ratio** h/w	**Ratio** a/w	S **[N/mm]**
1	0.315	0.449	737
2	0.315	0.447	716
4	0.315	0.452	724
5	0.315	0.444	734
6	0.315	0.451	692
9	0.314	0.447	729
10	0.314	0.444	680
11	0.312	0.446	685
12	0.312	0.443	721
average	**0.314**	**0.447**	**713**

To decrease the size of the characteristic length $\overline{r}$ theoretically, the solution would be to decrease the stiffness of a single specimen. This can be done in 3 ways. The first way is to increase the length l of the specimens to enable a longer span S in the SENB setup. The second way is to decrease the laminate thickness h and the third way is to decrease the height w of a specimen. When decreasing the height of a specimen, the remaining ligament width where a crack can be tracked decreases as well which is unwanted since the possibility of tracking the crack propagation for a longer crack length is preferred because longer crack propagation means more data, less interpolation and subsequently a more accurate R-curve. Decreasing laminate thickness might decrease stiffness, but it decreased the size of the plane-strain area as well. Therefore, increasing the span S of a specimen is preferred. This way, the plane-strain area stays the same and there is no influence on the maximum crack length that can be tracked.

With the gained knowledge of the FEM plastic zone analysis and the analysis of previous CF/LMPAEK specimens, the specimen dimensions have been devised. As mentioned before in **Section 3.2**, the length of a specimen has been set to 70mm with a span of 65mm, a thickness of 4.3mm, a height of 14mm, and an initial crack length of 6.5mm (i.e., excluding pre-crack cutting) is present. ISO 13586 recommends $2 < w/h < 4$. With a given laminate thickness of 4.3mm, the height could vary between 8.6 and 17.2mm. Simply taking the maximum height for the longest crack tracking would mean that a longer v-notch is needed, to fall within limits of the standard (i.e., $0.45 \leq a/w \leq 0.55$). It basically comes down to using more material in a specimen, while the gain is limited. The previously analyzed specimens with a height of 14mm showed promising results, as well in fracture toughness as in the R-curve. Therefore, the height of 14mm has been applied to the Round-Robin specimens as well. The span of 65mm is an increase upon the span of 46mm used in the analyzed tests. This is done to decrease the stiffness as mentioned in the paragraph above. Lastly, the v-notch depth is set at 6.5mm, falling just within the minimum a/w value of 0.45 (i.e., approx. 0.464) to allow for the longest possible crack tip tracking.

3.4 Specimen Preparation

The section will explain the experimental methods used for the preparation of the specimens. By using the experience of previous researchers, fellow students and trial and error, the most suitable method for the specimen preparation steps have been found. This section will elaborate on the sawing, machining, and most importantly, the pre-crack cutting of the specimens, resulting in the sharpest possible pre-crack.

3.4.1 Sawing

In designing the test protocol, all the experimental methods have been evaluated on the same material as used for the Round-Robin test, however originating from a different laminate. This material is a CF/LMPAEK composite with a $[0]_{34}$ lay-up, having a thickness of 4.4mm. The laminate itself was discarded since a c-scan showed irregularities in thickness of this material, making it unsuitable for actual tests where results mattered. However, this made it perfect for use in designing a test method where the method itself mattered more than the results.

All specimens were cut with a water-cooled diamond circular saw blade, available at the University of Twente. The specimens measured 70mm by 14mm. Using a water cooled diamond saw is necessary when cutting composite materials since the highly abrasive nature of this class of materials.

3.4.2 Machining

After the sawing of the specimens, the next step is to create the first slot prior to the pre-crack. The ISO 13586 standard does not provide any details on machining of notches other than the fact that they should be sharp, meaning a v-notch.

However, the ISO 2818:2018 standard for preparation of test specimens by machining provides information on machining v-notches in thermoplastics and recommends medium speed milling with 200 up to a 1000 rpm, with a tool diameter of 60 to 80mm, a cutting speed of 50 to 250 m/min and a feed rate of 0.07 to 2 m/min [57]. Whether this translates to the machining of composites, can easily be discovered by machining several v-notches in specimens cut from the discarded CF/LMPAEK laminate.

For the machining of Composite SENB specimens, a special holder was created. This holder can be placed in the clamp of a milling machine. The holder has 2 sides, exactly 90 degrees apart from each other. This ensures that the notch is at a constant distance from the left side of the specimens. The specimens will be stacked as depicted in **Figure 3.8** on the left. Between the specimens, several pieces of PMMA plastic are placed. This is done to mainly avoids burrs on the composite SENB specimens. Next, the specimens are clamped by 2 bolts and a bridging piece of steel. Between the specimens and this piece of steel, a thin part of triplex is placed to avoid damaging the composite material while clamping.

This can be seen in **Figure 3.8** on the right. The holder itself is then placed in a milling machine, and the designated clamp fixates the specimens.

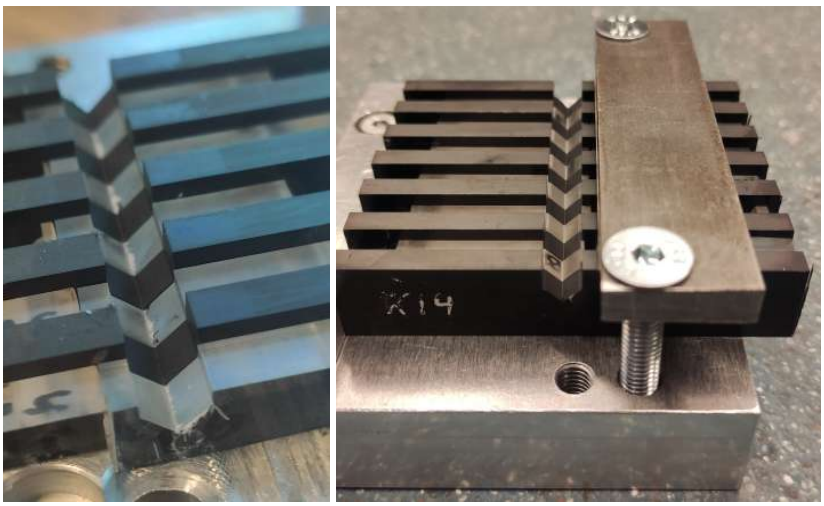

Figure 3.8: Left: PMMA material between specimens to prevent burrs, Right: clamping method prior to machining SENB specimens

Trying machining with a feed rate of 50mm/min and an rpm of 2500rpm resulted in a very rough surface with melted LMPAEK, as can be seen in **Figure 3.9** on the left. This figure depicts the specimens photographed from the top after machining. The melting of LMPAEK was due to a very high rotational speed and a too low feed rate, creating too much heat and melting the polymer matrix material. Next, the feed rate was increased to 200mm/min and the rpm decreased to 2000rpm. This resulted in a clean cut and no melted LMPAEK as can be seen in **Figure 3.9** on the right.

Next, it has been tried to machine the v-notch in 2 different steps to avoid ruining the 90 degree tool within a few runs through some specimens, since the material to be cut is extremely abrasive. First a 120 degrees, 6mm uncoated solid carbide chamfering cutter tool was used at mentioned rpm and feed rate to cut the first 5.5mm. The final step was done with a 90 degree, 6mm uncoated solid carbide chamfering cutter tool, as well with same rpm and feed rate. The result is a stepped line in **Figure 3.10** on the right. Both tools used are manufactured by Garant®. Their product numbers are 208080 6 for the 120 degrees tool and 208070 6 for the 90 degrees tool.

However, after inspection, no visible sign of wear was detected on the 90 degree tool and it has been decided to keep the machining step simple and machine the entire 6.5mm depth in one go. This proved to work just as well and produced a clean machined area.

3.4.3 Pre-crack cutting

After creating the first notch in the SENB specimen, the next step would be to create a pre-crack in this notch to simulate the existence of a natural crack, also known as 'broaching' but later renamed to pre-crack cutting. The sharper this crack can be, the closer it would be to a crack that would form due to outside forces. In the world of fracture toughness tests, this is a topic of major importance. When a sharp pre-crack cannot be formed, the resulting K_{Ic} is meaningless since the material would crack at a lower K_{Ic} in a real world application. In general it can be stated that the sharper the pre-crack, the lower the K_{Ic}. This, since a sharper pre-crack translates to a smaller plastic zone, making the material around the crack more ductile and a lower amount of energy J is needed to crack a particular area in m^2.

The ISO 13586 standard mentions 3 ways of creating a pre-crack in a SENB specimen: [2]

- A natural crack can be generated by tapping on a new razor blade placed in the notch (it is essential

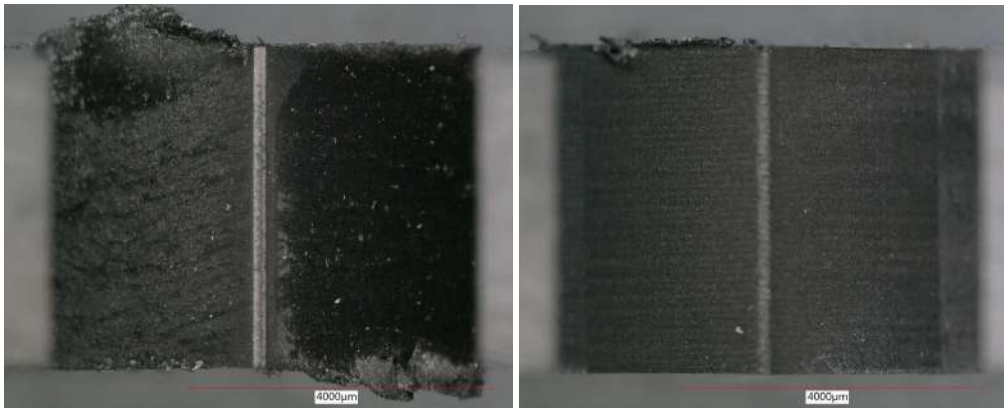

Figure 3.9: Left: surface area after machining at 2500rpm with 50mm/min, Right: surface area after machining at 2000rpm with 200mm/min

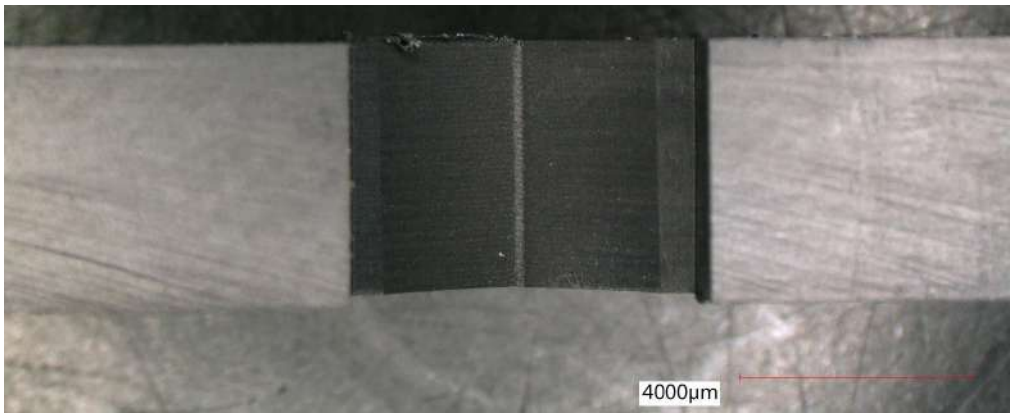

Figure 3.10: Stepped area due to machining with 2 different tools

to practice this since, in brittle test specimens, a natural crack can be generated by this process, but some skill is required in avoiding too long a crack or local damage). The length of the crack thus created shall be more than four times the original Notch Tip Radius (NTR).

- If a natural crack cannot be generated, as in tough test specimens, then sharpen the notch by sliding a razor blade across the notch. Use a new razor blade for each test specimen. The length of the crack thus created shall be more than four times the original Notch Tip Radius (NTR).
- Cooling tough test specimens and then performing razor tapping is sometimes successful. Pressing the blade into the notch is not recommended because of induced residual stresses and thus a higher K_{Ic}

It should be mentioned again that this standard is for testing of plastics and has an annex with which the standard could also be used for the testing of SFRPs, as mentioned before. For the notching of a short fiber reinforced plastic SENB specimen, the standard recommends the second pre-cracking method above and advises against using the first or third method since it is a difficult practice on its own and becomes increasingly difficult and risky when dealing with this class of materials. Furthermore, the standard mentions the fact that the crack tip sharpness is generally less critical with this class of materials than with other classes of plastics. A NTR of ≤ 15 µm is usually sufficiently sharp. Thereafter, the quality of the notch and the damage produced in front of it by the notching itself should be assessed by microscopic examination. Even so, the sharpness and wear of the blade shall be assessed periodically by microscopic examination.

When taking all this into account, it can be said that neither of the methods are particularly reliable, reproducible and consistent, especially when using it for the pre-crack cutting of CFRPs. Therefore, a new cutting method using an incremental cutting device (e.g., a microtome) was brought forward by the ESIS TC04 [50]. This method can be found in **Appendix D**. A microtome is a machine, originally used for slicing extremely thin slices of a material. They are often used prior to microscopy in the preparation of samples [58]. Next to a microtome, dedicated equipment is available such as a Instron Ceast Specimen Preparation Notching machine [59].

ESIS TC04 [50] has proposed a method which makes use of the microtome where a notch can be generated in a SENB specimen using sharpened cutting blades, while being able to control the cutting speed, cutting depth, step size, and most importantly the consistency. When tapping or sliding a razor blade, all of these parameters are controlled by the human hand and way less accurate, consistent and this methods is thus unreliable and will influence the K_{Ic} results. Therefore, it has been decided to implement and edit this cutting method wherever needed to be suitable for use on CFRPs in the preparation of SENB samples for the Mode I intralaminar fracture toughness testing.

3.4.3.1 Method Outline

This section will introduce the cutting method which makes use of a microtome. The various steps will be explained and choices made to perfect the cutting method for use in the final protocol will be elaborated wherever necessary. The cutting cycle itself, including a few minor changes that will be presented in **Section 3.4.3.2**, is presented in **Figure 3.11** on the left. Furthermore, the used microtome itself is presented on the right in the same figure.

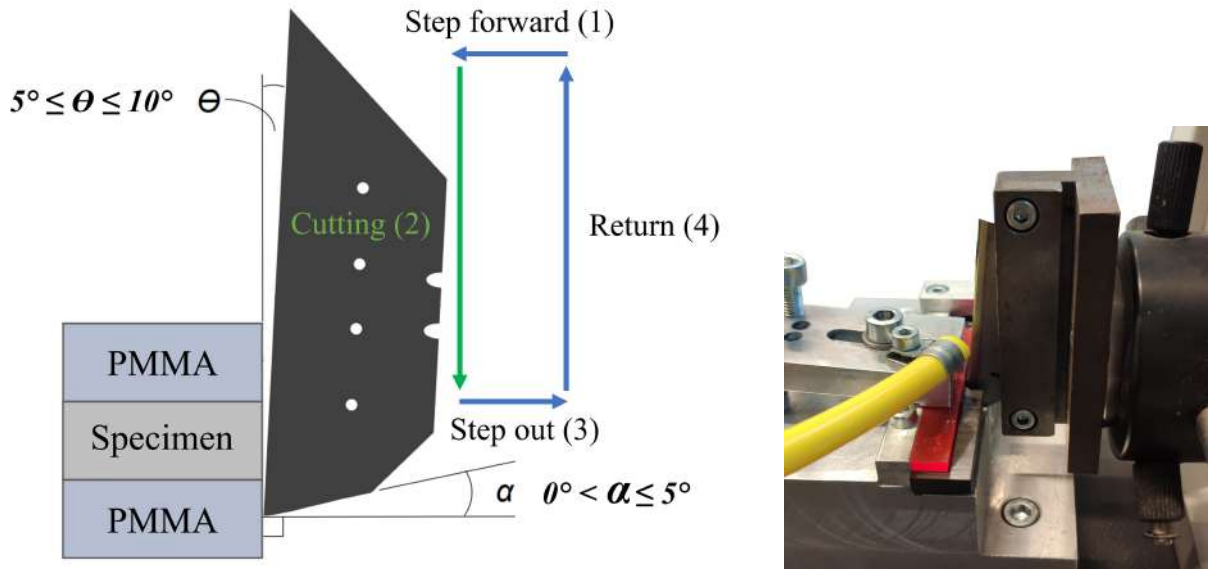

Figure 3.11: Left: Blade orientation and cutting cycle steps [50], Right: microtome used in preparing SENB specimens

One cycle consists of a forward step of 20 µm for the first millimeters to cut and a forward step of 10 µm for the final 0.1mm. The cutting is performed in step 2, where the blade slices through the material. Step 3 is the step out of the material, or retraction. Finally, step 4 brings the blade back up to its first position, whereafter the cycle is repeated. The depth of the cut can be controlled by counting the number of cycles.

The blades are sharpened at an angle range θ and the angle range α as depicted in **Figure 3.11**. Lowering θ, increases friction and non-perpendicular notches and create blunt crack tips, whereas increasing θ, results in the risk of damage to the blade. Lowering α would result in pushing/ploughing into the specimen, whereas increasing α would again increase the risk of damage to the blade. This all means

that the original cutting surface of the blade is not the intended cutting surface in this method and the blade needs to be sharpened by wet sanding.

Figure 3.12 shows a block-diagram, showing the different steps taken in creating a pre-cracked specimen. **Appendix A** elaborates on the different steps and provides a detailed description.

Figure 3.12: Block diagram indicating the different steps to be taken to create a pre-crack according to ESIS TC04 [50]

3.4.3.2 Agreements and changes with the proposed method in pre-cracking composites

The ESIS TC04 method has been looked into regarding the suitability for cutting CF/LMPAEK. As a result, several (minor) changes have been made in the application of this method. However, the method has largely stayed the same.

The method recommends the use of Stanley Carbide® blades. Previous results have proven that this type of blade produced the sharpest NTR and the smallest damage at moderate failure rates. Furthermore, far less promising results have been obtained with Stanley 1992N®, Stanley Fatmax®, and Promat 817766 blades [50]. However, Stanley Carbide® blades are prone to one failure that seems to reoccur: brittle failure. These blades have a higher hardness than the other ones. Although this blade type pro-

duces sharper NTRs due to its higher abrasion resistance on polymer specimens, it also makes the blades prone to brittle failure next to normal wear, which is sadly unavoidable since it occurs randomly and cannot be accounted for while keeping the same pre-crack sharpness. An example of this brittle failure, induced by the cutting of CFRP specimens, can be seen in **Figure 3.13** on the right. The left side of the figure depicts the same blade prior to failure. The brittle failure is mostly present at the tip of the blade which is in direct contact with the specimen while cutting. Due to sudden peak forces when entering the CF/LMPAEK material, brittle failure occurs here.

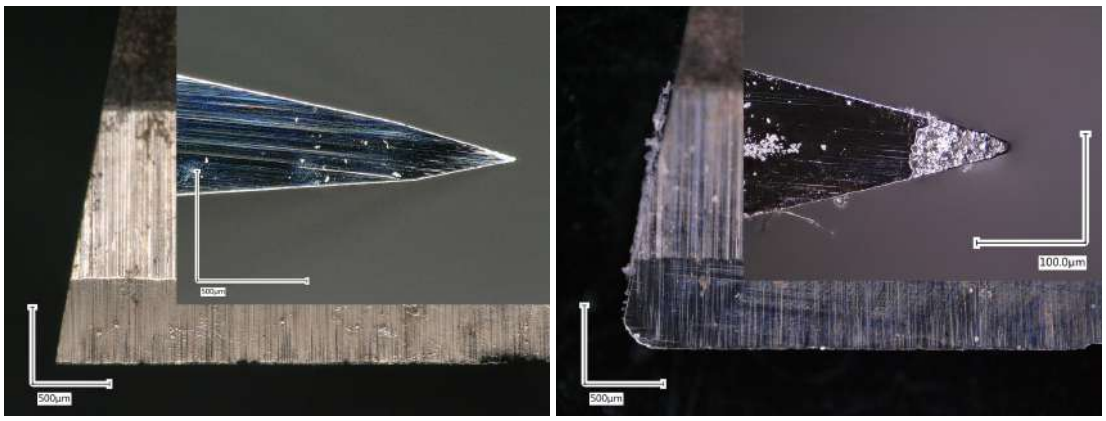

Figure 3.13: Left: sharpened blade (side and front view), Right: same blade after brittle failure (side and front view)

It has been chosen to continue with these Stanley Carbide® blades for the sharpest pre-crack possible since a specimen can simply be discarded in a test if the crack is less sharp than average due to brittle fracture. Furthermore, the choice has been made to experiment with the pre-crack depth in creating the sharpest pre-crack possible, with the least amount of blade wear.

Furthermore, the method sets the limit of the amount of specimens to be cut at once at three. As already mentioned, a carbon fiber composite is an extremely abrasive material and in fear of damaging the blade too much it has been chosen to cut only one specimen at a time. It has also been opted to use the sharpened blade side for the cutting of one specimen only. Although this is more labor intensive with more blades to be prepared and will require more time, it is a right step towards the sharpest possible pre-crack.

Next, two pieces of PMMA sacrificial material are used, one on each side of the specimen as depicted in **Figure 3.11**. The ESIS TC04 method only recommends using one piece of sacrificial material at the bottom of the specimen to prevent burrs and delamination in cutting. However, clamping the fixture down directly on the specimen, prior to cutting, is feared to cause damage on the composite as well, possible influencing the micro structure in the area to be tested. Therefore, a sacrificial beam is also used on top of the specimen. These beams are made from a much more compliant polymer material and absorb the clamping force. Besides, the sacrificial polymer beams are cut to width to match the depth of the machined notch.

Furthermore, the cutting method proposes vortex cooling to cool the blade tip down to -10°C to prevent generator heat to damage the polymer. However, as seen in **Figure 3.13**, the blades are already prone to brittle failure and decreasing the temperature of the tip would only increase the brittleness of the material, quite similar to the hull of a certain famous ship that hit an iceberg in 1912 and was left full of holes after the ice cold water of -2°C had made the steel more brittle.

3.5 Analysis of preliminary results

To get a better understanding of the entire process for determining the fracture toughness and in seeing which new implementations work and which do not in determining the G_{Ic} and K_{Ic}, there is a need

for preliminary testing. As soon as consistent, precise and reproducible results are obtained, the final specimens can be tested.

For the preliminary tests, rest material has been used. This material was a CF/LMPAEK $[0]_{30}$ laminate with a thickness of 4.4mm. This laminate has been rejected for its inconsistent thickness. Specimens were cut out of this laminate, having the same dimensions as described in **Section 3.2**. The machining of the crack has been done in two steps as described in **Section 3.4.2**. Afterwards the pre-crack cutting was done up to different depths of 0.1, 0.2, 0.55, and 0.8mm. Here, a depth of 0.8mm corresponds to a depth of 4xNTR, recommended by the ESIS TC04 method. This varying of depth is done to try and find the relation between cutting depth, the sharpness and wear of the blade, and the change in K_{Ic} and G_{Ic} as described in **Section 3.5.1**.

In total 18 preliminary specimens were tested, having different machining steps, cutting depths and paint/Typp-ex applied. The conditions for all these specimens are presented in **Table 3.5**. Furthermore, a lower loading rate (i.e., 0.5 mm/min) has been used on the first few specimens to ease the adjusting of the crack tip tracking, since the crack will propagate slower with a lower loading rate. When it came apparent that the tracking was working well, the loading rate was changed to 1mm/min.

Table 3.5: Specimen specific testing conditions

Specimen	Loading rate	Cutting depth	Machining steps	Contrast layer
X1	0.5 mm/min	0.800 mm	120°tool (5.5mm), 90°tool (1mm)	thin matte white spray paint
X2	0.5 mm/min	0.800 mm	120°tool (5.5mm), 90°tool (1mm)	thin matte white spray paint
X3	1 mm/min	0.800 mm	120°tool (5.5mm), 90°tool (1mm)	thick matte white spray paint
X4	0.5 mm/min	0.800 mm	120°tool (5.5mm), 90°tool (1mm)	thin matte white spray paint
X5	0.5 mm/min	0.800 mm	120°tool (5.5mm), 90°tool (1mm)	thin matte white spray paint and Typp-Ex
X7	1 mm/min	0.800 mm	120°tool (5.5mm), 90°tool (1mm)	thin matte white spray paint and Typp-Ex
X8	1 mm/min	0.100 mm	120°tool (5.5mm), 90°tool (1mm)	thicker matte white spray paint
X9	1 mm/min	0.100 mm	120°tool (5.5mm), 90°tool (1mm)	thicker matte white spray paint
X10	1 mm/min	0.200 mm	120°tool (5.5mm), 90°tool (1mm)	thicker matte white spray paint
X11	1 mm/min	0.550 mm	120°tool (5.5mm), 90°tool (1mm)	thicker matte white spray paint
X12	1 mm/min	0.400 mm	120°tool (5.5mm), 90°tool (1mm)	thicker matte white spray paint
X13	1 mm/min	0.400 mm	120°tool (5.5mm), 90°tool (1mm)	thicker matte white spray paint
X14	1 mm/min	0.200 mm	120°tool (5.5mm), 90°tool (1mm)	thicker matte white spray paint
X15	1 mm/min	0.200 mm	90°tool (6.5mm)	thicker matte white spray paint
X16	1 mm/min	0.200 mm	90°tool (6.5mm)	thicker matte white spray paint
X17	1 mm/min	0.100 mm	90°tool (6.5mm)	thicker matte white spray paint
X18	1 mm/min	0.100 mm	90°tool (6.5mm)	thicker matte white spray paint
X19	1 mm/min	0.000 mm	90°tool (6.5mm)	thicker matte white spray paint

3.5.1 Towards the 'perfect' pre-crack

As mentioned before, the main goal regarding pre-crack cutting is recreating the most naturally occurring, thus sharpest pre-crack possible, proving a challenge in the recreation of this.

The ISO 13586 standard recommends a pre-crack depth of more than 4 times the NTR of the machined notch, to avoid too long a crack or local damage. Next to that, the method designed by ESIS states a cutting depth of 1.3mm. After research, it became apparent that this value of 4 times the NTR (approximately 1.3mm) is a remnant value from the testing of metal SENB specimens in the second half of the 20th century and meant for isotropic, homogeneous materials. This rises the question whether this is even applicable to a CFRP at all due to its orthotropic material properties and non-homogeneity. Therefore, it has been chosen to find the best cutting depth empirically for a CFRP as part of this research and not to rely on the previously mentioned standards.

The G_{Ic} $[J/m^2]$, can be seen as a measure of crack sharpness. The G_{Ic} is based on the load and displacement at crack initiation, being the input energy. When the G_{Ic} is high, more energy needs to be put into the initiation of fracture, whereas when the G_{Ic} is low, the fracture in the SENB sample will be

initiated at a lower input energy. Similarly, the K_{Ic} is reduced when a sharper pre-crack can be created.

To determine the pre-crack length that recreates a naturally occurring crack the best, thus having the sharpest crack, the following method has been devised. First, several specimens are machined from the discarded laminate, whereafter several pre-cracks are cut into the specimens at various depths. To be able conclude something about the relation between cutting depth and crack sharpness, only the cutting depth parameter should be changed and all other parameters be kept consistent. Therefore, all specimens were cut with a new sharpened razor blade, and afterwards tested at the same quasi-static loading rate of 1mm/min.

Prior to testing, all specimens have been microscopically examined. The pre-crack Notch Tip Diameter (NTD) after pre-crack cutting has been measured and the overall quality/neatness of the pre-crack has been examined; both on either side of the specimen. Examples of the acquired images for the pre-crack NTD and the pre-crack quality/neatness can be found in **Figure 3.14** on the left and right respectively. Furthermore, the initial crack length a_0 has been determined by microscopic examination as well. This value is used in the calculation of G_{Ic} and K_{Ic}. On a side note, it should be mentioned that all others dimensions of the specimens: width h, height w, and length l are measured twice on either side and averaged for use in calculations later on.

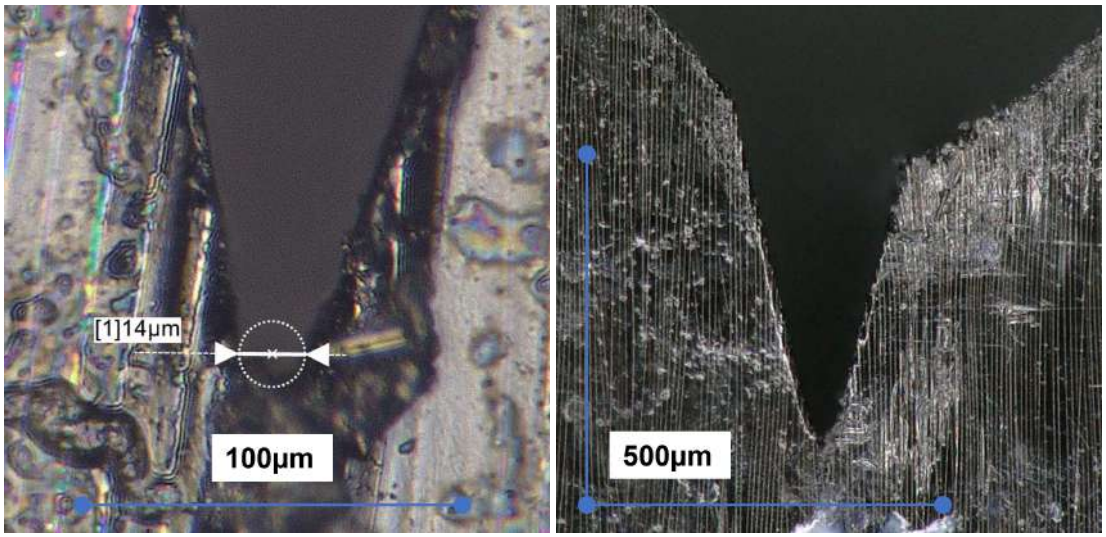

Figure 3.14: Left: Notch tip diameter of specimen X16 (zoomed in from the right figure), Right: Pre-crack of specimen X16 after pre-crack cutting

Table 3.6 shows a summary of the results of the tested specimens in order to find the best cutting depth statistically. The values have been calculated according to ISO 13586. Higher values of the maximum force, G_{Ic} and K_{Ic} have been highlighted red while lower values have been highlighted green, representing a better pre-crack sharpness. The same is done for the maximum force reached during testing F_{max}, notch tip diameter, characteristic length $\overline{r}$ and stiffness C. It should be noted that in calculating the average and the relative standard deviation, specimen X19 was not taken into account since this specimen has not been pre-cracked. This, to see what the results would be without generating a sharp crack. As can be seen, the G_{Ic} and K_{Ic} are significantly higher than the average, indicating the effect of pre-crack cutting.

Furthermore, these results have been displayed in **Figure 3.15** where bar charts are presented, grouping the different cutting depths, and corresponding results of G_{Ic}, K_{Ic}, and NTD. When looking at the difference in K_{Ic} over the different cutting depths, a very slight upwards trend is visible with increasing cutting depth. The average of the K_{Ic} values of specimens cut at 0.1mm is lower than the average of specimens cut at 0.8mm for example (3.31 and 3.39 $MPa\sqrt{m}$ respectively). Furthermore, when looking at the G_{Ic}, a similar trend is visible where the average seems to very slightly increase with increasing

Table 3.6: Summary of preliminary SENB test results and relative parameters

Specimen	Rate	Cut depth	F_{max} [N]	NTD [µm]	G_{Ic} $\left[\frac{J}{m^2}\right]$	K_{Ic} $[MPa\sqrt{m}]$	$\overline{r}$ [mm]	C $\left[\frac{N}{mm}\right]$
X1	0.5 mm/min	0.800 mm	182	15	1706	3.22	1.40	626
X2	0.5 mm/min	0.800 mm	188	14	1779	3.24	1.43	630
X3	1 mm/min	0.800 mm	199	19	1974	3.60	1.75	654
X4	0.5 mm/min	0.800 mm	187	15	1712	3.24	1.42	646
X5	0.5 mm/min	0.800 mm	203	7	1978	3.51	1.61	638
X7	1 mm/min	0.800 mm	202	23	1885	3.50	1.64	676
X8	1 mm/min	0.100 mm	178	8	1638	3.17	1.41	643
X9	1 mm/min	0.100 mm	194	8	1886	3.51	1.66	650
X10	1 mm/min	0.200 mm	196	20	2017	3.62	1.76	625
X11	1 mm/min	0.550 mm	183	30	1982	3.62	1.72	572
X12	1 mm/min	0.400 mm	170	20	1727	3.31	1.57	609
X13	1 mm/min	0.400 mm	171	13	1768	3.31	1.62	619
X14	1 mm/min	0.200 mm	174	16	1811	3.26	1.60	622
X15	1 mm/min	0.200 mm	190	14	1916	3.52	1.71	638
X16	1 mm/min	0.200 mm	180	14	1835	3.31	1.58	621
X17	1 mm/min	0.100 mm	185	4	1809	3.33	1.54	635
X18	1 mm/min	0.100 mm	182	4	1646	3.24	1.42	652
X19	1 mm/min	0.000 mm	236	1000	2806	4.18	2.41	652
		σ	**10.27**	**6.89**	**120.51**	**0.16**	**0.12**	**22.60**
		Average	**186.07**	**14.35**	**1827.61**	**3.38**	**1.58**	**632.76**
		%STD	**5.52%**	**48.01%**	**6.59%**	**4.61%**	**7.86%**	**3.57%**

cutting depth. To really be able to indicate a trend, more data is needed. However, no more specimens were available. The notch tip diameter however, does indicate a more clear trend. The average increases significantly with increasing cutting depth.

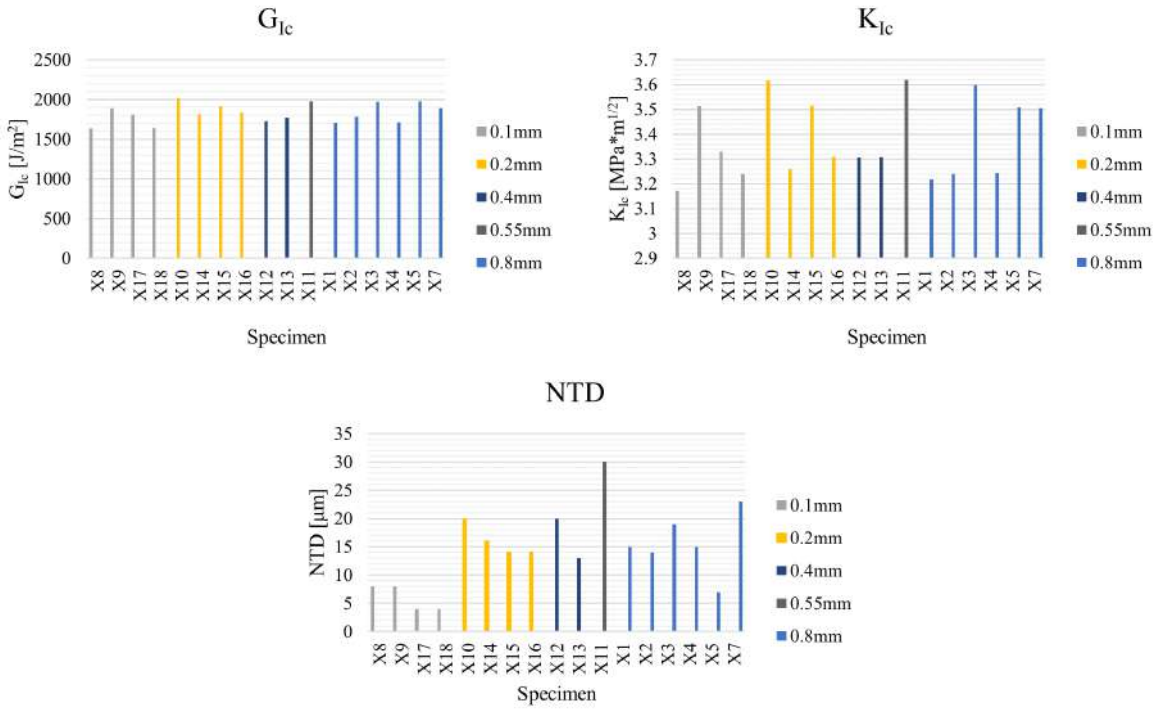

Figure 3.15: Top: Grouped preliminary G_{Ic} results, Right: Grouped preliminary K_{Ic} results, Bottom: Grouped preliminary NTD results

Seeing the G_{Ic} and K_{Ic} and especially the NTD slightly rise on average with increasing cutting depth, indicates the fact that the NTD becomes less sharp the deeper the cut is. Whether this effect becomes less apparent when the NTD becomes increasingly small and there exists some critical NTD, is unknown. However, the statement made in ISO 13586 indicates that this is the case: "Crack tip sharpness is generally less critical with this class of materials (SFRPs) than with other classes of plastics: a notch tip radius of $\leq$ 15µm, as can be easily obtained by machining the notch with a fresh razor blade, is usually sufficiently sharp." [2].

To determine whether the apparent trend is due to the abrasive nature of a CFRP, the blades used in the cutting of these specimens have been examined after each specimen was cut by taking pictures of the blade area used to cut. This, from the side as well as normal to the cutting surface. A collage of the microscopic examination of 3 blades, used for cutting depths of 800µm, 550µm, and 100µm is presented in **Figure 3.16**. As expected, it can be seen that blade 6 and blade 13 have higher wear than blade 7, with the latter used for cutting 100µm instead of 800µm. Abrasive lines can be seen on the side of the blades, likely due to fibers. Furthermore, the damaged area due to pre-crack cutting is shaded with translucent red. It can be seen that the damaged area decreases where the pre-crack depth decreases. Concluding, it can be said that a deeper cutting depth reduces the pre-crack sharpness. This is indicated by an increase in G_{Ic}, K_{Ic}, NTD and higher wear on the corresponding blades used.

The fracture surface and pre-crack sharpness have been analyzed with use of SEM (Scanning Electron Microscopy) as well. **Figure 3.17** shows SEM images of specimens X7, X17 and X19 after pre-crack cutting and testing. The specimens are fully cracked by swiftly tapping one end of a specimen while having the other end clamped, fracturing the specimen by brittle fracture. Then, one half of each specimen was analyzed. The images are views normal to the fractured surface and encapsulate part of this fractured surface as well as the pre-crack. When comparing the crack tip of specimen X7 (800µm pre-crack) and X17 (100µm pre-crack), it can be seen that in specimen X7 several bundles of fibers are separated from one half of the specimen outside of the dedicated notch tip, leaving lots of 'craters' in the fractured area. Specimen X17 however, shows way less of these 'craters' indicating less separated fiber bundles. This is also indicated by the transition of the pre-cracked area into the fractured surface. Specimen X7 shows an uneven transition, whereas specimen X17 almost shows a horizontal transition line, apart from a few 'craters'. This can also be explained by the NTD of X7 which was lower than that of X17, concentrating the stress peaks at fracture initiation on an even smaller volume, forcing the material to fracture at the pre-crack tip line.

Furthermore, in trying to indicate the fracture mechanisms present, it can be seen in the zoomed area of specimen X7 that one of the main failure mechanism is fiber-matrix interface failure (i.e., debonding). This, since a lot of relatively clean fibers are present, indicating clean separation. However, this might also be due to a bad matrix penetration. Next to this, ductile yielded matrix material is present, indicating matrix-failure. Finally, a little amount of fiber fracture is observed but some is present.

When taking a look at the zoomed area of specimen X19, the non pre-cracked specimen, lots of fractured fibers can be seen over the entire width of the specimen. Whether this is due to testing itself or due to the machining of the specimen is unknown. If the latter case is true, then the reason for this failure not being present in specimens X7 and X17 is the fact that these failed fibers would have been cut away during the pre-cracking of the specimen.

As can be seen in **Figure 3.15**, specimen X8 up until specimen X18 have the seemingly lowest average G_{Ic} and are cut at a depth of 0.1 mm. The K_{Ic} does not seem to differ much, which is likely due to the local micro-structure of the volume around the plastic zone which is all determining in fracture initiation and more available testing data is necessary to indicate this trend. Furthermore, the blades used for the cutting of these specimens, show little sign of wear compared to the blades used for cutting 800µm and microscopic examination showed the NTD to be the smallest, indicating the sharpest pre-crack possible. Finally the SEM analysis indicated that, the crack tip line for 100µm pre-crack depth was more even than the crack tip line for 800µm. For these reasons, it has been chosen to cut the specimens

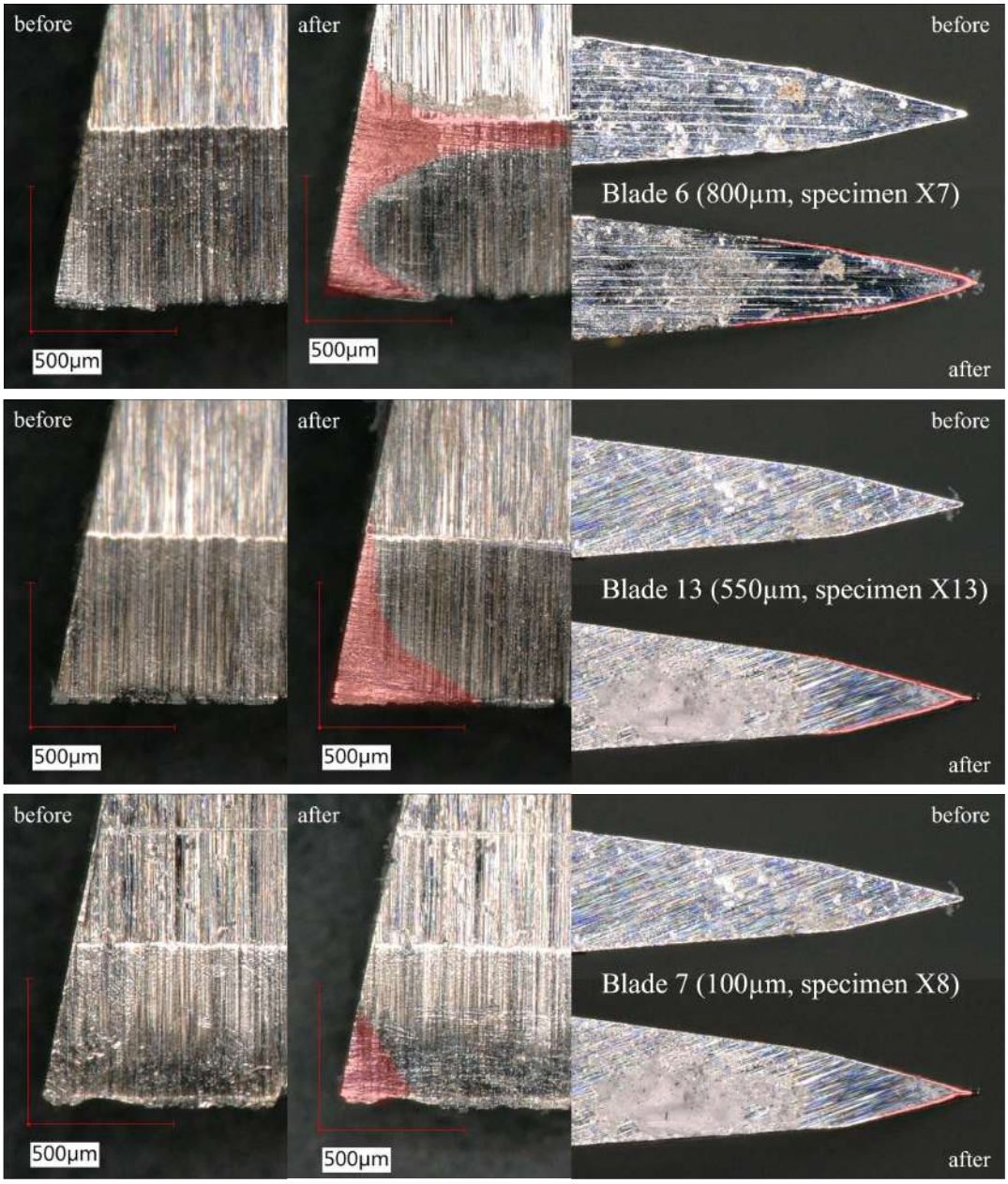

Figure 3.16: Blade 6, 13 and 7 before and after pre-crack cutting, from top to bottom respectively (the damaged area is shaded translucent red)

for the RR at a depth of 100µm.

3.5.2 Analysis of force-displacement plots

The calculation of K_{Ic} and G_{Ic} makes use of the force-displacement plot. Similarly, the R-curve is calculated by using the same force-displacement plot. An example of this plot of specimen X15 can be seen in **Figure 3.18** on the left. This plot is created by first zeroing the displacement offset of the specimen and afterwards correcting for the setup compliance C_0 as prescribed in the ISO 13586 standard. This is done by obtaining the setup compliance C_0 and subtracting the product of compliance C_0 times force at displacement from the measured displacement during testing.

It can be seen that the initial loading up until $\sim$ 185N is quasi-linear, indicating linear elastic material

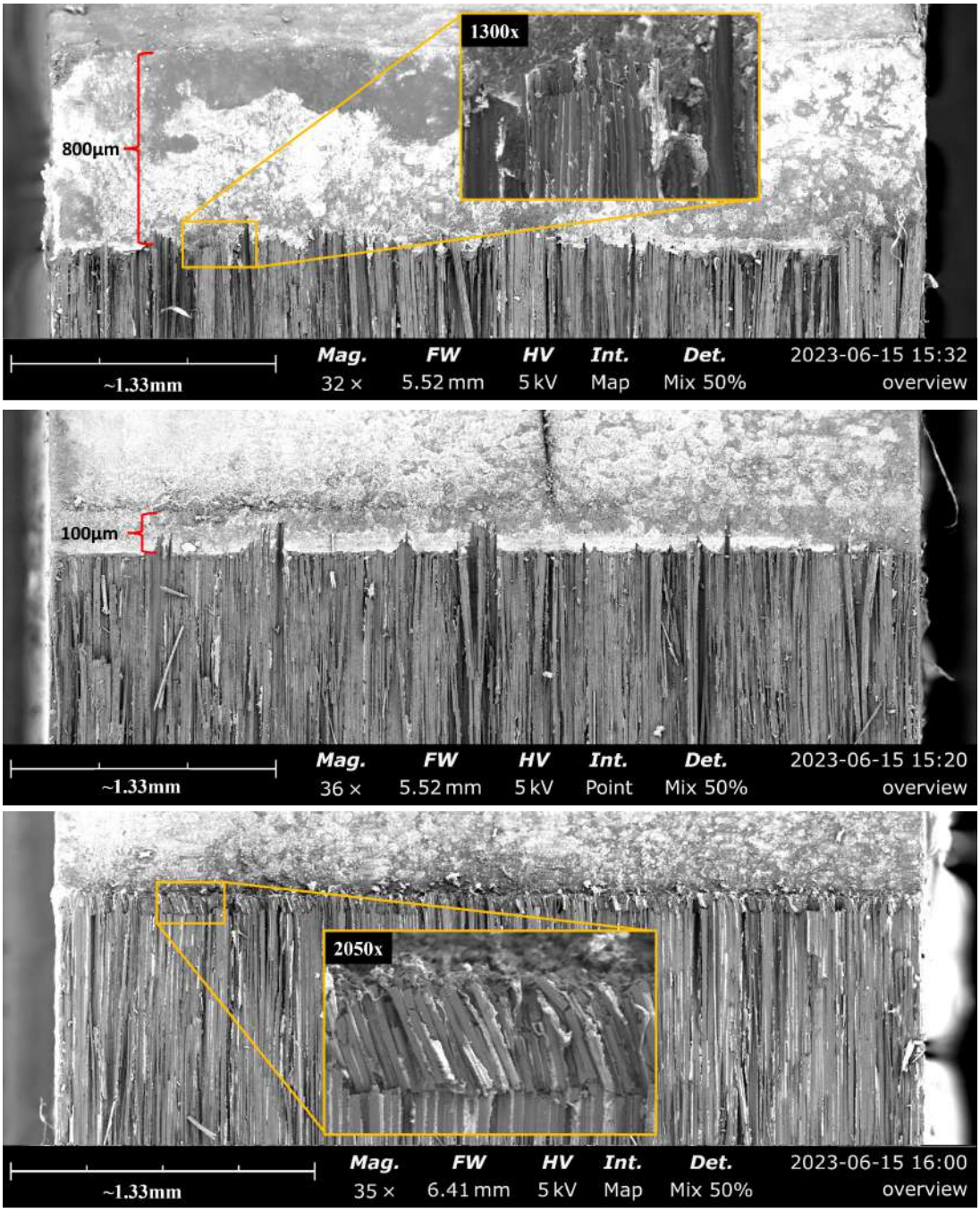

Figure 3.17: SEM images of specimen X7, X17 and X19 after pre-crack cutting and testing, from top to bottom respectively

behaviour. At larger displacements, the fracture initiates and the crack starts to propagate. When testing plastics, the usual result is a spontaneous crack through the specimen, indicating brittle failure. This is indicated by an almost vertical line in the force-displacement plot after fracture initiation. However, when testing the Mode I longitudinal intralaminar crack propagation, no sudden brittle fracture is observed but instead a slowly, in speed decreasing, crack propagation is observed. This progression seems very consistent and smooth. Whether this is the case, can be determined by the R-curve as will be explained in **Section 3.6**.

Furthermore, the specimen is loaded with a constant displacement up until the end of crack propagation where the displacement is reversed until the specimen is fully unloaded. This is indicted by the

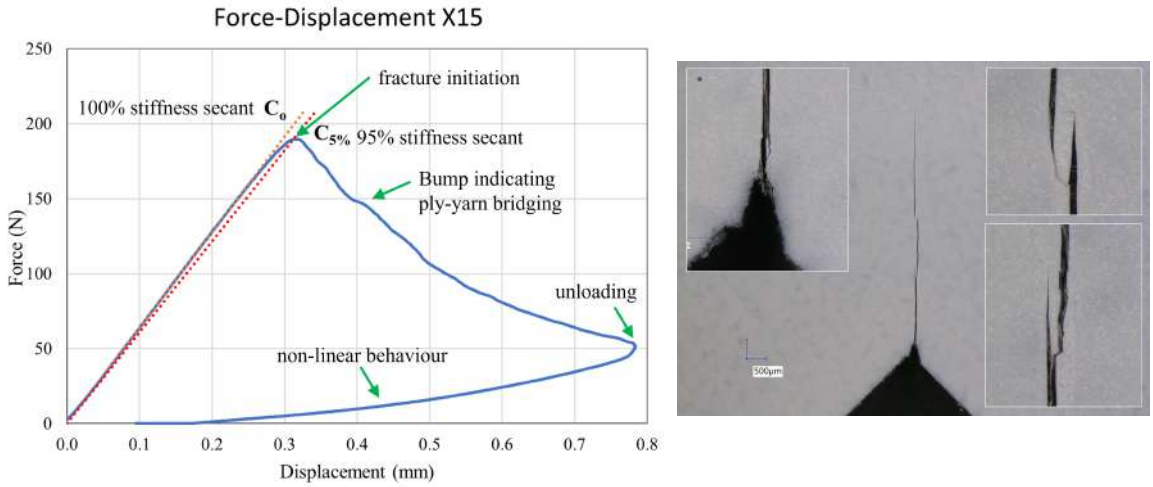

Figure 3.18: Left: Force-Displacement plot of specimen X15, Right: example of ply/yarn bridging

bottom line in **Figure 3.18**. In the case of linear elastic material behaviour, this line would be linear. However, as can be observed, this is not the case which indicated non-linear behaviour. This can be due to toughening mechanisms with subsequent excessive plasticity in the ligament, and or ply/yarn shifting interfering with the unloading, resulting in the inability to return to origin.

What can be seen as well is that the crack propagation largely resembles a $\frac{1}{x}$ function. Sometimes 'bumps' on the $\frac{1}{x}$ line are present. An example of such a bump is present in **Figure 3.18** on the left. These bumps occurred at the same time where a phenomenon of bridging fibers/plies has been observed. The crack 'jumps' a ply or fiber bundle since that is the apparent way of least propagation resistance, slightly decreasing the consistent and smooth crack propagation. This jumping of fiber bundle or ply can be seen in **Figure 3.18** on the right where a total crack is presented and the sides of the figure show the zoomed in jumping.

Lastly, the ISO 13586 standard states to check $F_{max}/F_5 < 1.1$. This is to ensure linear elasticity in loading the specimen. If $F_{max}/F_5 > 1.1$, the specimen should be discarded and a new one should be tested in its place. Since LEFM will be assumed for the adapted method for CFRPs, this will be adhered to. Furthermore, the standard states to check that the difference between E_{stiff} and E_{fract} is less than 15% as described in **Section 2.1**. However, the notion of a single Young's modulus in all directions for an anisotropic CFRP is not true. Although, the test is characterized by Mode I loading, where the Young's modulus of the matrix material LMPAEK is dominant. Due to differences in the local micro-structure, the modulus in this direction might differ from the Young's modulus of LMPAEK. Therefore, this check shall not determine the validity of the test. It can, however, be checked.

3.6 The R-curve

As explained in **Section 2.2**, the R-curve is a representation of the material's resistance to crack propagation. It was mentioned in **Chapter 1** that the ISO 13586 standard does not provide any method to calculate the R-curve of a SENB specimen. This, since fracture in polymer SENB specimens is brittle and spontaneous and an R-curve is not at issue.

However, it was observed that the intralaminar crack propagation of a UD composite SENB specimen might exhibit stable crack propagation, much like a DCB specimen used for the testing of interlaminar fracture toughness.

3.6.1 R-curve determination by direct observation of the load, displacement and crack length

The ISO 13586 standard defines G_{Ic} by **Equation (2.6)**. Here, the energy to break, denoted by W_b, is equal to the area under the force-displacement curve up until point of crack initiation. This makes sense for the fact that when a polymer specimen fractures in a quick and brittle way, all the accumulated work done by the loading rig will transform into fracture and no residual energy is left. When $P(x)$ is the load at displacement x, d is the displacement at crack initiation and d_0 is the displacement prior to loading, equal to 0, then **Equation (3.1)** applies.

$$W_b = \int_{d_0}^{d} P(x)\,dx \tag{3.1}$$

However, an important realization to make is the fact that during crack propagation of a UD composite SENB specimen, the fracture is not sudden and seems to propagate in a stable way. For the calculation of the G_{Ic} during crack propagation, **Equation (2.6)** cannot be used. The formula makes use of the factor $\phi(a/w)$ which is added to account for the crack length dependent stiffness of the specimen and accounts for load-line compliance. A. Bakker has computed the parameters for this $\phi(a/w)$ function, based on linear stiffness and with brittle, spontaneous fracture of a polymer SENB specimen in mind [60]. When trying to compute the G_{Ic}, the values seemed to display a relation closer to a power function with ever increasing values, than a slightly rising, approximately linear, R-curve. Another reason why **Equation (2.6)** cannot be used has to do with the energy balance. When recalling the energy balance as explained in **Equation (2.1)**, it follows that during crack propagation, not all energy dissipates at once at fracture initiation as is assumed in **Equation (2.6)**.

A different method had to be found to calculate the G_{Ic} values during crack propagation and the attention was directed at the ISO 15024 standard for the determination of Mode I fracture toughness and crack propagation resistance of DCB specimens. Similar to this standard, it was tried using the discrete area method where G_{Ic} is determined by calculating the change of work done ΔW_b over a small displacement δx and divided by the change in fractured area, being the specimen width b times the increment of crack length over that displacement δa. This relation is given by **Equation (3.2)**. It can be proven mathematically that every change in work done, independent of the function direction, can be approximated by this equation [43].

$$\Delta W_b = \frac{1}{\delta a}\{P(x)\cdot(x+\delta x) - P(x+\delta x)\cdot(x)\} \tag{3.2}$$

Unfortunately, this approach is difficult because it requires subtraction of nearly equal values. This method might be suitable for the calculation of G_{Ic} in DCB specimens with significantly large crack length increments, but with intralaminar cracks, the method becomes increasingly difficult. The increase in area is usually small and difficult to measure accurately. Together with the fact that this value is used in the denominator of the equation, the results become unreliable due to a huge amount of scatter in the crack growth data. It has been tried to reduce the data using exponential smoothing, several regression methods and, sliding windows but the problem remained persistent.

A solution, that does not require subtraction of practically equal areas proved to be part of a revised area method [61]. The representation of this revised area method is presented in **Figure 3.19b**. First, **Figure 3.19a** presents the energies in intralaminar SENB testing. This graph is devised from a specimen that was tested in the Round-Robin. The area under the orange line in this figure represents the cumulative energy U_1 and is equal to the total work done by the loading rig given by **Equation (3.3)**.

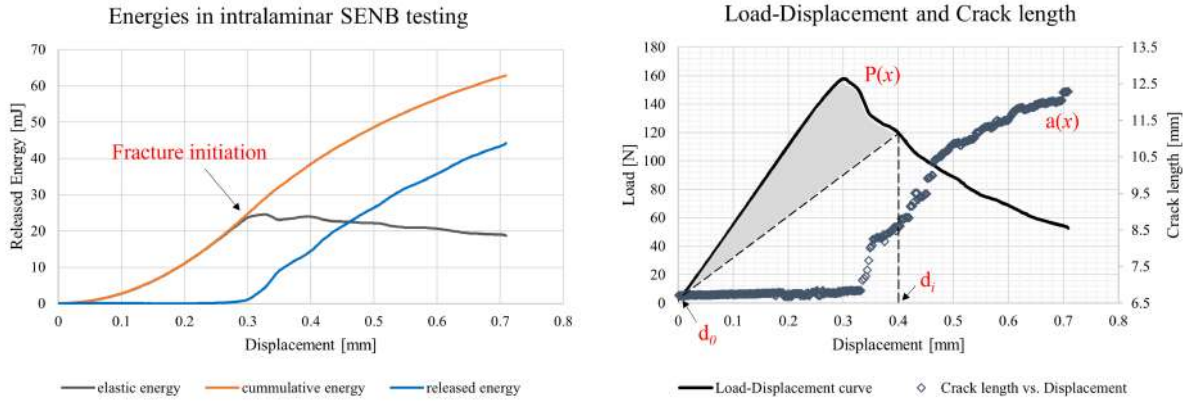

(a) Different Energies present in intralaminar SENB testing. Notice that released energy U_2 is >0 when crack propagation starts

(b) Force-Displacement plot with crack length on secondary y-axis. The grey area denotes the released energy U up to displacement d_i

Figure 3.19: Energies in intralaminar SENB testing and Load-Displacement plot

$$U_1(d_i) = \int_{d_0}^{d_i} P(x)\,dx \approx \sum_{i=0}^{d_i-1} \left\{ (d_{i+1} - d_i) \left\{ P(d_i) + \frac{P(d_{i+1}) - P(d_i)}{2} \right\} \right\} \tag{3.3}$$

Then, the area under the grey line represents the elastic energy in the specimen (i.e., the energy stored in elastic deformation) at displacement d_i. **Equation (3.4)** yields the elastic energy U_3 at each displacement d_i. The important assumption is made that, if the specimen would be unloaded during crack propagation, the stored elastic energy would dissipate and the load-line would return to the origin, exhibiting linear elasticity. This can be verified in practice, but if one tried to measure the return line by unloading during testing, the ply/yarn-bridging zone would interfere with the unloading and not return to the origin (i.e., the fibers would not slide back into their original location and would likely be crushed instead). But any energy associated with such crack plane interference or non-linearity during unloading is not part of the energy released during monotonic crack propagation and therefore should not be part of the calculated cumulative released energy U_2 as will be explained in **Section 3.6.3**.

$$U_3(d_i) = \frac{P(d_i)}{2}(d_i - d_0) \tag{3.4}$$

Finally, the cumulative released energy U_2 at displacement d_i by fracture of the material and subsequent crack propagation is equal to area under the blue line and given by **Equation (3.5)**. Notice that the area is the same as the area under the cumulative energy curve minus the area under the elastic energy curve.

$$U_2(d_i) = U_1(d_i) - U_3(d_i) \approx \sum_{i=0}^{d_i-1} \left\{ (d_{i+1} - d_i) \left\{ P(d_i) + \frac{P(d_{i+1}) - P(d_i)}{2} \right\} \right\} - \frac{P(d_i)}{2}(d_i - d_0) \tag{3.5}$$

The cumulative released energy between d_o and d_i is presented in **Figure 3.19b** by the shaded area. The area of elastic energy within the same boundaries is presented by the area bound by the x-axis and the 2 dotted lines. Furthermore, the crack propagation is presented by blue diamonds with values on the second y-axis.

To obtain the R-curve, the next step is to plot the cumulative released energy $U_2(d_i)$ against crack length $a(d_i)$ to obtain $U_2(a)$. Since both displacement and crack length are recorded at the same time and synced in LabVIEW, this is easily done. The result is presented in **Figure 3.20**. Then, the R-curve is obtained by **Equation (3.6)**. As seen, the slope $\frac{dU_2(a)}{da}$ of the cumulative released energy $U_2(a)$ at each CTP a divided by the specimen width B yields the crack propagation resistance $R(a)$ in $[\frac{J}{m^2}]$.

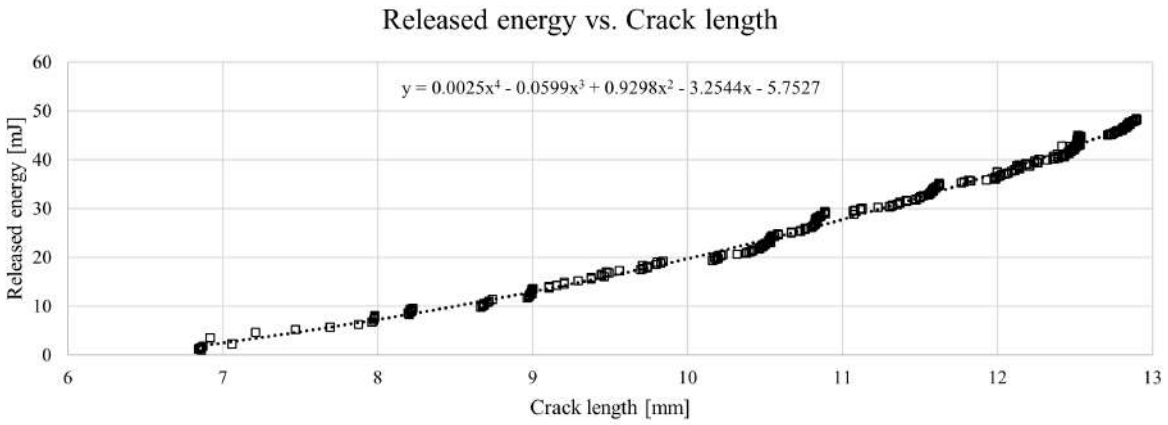

Figure 3.20: The cumulative released energy U plotted over the crack length a

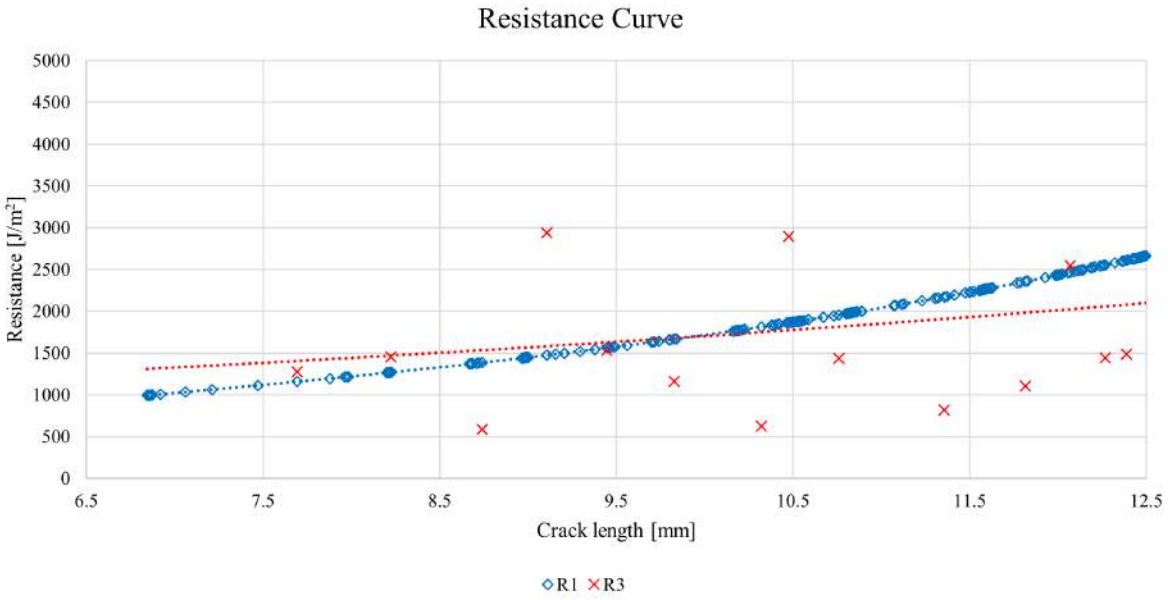

Figure 3.21: Red: R-curve with sliding window linear fits, Blue: R-curve with exact derivative of polynomial fit

$$R(a) = \frac{1}{B}\frac{dU_2(a)}{da} = \frac{1}{B}U_2'(a) \tag{3.6}$$

The challenge now lies in finding the slope $\frac{dU_2(a)}{da}$ by numerically finding the derivative of $U_2(x)$ with scattered data. Several methods were used such as fitting polynomials, linear and cubic regression, exponential smoothing, but the data seemed to contain huge scatter. The exact integration of the polynomial fit, displayed in **Figure 3.20**, to the $U_2(x)$ data, proved to provide a somewhat manageable curve

that is displayed in **Figure 3.21** by data set $R1$. Another manageable result was found by using linear fits to a sliding window of 15 data points along the data. The R value for the crack length at the center of each window is found from the slope of that window's fit. The R-value is calculated by **Equation (3.6)**. This method is presented by data set $R3$ in **Figure 3.21**.

What can be seen is that, when fitting relations to both datasets, the slope differs somewhat and the vertical position ('amplitude') differs at begin and end of the R-curve. There seems to be agreement at a crack length a of 10mm. The reason for the observed difference is that the change in crack length Δa, being in the denominator of **Equation (3.6)**, contains data scatter where a small change in Δa influences the result for R a lot, explaining the exaggerated data points of $R3$ and exaggerated movement of the $R1$. This agrees to the statement by John A. Nairn: "Unfortunately this approach (referring to the discrete area method and necessary division by Δa) is difficult because it requires subtraction of nearly equal values of Δa [61].

3.6.2 R-curve determination by Corrected Beam Theory (CBT)

The relation between the displacement, load and crack length has been observed by testing of specimens whereafter the slope of $\frac{dU_2}{da}$ has been tried to obtain, by sliding windows and fitting polynomials. However, the crack length a data scatter proved to provide some challenges. This section will elaborate on finding an exact relation for the change of compliance over crack length $\frac{dC}{da}$. This relation can be found analytically, by applying Castigliano's method for determining the displacements of a linear-elastic system based on the partial derivatives of the energy [62].

Let us split the a SENB specimen into 4 sections as depicted in **Figure 3.22**. Here, the beam is split into sections AC, CD, DE and EB. Sections, CD and DE represent the area where the crack propagates and are relatively small compared to sections AC and EB. Furthermore, these sections have a different cross-section, and corresponding second moment of area I_i dependant on crack length a. The vertical deflection of position D by force P can be determined by Castigliano's theorem in **Equation (3.7)**, which states that the deflection over length 0 to L can be approximated by the integral of the bending moment $\frac{M}{EI}$ times the partial derivative of the moment M over the force P [62]. Here P is the load on the SENB specimen, E_y the material's Young's modulus, I the second moment of area and M the resultant moment over length 0 to L.

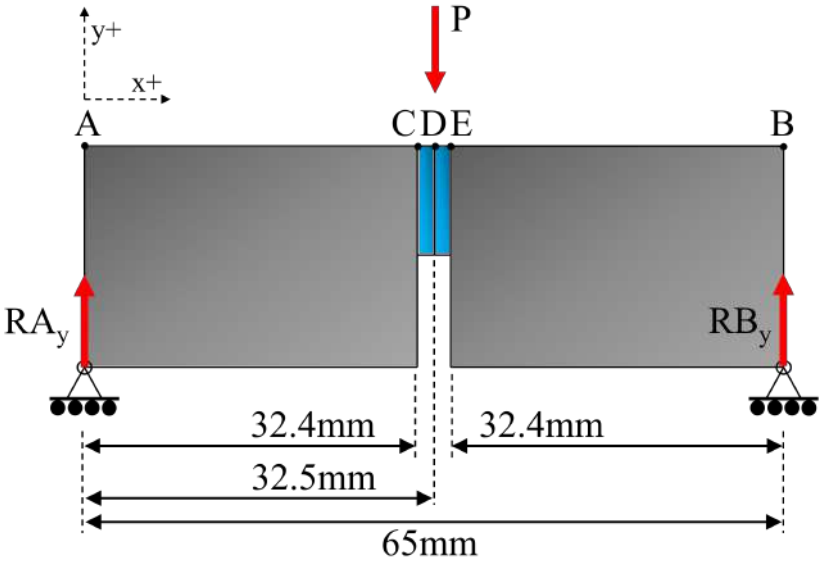

Figure 3.22: Free body diagram of a SENB specimen

$$\delta_{0-L} = \int_0^L \frac{M}{E_y I} \left\{ \frac{\partial M}{\partial P} \right\} dx \tag{3.7}$$

For the deflection of point D, we can write Castigliano's theorem for each section i and sum the deflection as presented in **Equation (3.8)**

$$\delta_{x_1-x_4} = \sum_{i=1}^{4} \int_{x_i}^{x_i+1} \frac{M_i}{E_y I_i} \left\{ \frac{\partial M_i}{\partial P} \right\} dx \tag{3.8}$$

After splitting the SENB specimen in 4 sections, divided by positions A, B, C, D, and E and equating the moment balance around each section, the results are presented in **Table 3.7**.

Table 3.7: Sections, limits, moment balances, second moment of area's and partial derivatives

Segment	**x=0**	**Limits [mm]**	I_i	M_i	$\frac{\partial M_i}{\partial P}$
AC (1)	A	0-C	I_1	$\frac{P}{2}x$	$\frac{x}{2}$
CD (2)	A	C-D	I_2	$\frac{P}{2}x$	$\frac{x}{2}$
DE (3)	A	D-E	I_2	$\frac{P}{2}x - P(x-D)$	$\frac{x}{2} - x + D$
EB (4)	A	E-B	I_1	$\frac{P}{2}x - P(x-D)$	$\frac{x}{2} - x + D$

Substitution in Castigliano's theorem yields **Equations (3.9)** to **(3.12)**.

$$\delta_{AC} = \frac{1}{E_y I_{AC}} \int_A^C \left\{ \frac{P}{2}x \right\} \left\{ \frac{x}{2} \right\} dx = \frac{1}{E_y I_{AC}} \left[\frac{P}{12}x^3 \right]_A^C = \frac{1}{E_y I_{AC}} \left\{ \frac{P}{12}C^3 \right\} \tag{3.9}$$

$$\delta_{CD} = \frac{1}{E_y I_{CD}} \int_C^D \left\{ \frac{P}{2}x \right\} \left\{ \frac{x}{2} \right\} dx = \frac{1}{E_y I_{CD}} \left[\frac{P}{12}x^3 \right]_C^D = \frac{1}{E_y I_{CD}} \left\{ \frac{P}{12}D^3 - \frac{P}{12}C^3 \right\} \tag{3.10}$$

$$\delta_{DE} = \frac{1}{E_y I_{DE}} \int_D^E \left\{ \frac{P}{4}x^2 - \frac{DP}{2}x + D^2 P \right\} dx = \frac{1}{E_y I_{DE}} \left[\left\{ -\frac{P}{12}x^3 + PD^2 x \right\} \right]_D^E = \frac{1}{E_y I_{DE}} \left\{ -\frac{p(E^3 - D^3)}{12} + PD^2 E - PD^3 \right\} \tag{3.11}$$

$$\delta_{EB} = \frac{1}{E_y I_{EB}} \int_E^B \left\{ \frac{P}{4}x^2 - \frac{DP}{2}x + D^2 P \right\} dx = \frac{1}{E_y I_{EB}} \left[\left\{ -\frac{P}{12}x^3 + PD^2 x \right\} \right]_E^B = \frac{1}{E_y I_{EB}} \left\{ -\frac{p(B^3 - E^3)}{12} + PD^2 B - PD^2 E \right\} \tag{3.12}$$

Summing all deflections and realizing $I_{AC} = I_{EB} = I_1$ and $I_{CD} = I_{DE} = I_2$ yields **Equation (3.13)**.

$$\delta_D = \sum_{i=1}^{4} \int_{x_i}^{x_i+1} \frac{M_i}{E_y I_i} \left\{ \frac{\partial M_i}{\partial P} \right\} dx = \frac{1}{E_y I_{AC}} \left\{ \frac{P}{12} C^3 \right\} + \frac{1}{E_y I_{CD}} \left\{ \frac{P}{12} D^3 - \frac{P}{12} C^3 \right\} + \frac{1}{E_y I_{DE}} \left\{ -\frac{p(E^3 - D^3)}{12} + PD^2 E - PD^3 \right\} + \frac{1}{E_y I_{EB}} \left\{ -\frac{p(B^3 - E^3)}{12} + PD^2 B - PD^2 E \right\} = \frac{PD^3}{12 E_y I_1} + \frac{-PB^3 - 11D^3 P + 12D^2 BP - 24D^2 PE}{12 E_y I_2} \quad \textbf{(3.13)}$$

Now we have written the deflection on point D, **Equation (3.13)** can be written as function of crack length by realizing only the second moment of area I_2 changes with changing crack length. The equation for the second moment of area at crack location is equal to **Equation (3.14)**, with B^* the width of the specimen and W the height of the specimen.

$$I_2 = \frac{B^*(W - a)^3}{12} \quad \textbf{(3.14)}$$

According to Williams, in the case of linear elasticity, the equation for energy release rate can be expressed in terms of $\frac{dC}{da}$ and U_3 (which is the stored elastic energy in the body by **Equation (2.1)**) [43]. This expression is presented in **Equation (3.15)**.

$$G(a) = \frac{P^2}{2B_{spec}} \frac{dC}{da} = \frac{1}{2B} \left\{ \frac{u}{C} \right\} \frac{dC}{da} = \frac{U_3}{B^*} \frac{1}{C} \frac{dC}{da} \quad \textbf{(3.15)}$$

After substitution of **Equation (3.13)** in **Equation (3.15)**, the compliance of a SENB specimen is given by **Equation (3.16)**.

$$C(a) = \frac{u}{P} = \frac{PD^3 I_2(a) - PB^3 I_1 - 11PD^3 I_1 + 12D^2 BI_1 - 24PD^2 EI_1}{12 E_y I_1 I_2(a) P} \quad \textbf{(3.16)}$$

After substitution of **Equation (3.14)** and taking the derivative $\frac{dC}{da}$, **Equation (3.17)** is obtained.

$$\frac{dC(a)}{da} = -3 \frac{24D^2 E + 11D^3 - 12BD^2 + B^3}{B^* E_y (a - W)^4} \quad \textbf{(3.17)}$$

Finally, after substitution of **Equation (3.17)** in **Equation (3.15)**, we obtain **Equation (3.18)** which is the energy release rate as function of crack length, based on the corrected beam theory and assuming linear elastic material behaviour.

$$R(a) = G(a) = \frac{P^2}{2B^*} \frac{dC}{da} = -\frac{3P^2 \left(24D^2 E + 11D^3 - 12BD^2 + B^3\right)}{2B^{*2} E_y (a - W)^4} \quad \textbf{(3.18)}$$

3.6.3 Comparison between both R-curve determination methods

Next, it is interesting to see whether **Equation (3.18)** can provide a good approximation for the testing data of SENB specimens. As mentioned before, **Equation (3.15)** assumes linear elastic material behaviour and calculates G by the stored elastic energy U_3. To obtain the R-curve for the SENB test data using **Equation (3.18)**, only the crack length a, force, and displacement are inputs. Although, the

Young's modulus of the material does appear in **Equation (3.18)**, it is canceled out in evaluation of G. Instead of taking the cumulative energy U_2 for the calculation of G, we now take the stored elastic energy U_3. This, since the formulation of G is based on the change of compliance over crack length $\frac{dC}{da}$.

Figure 3.23 presents the theoretically calculated R-curve, next to the same R-curves (fitting by sliding window method and a polynomial) as in **Figure 3.21**. This R-curve, based on theoretical $\frac{dC}{da}$ is shown by data set $R2$.

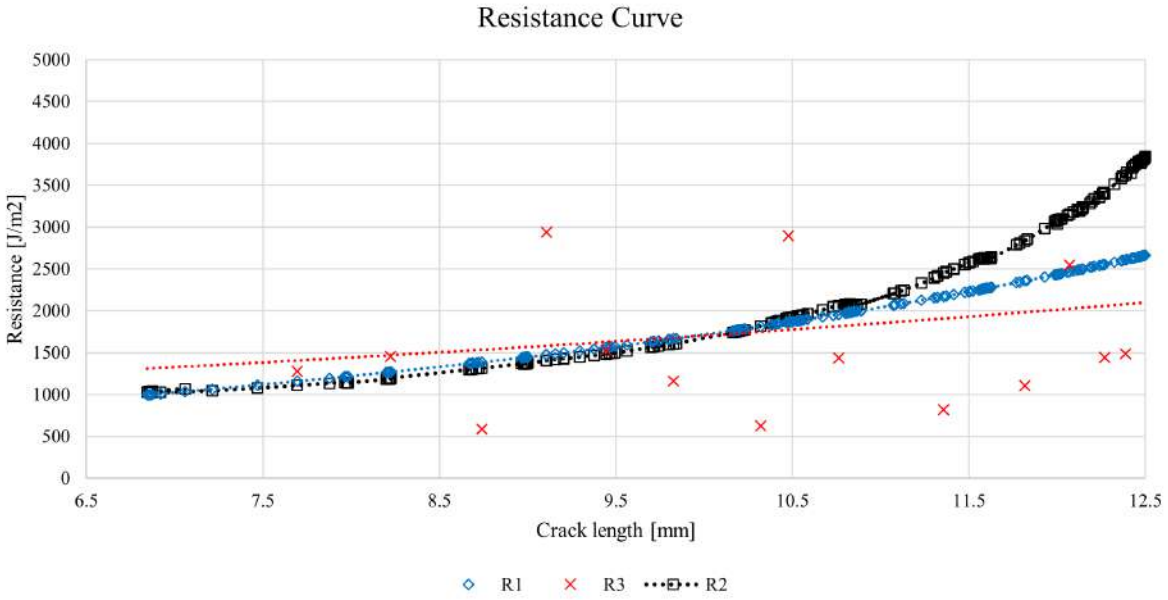

Figure 3.23: Black: R-curve with theoretical $\frac{dC}{da}$, Red: R-curve with sliding window linear fits, blue: R-curve with exact derivative of polynomial fit

The CBT method seems to approximate reality quite well up to a crack length of approximately 10.5mm for this specimen. At values of a/w close to 1, meaning the crack length is approaching the specimen height, usually toughening mechanisms and excessive plasticity occur, meaning the assumption of linear elasticity has been violated. The load-line, when unloading at these longer crack lengths, will for example not return to the origin but will cross the x-axis at a certain displacement. **Figure 3.24** shows the force-displacement plot of specimen X15 with an energy analysis at maximum crack length. Here U_2 is the cumulative released energy, U_3 is the stored elastic energy and U_p is the unrecoverable plastic deformation energy. When assuming linear elastic material behaviour, the unloading would yield the green arced area plus the red arced area, increasing U_3. However, as can be seen in the figure, the stored elastic energy U_3 is smaller in reality. As a result, the G_{Ic} will be lower in reality than assumed by the area method for these larger displacements. This explains the higher values of G_{Ic} for data set R_2 at larger crack lengths where plasticity increased. Furthermore, it should be noted that, when basing the R-curve on the released energy, this effect of plastic deformation is not visible. This is due to the fact that the yellow arced area in **Figure 3.24**, being the cumulative released energy U_2, does not overlap with the the unrecoverable plastic deformation energy U_p, being U_5.

For the construction of the entire R-curve, it should be noted that it is assumed that the SENB specimen only releases energy to crack propagation and process zone damage, this process zone damage however is not taken as part of the cumulative released area, indicating the difference between U_2 and U_5. Since there is no crack extension at initiation, the released energy at crack initiation is equal to zero, since all energy is stored in elastic deformation. When the crack starts to propagate, the release of energy starts, where G_{Ic} is equal to the slope of $\frac{dU_2}{da}$.

However, the initiation of fracture costs energy as well and is denoted by W_b as described by ISO

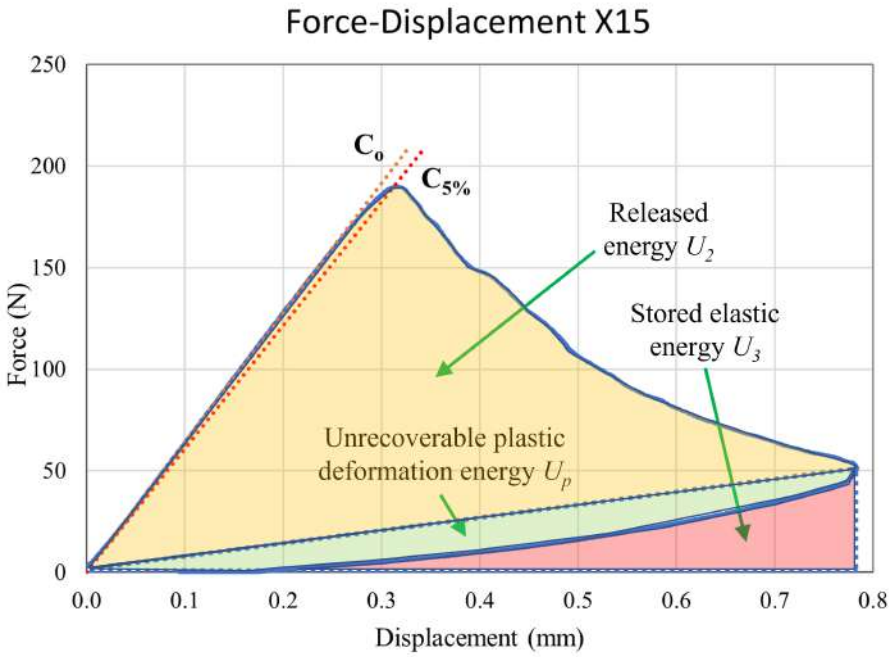

Figure 3.24: Energy analysis of specimen X15 at maximum crack length a. The yellow arced area represent the cumulative released energy U_2, the red area represents the stored elastic energy U_3 and finally the green arced area represents the unrecoverable plastic deformation energy U_p.

13586. For the testing of UD composite SENB specimens it has been decided to split the R-curve into two parts. The first part, leading up to the CTP at crack initiation a_{Ic}, will be determined by the method presented in ISO 13586, and the second part up to final CTP a_{max} will be determined by the area method presented in this section. This relation is presented by **Equation (3.19)** In determining $R(a)$ during crack propagation, **Equation (3.18)** can be used as well, although it should be noted that excessive plasticity at a/w close to 1 is neglected due to assumed linear elasticity at the same a/w ratios.

$$R(a) = \begin{cases} W_b \frac{1}{hw\phi(a/w)} & \text{for } \textit{initiation} \\ \frac{1}{B}\frac{dU_2(a)}{da} & \text{for } \textit{crack propagation} \\ \quad \textit{or} & \\ -\frac{3P^2\left(24D^2E+11D^3-12BD^2+B^3\right)}{2B^{*2}E_y(a-W)^4} & \text{for } \textit{crack propagation} \end{cases} \tag{3.19}$$

3.7 Crack tip tracking algorithm and test setup

After finishing the specimen preparation and data reduction methods, the implementation of the testing method itself became paramount. One of the parameters to ultimately be able to calculate the characterizing R-curve (as explained in **Section 3.6**), is the crack length of the specimen under loading. There is the need of constant monitoring of this value to be able to precisely determine G_Ic at different points in time. This section will elaborate on the test setup used. However, this section will not explain the algorithm used to track the crack length during propagation due to its complexity. The detailed explanation and the experimental methods used to optimize this algorithm can be found in **Appendix B**.

3.7.1 The need for crack tip tracking

The known ISO 15024 standard provides a method to calculate the G_{Ic} values during interlaminar crack propagation in a DCB specimen. When a similar method, as described in **Section 3.6.2**, will be applied to a propagating longitudinal intralaminar crack in a SENB specimen, it requires constant monitoring of the crack length during testing. This, since G_{Ic} has unit $\frac{J}{m^2}$, being the energy to fracture in joules divided by the fractured area in squared meters. The fractured area is the crack length a, measured from the bottom of the specimen to the crack tip, multiplied by the thickness h of the specimen.

3.7.2 Test setup

This section will explain the test setup itself with information on: loading, tools used, and force and displacement acquisition. The setup is presented in **Figure 3.25** where the SENB test can be seen, loaded with a pre-cracked CF/LMPAEK specimen. The bottom rollers have been placed at exactly 65mm apart, according to what was decided in **Section 3.2**. In front of the specimen a clamped knife is positioned that can slide back and forth. The pre-crack can be placed on top of the blade, such that the specimens are placed exactly in the middle of the three point bending setup. This, of course, requires a precise setup beforehand. When tracking the crack length during testing, the slider is pushed towards the camera, out of focus.

Behind the specimen, a special holder is placed to provide a back stop for the specimen, again making it possible to position a specimen exactly in in the camera's focus. Behind the rollers, a Linear Variable Differential Transformer (LVDT) has been placed. The test is performed by moving the platform at the bottom of the setup containing the 2 rollers, towards the force cell. This way, the LVDT slides inwards. The force cell itself is positioned on top of the specimen. To the force cell, the third and last roller has been attached. Finally, the lens of the camera to measure crack length can be seen on the right.

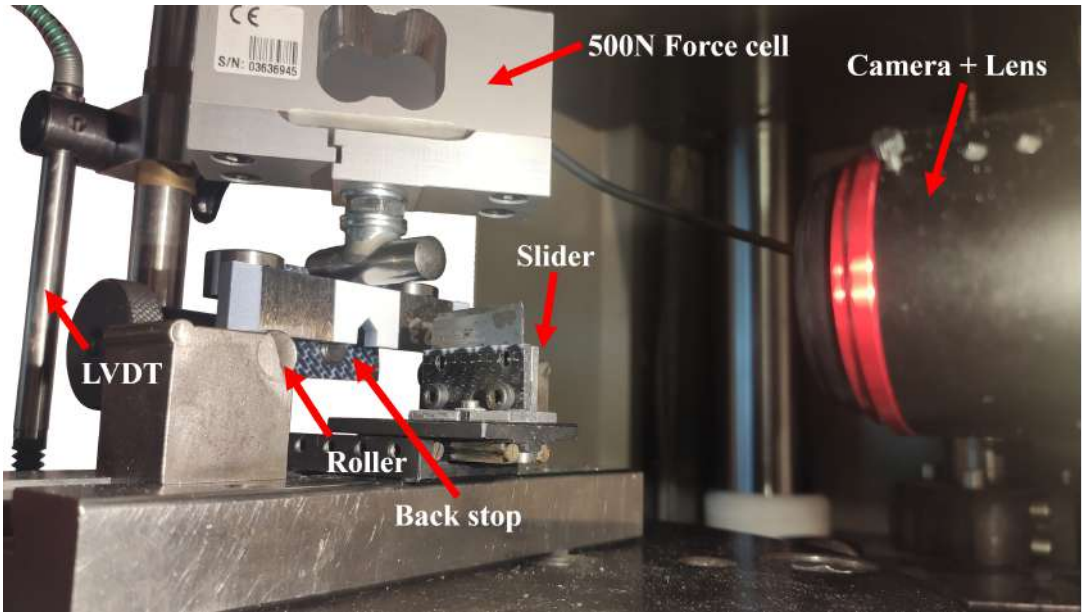

Figure 3.25: 3 point bending test setup for composite SENB specimens

The camera used is a U3-3800CP-M-GL Rev.2.2 camera from IDS, with a resolution of 5536 x 3692 Pixel (20.44 MPix) and a pixel size of 2.4µm. Its maximum frame rate is 20 fps. The camera, including lens, is placed at a distance of 105mm from the specimen, this being the same distance where the lens correction was applied as well. Furthermore, the lens used is a Kowa LM25FC24M with a focal length of 25mm, f-number of 1.8-16 and a minimum focus distance of 100mm. Finally, the sampling rate

in LabVIEW for all data has been set to 10Hz. The data sheets for the camera and lens are added in **Appendices I-1** and **I-2** respectively.

3.7.2.1 Force acquisition

Next to the crack tip position, the other important parameters to calculate the critical energy release rate G_{Ic} and fracture toughness K_{Ic} are: elapsed time, force and displacement of the specimen. The force is measured by a 500 Newton load cell. Using a 200 Newton load cell was opted out of the question with the specimen sizes chosen. This, since the maximum force reached in the preliminary tests with approximately equal material and specimen size, was approximately 185 Newton; too close to the load cell limit to be using a 200 Newton load cell. The load cell makes use of a Wheatstone bridge which is excited with an excitation voltage. The Wheatstone bridge consists of strain gauges in the Wheatstone formation. The output is then measured in $\frac{mV}{V}$. The algorithm was designed such that the load can be zeroed by applying a force offset. This eliminates the need to edit the exported data afterwards. Furthermore, a load cell needs to be calibrated after certain amount of use. After calibration, a value in $\frac{N}{\epsilon}$ can be entered in the algorithm to correct for the calibration.

3.7.2.2 Displacement acquisition

The displacement acquisition is done by using a Linear Variable Differential Transformer (LVDT) from Solartron (DP10s), having a high repeatability of 0.07µm and low hysteresis. The data sheet of this LVDT is added in **Appendix I-3**. The resolution of the LVDT used is 0.05µm and the range is 10mm. When performing a test with a speed of 0.5mm/min, this is translated to a displacement of 0.000833mm per 100ms (corresponding with a sample rate of 10Hz). The resolution of 0.05 µm is thus sufficient for the lowest occurring loading rate. Similarly to the load cell data acquisition, the displacement can be zeroed in the algorithm as well to eliminate the need to edit the data after performing the tests.

4 | Round Robin fracture toughness test results using the designed test method

After the testing of the preliminary specimens, the Round-Robin specimens have been tested according to the devised test method, setup, and with use of the LabVIEW algorithm (**Appendix B**). This section will provide the first results for the Round-Robin regarding the fracture toughness K_{Ic}, the critical energy release rate G_{Ic} and will provide the R-curves for all specimens. Furthermore, the fracture surfaces will be examined to see what failure modes and failure mechanics were present. Finally, an error analysis will be performed on the calculation of values to see what the influence of certain misreads or measurement errors are down the path of calculations.

4.1 SENB specimen division from laminate

The prepared laminate for the Round-Robin SENB tests is presented in **Appendix H-4**. The specimens were cut from the laminate in four vertical strokes. The first one was named A, the second one B and so on. Then the specimens are numbered from top to bottom, meaning specimen A23 is the 23rd specimen out of stroke A. For the organisation of the Round-Robin it has been decided to provide all participants with an equal amount of SENB specimens. It should be noted that the specimens would not be cut or pre-cracked, this is something the Round-Robin participants have to arrange themselves.

The division of the Specimens has been done as follows. Each participant has been given an equal amount of specimens out of stroke A, B, C, and D. This left each participant with 10 specimens. The amount of specimens has an influence on the precision of the results. **Equation (4.1)** presents a formula to be able to calculate the sample size needed, to be able to indicated a probability of precision [63]. Here, $n_adjusted$ is the adjusted sample size, Z^2 is the Z-score based on a standardized confidence level, p is the population proportion (assumed 50%), P the total population (92 specimens), and M the margin of error. It can be checked that a sample size of 10 will have a maximum error margin of 30% with a confidence level of 95% (Z=1.960).

$$n_{adjusted} = \frac{\frac{Z^2 p(1-p)}{M^2}}{1 + \frac{\frac{Z^2 p(1-p)}{M^2} - 1}{P}} \tag{4.1}$$

The specimens have been taken out of different strokes since a laminate can have voids or a local higher thickness, influencing the results. When one participant receives these specimens with voids and/or different thickness and tests them, the results would be off. This not necessarily due to the participant's method of testing, but due to SENB specimens itself and their original location in the laminate. However, the laminate has been checked on voids and thickness by means of a C-scan, and no large defects have been found. The scans of this laminate are presented in **Appendix H-3** The SENB specimens that were tested for this research are: A2, A13, A23, B2, B13, C2, C13, C23, D2, and D13.

4.2 Fracture toughness K_{Ic} and critical energy release rate G_{Ic}

The final values of K_{Ic} and G_{Ic} after testing of the Round-Robin specimens are presented in **Table 4.1**. beneath the table, the Relative Standard Deviation (%STD) for the data in the corresponding column is presented. The values of K_{Ic}, C and F_{max} show the lowest value, indicating the most consistent results,

followed by G_{Ic}. It is interesting to see that specimen C23, having the highest NTD of the 10 tested specimens, shows one of the lowest K_{Ic} and G_{Ic}. However, the maximum force reached during testing and the stiffness are one of the lowest present compared to the other specimens. This indicated less work U_1 needed to initiate fracture and subsequently the G_{Ic} is lower. The low K_{Ic} and G_{Ic} with a relatively high NTD can also be explained by the fact that the micro structure around the crack tip was such that initiation of fracture was relatively easy, however, this is anybody's guess.

Table 4.1: UTwente Round-Robin results, values range from green to red, being best to worst

Specimen	Rate	Cut depth	F_{max} [N]	NTD [µm]	G_{Ic} $\left[\frac{J}{m^2}\right]$	K_{Ic} $[MPa\sqrt{m}]$	$\overline{r}$ [mm]	C $\left[\frac{N}{mm}\right]$
1 (A2)	1 mm/min	0.100 mm	158	7	1583	3.03	1.25	551
2 (A13)	1 mm/min	0.100 mm	146	9	1411	2.80	1.12	548
3 (A23)	1 mm/min	0.100 mm	153	7	1503	2.98	1.18	537
4 (B2)	1 mm/min	0.100 mm	156	9	1594	3.02	1.28	553
5 (B13)	1 mm/min	0.100 mm	142	6	1360	2.75	1.08	545
6 (C2)	1 mm/min	0.100 mm	160	10	1560	3.09	1.28	566
7 (C13)	1 mm/min	0.100 mm	139	8	1223	2.66	0.96	545
8 (C23)	1 mm/min	0.100 mm	138	13	1290	2.69	0.99	523
9 (D2)	1 mm/min	0.100 mm	156	8	1566	3.02	1.25	550
10 (D13)	1 mm/min	0.100 mm	136	10	1270	2.63	0.96	523
		σ	9.10	1.97	143.00	0.18	0.13	13.43
		Average	148.36	8.48	1436.16	2.87	1.13	544.15
		%STD	**6.13%**	**23.27%**	**9.96%**	**6.19%**	**11.65%**	**2.47%**

These results of K_{Ic} and G_{Ic} and NTD are presented in **Figure 4.1** as well.

4.3 Force-displacement plots

Figure 4.2 shows the force-displacement plots of all Round-Robin test specimens. What can be seen is that all specimens show very even results over the linear loading line up to fracture, indicating a similar stiffness. However, the point of fracture initiation of the SENB specimens does differ a bit. The lowest maximum force reached is 136N for specimen D13, while the maximum maximum forced reached is 160N for specimen C2. This difference has everything to do with the local micro structure of the material around the crack tip line.

Furthermore, the crack propagation seems to proceed relatively the same for all specimens. The shape of the crack propagation part in the force-displacement plots seems similar for all specimens tested, however, the vertical position differs due to a different point of fracture invitation. Then, the unloading of the specimen was performed when the force reached a value of approximately 40N. What can be seen in the plots is that the unloading is non linear and does not return to origin. As explained in **Section 3.5.2** this can be due to toughening mechanisms with subsequent excessive plasticity in the ligament, and or ply/yarn shifting interfering with the unloading, resulting in the inability to return to origin. When taking specimens out of the SENB setup, the cracks did not fully close, indicating that one or both of these phenomena had occurred. Lastly, it can be seen that the 'leftover' displacement, being the displacement where the unloading crossed the x-axis, ranges from approximately 0.1mm to 0.25mm.

4.3.1 R-Curves

The R-curves for the RR specimens have been determined by the two methods (**Sections 3.6.1** and **3.6.2** that are presented in this research:

1. First, with use of the cumulative area method, the released energy U_2 was calculated and cross plotted against the crack length a. Then, a best fitting polynomial was fitted and the exact derivative

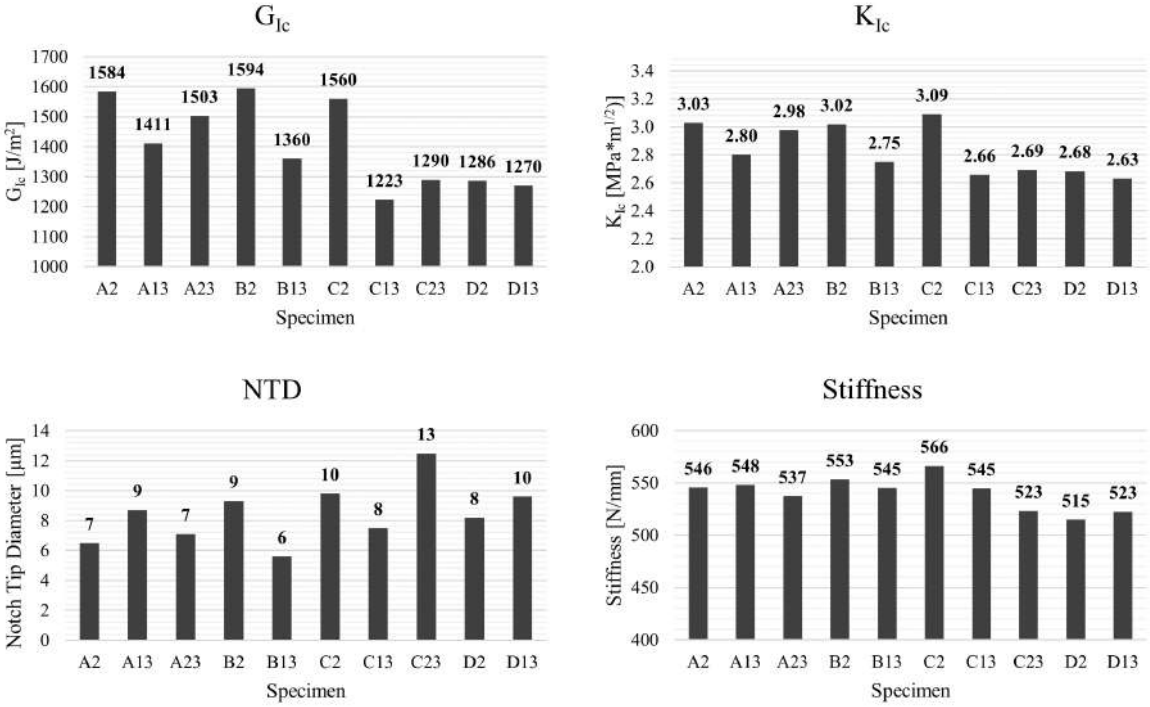

Figure 4.1: G_{Ic} [J/m^2], K_{Ic} [MPa$\sqrt{m}$], NTD [µm], and C [N/mm] Round-Robin results

$\frac{dU_2(a)}{da}$ has been determined. Finally, the R-curve has plotted by evaluating the function $\frac{dU_2(a)}{da}$ at each crack length a.

2. Second, by calculating the SENB specimen's changing compliance C as function of changing crack length a. Using Castigliano's theorem, $C(a)$ has been determined. Next, the exact derivative $\frac{dC(a)}{da}$ has been taken, whereafter it was substituted in **Equation (3.18)**, obtaining $G(a)$. Finally, the R-curve has been plotted by assuming linear elastic material behaviour in the entire crack length regime and with use of the stored elastic energy U_3 at each crack length a.

The R-curves, determined by method 1, are presented in **Figure 4.3**. Furthermore, the R-curves, determined by method 2, are presented in **Figure 4.4**.

What can be seen is that the onset and offset of the R-curves in **Figure 4.3** seems to differ quite a bit. This is likely due to the onset of the polynomial fit. Furthermore, the R-curves in **Figure 4.3** and **Figure 4.4** seem to agree quite well. However, after a certain point the influence of plasticity becomes visible. Where the R-curves in **Figure 4.3** seem to show a constant upward trend, the R-curves in **Figure 4.4** seem to increase in release rate at longer crack lengths. This is due to the assumption of linear elastic material behaviour.

to check the precision of both methods to determine the G_{Ic}, the relative standard deviation of 3 values on all curves have been checked. These values are the initiation point G_{init}, being the first G_{Ic} value, the propagation point G_{prop}, being the value of G_{Ic} at 9.5mm crack length and finally the final value G_{fin}, being the last value of G_{Ic}. The results have been displayed in **Table 4.2**. The Relative Standard Deviation (%RSD) for the initiation values are higher for the first method used. This, again due to the polynomial fit. Furthermore, the %RSD for the propagation values and initiation values using method 2 are lower than that of method 1. This means that method 2 provides results with less scatter. If this means that the results are more accurate as well is unknown. It could be the case that specimens naturally differ from one another and method 1 provides more precise results.

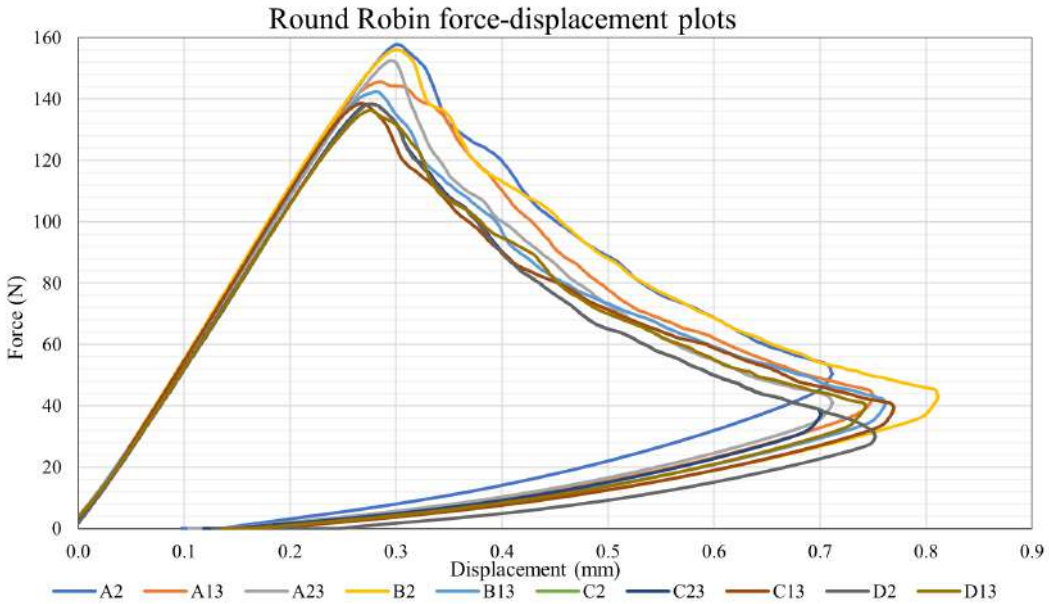

Figure 4.2: Force-Displacement plots of Round-Robin specimens

	Method 1			Method 2		
Specimen	G_{init} $\left[\frac{J}{m^2}\right]$	G_{prop} $\left[\frac{J}{m^2}\right]$	G_{fin} $\left[\frac{J}{m^2}\right]$	G_{init} $\left[\frac{J}{m^2}\right]$	G_{prop} $\left[\frac{J}{m^2}\right]$	G_{fin} $\left[\frac{J}{m^2}\right]$
A2	854	1652	2467	1029	1565	3350
A13	820	1565	2480	894	1505	4007
A23	1495	1220	2797	982	1390	3648
B2	821	1521	3030	1022	1537	4630
B13	1279	1285	2383	860	1356	3887
C2	997	1575	2860	1022	1496	4995
C13	691	1236	2652	768	1231	3506
C23	967	1117	2851	804	1295	3296
D2	690	1228	1843	816	1207	3011
D13	589	1245	3185	806	1283	4523
Average	**920**	**1364**	**2655**	**900**	**1386**	**3885**
%RSD	**30.5%**	**14.0%**	**14.4%**	**11.5%**	**9.5%**	**16.7%**

Table 4.2: Standard deviation on G_{Ic} G_{prop} and G_{fin} for determination methods 1 and 2

What can be seen as well is that method 1 has less variation in the final values of G_{Ic} than method 2 although the difference is not that significant. What is significant, is the rising of the R-curve at larger displacements. **Figure 4.5** shows the R-curves, calculated by both methods, plotted in one plot. The initial values up to 7.9mm differ due to the nature of the polynomial fit or the nature of fracture initiation. Then, both methods agree up to a crack length a of 10.4mm. Afterwards, the neglected effect of excessive plasticity causes the R-curves, calculated by method 2, to rise.

Furthermore, it is interesting that the transition between agreement and deviation of the two calculation methods seems to take place at approximately the same crack length for each specimen. When recalling the size criteria from **Section 3.2.1**, especially the criterion: $W - a > 2.5\overline{r}$ comes to mind. The reason for this particular criteria was to avoid excessive plasticity in the ligament $W - a$. **Table 4.3** shows the calculated characteristic length $\overline{r}$ and the crack length where transition between agreement and deviation of the two calculation methods took place a_{dev} for each specimen. Furthermore a_{crit} is the crack length where $W - a_{crit} = 2.5\overline{r}$. Finally, a_{dev} and a_{crit} are shown in **Figure 4.6** as well.

What can be seen is that the point of transition between agreement and deviation of the 2 calculation

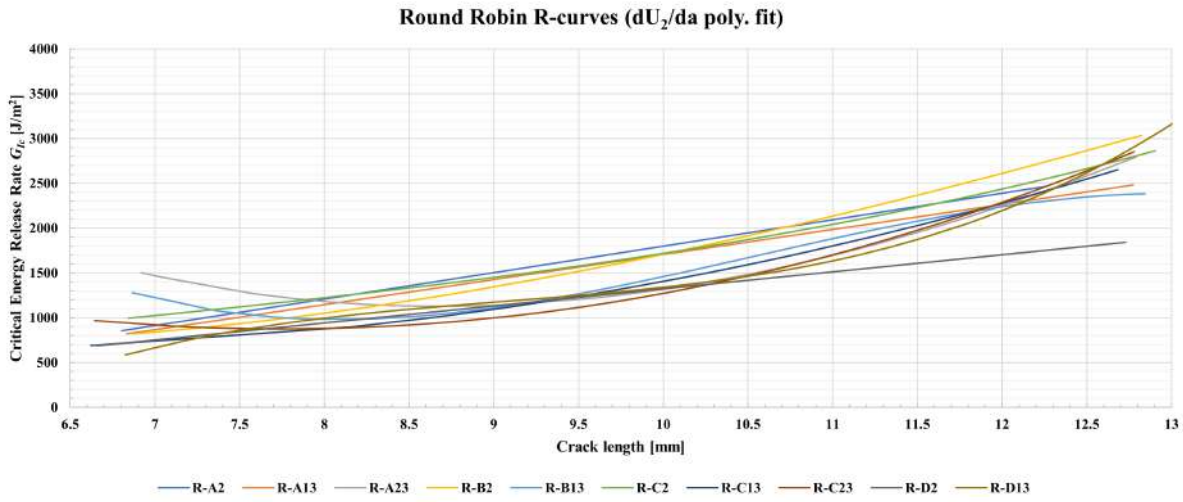

Figure 4.3: R-curves of Round-Robin specimens, calculated using method 1.

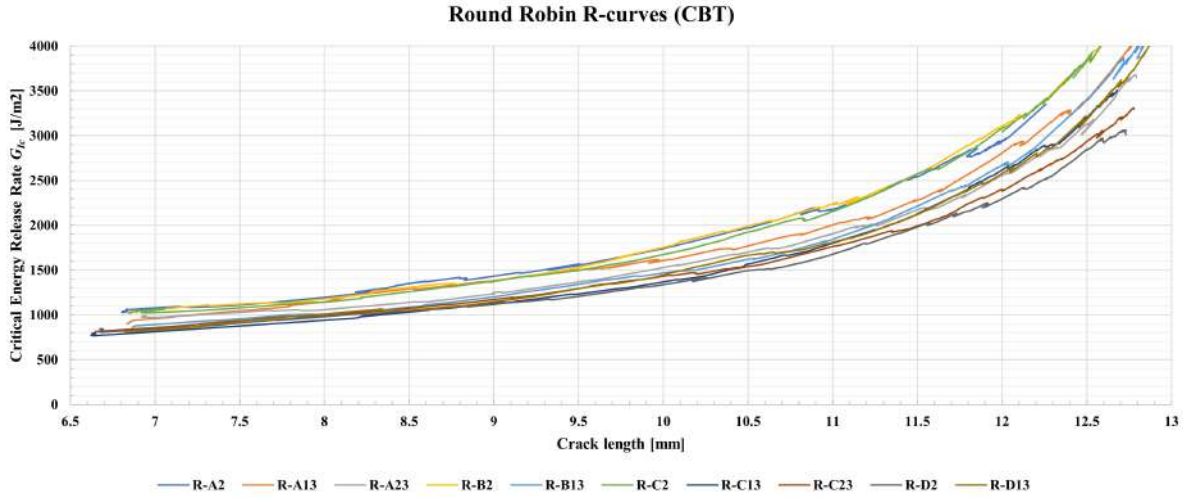

Figure 4.4: R-curves of Round-Robin specimens, calculated using method 2.

methods seems to approximate $W - 2.5\overline{r}$. The average crack length a_{dev} where the 2 methods started to deviate seems to be at 79% of W, whereas, the critical crack length determined by $W - 2.5\overline{r}$ seems to be at 80% of W. This indicates the accuracy of $\overline{r}$ and the importance. The concluding remark here is that the SENB specimens can be tested up to a crack length of maximum $0.8W$ without taking into account excessive plasticity in the ligament with. This also indicates that the assumption of linear elastic material behaviour is accurate for a maximum crack length of approximately $0.8W$.

4.4 Cumulative error analysis

To determine the cumulative cumulative error on the required results, the measurement precision of all the parameters used in calculation of G_{Ic}, K_{Ic}, stiffness S, notch tip diameter and $\overline{r}$ has been determined. These values can be found in **Appendix G-1**.

Next, a sample calculation has been done on Specimen A2 at crack initiation. Here, all the important parameters have been calculated down the path of calculation. This, including parameter precisions represented by a minimum and maximum value for each parameter. Furthermore, the same has been done

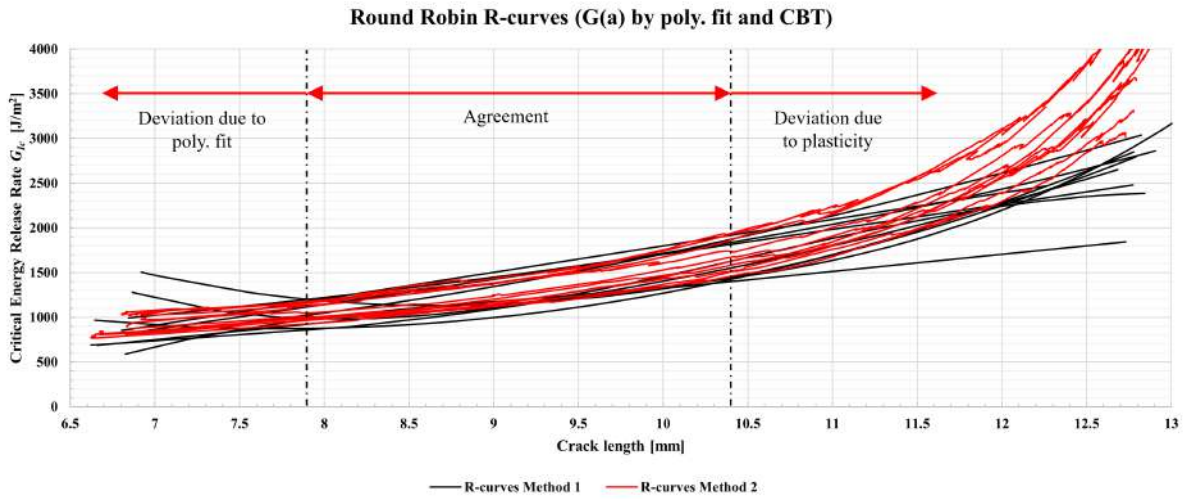

Figure 4.5: Agreement and deviation between method 1 and 2 in determining G_{Ic} at crack length a

Table 4.3: Comparison of a_{crit} and a_{dev} with averages

Specimen	$\overline{r}$ [mm]	W [mm]	$2.5\overline{r}$ [mm]	a_{dev}	W-a_{dev}	$W - 2.5\overline{r} = a_{crit}$	%W (a_{dev}/W)	%W (a_{crit}/W)
A2	1.2	14.0	3.1	10.5	3.5	10.9	75%	78%
A13	1.1	14.1	2.8	11.0	3.1	11.3	78%	80%
A23	1.2	14.1	3.0	11.6	2.5	11.1	82%	79%
B2	1.3	14.1	3.2	11.1	3.0	10.9	79%	77%
B13	1.1	14.1	2.7	11.3	2.8	11.4	80%	81%
C2	1.3	14.0	3.2	10.8	3.3	10.9	77%	77%
C13	1.0	14.1	2.4	11.3	2.8	11.7	80%	83%
C23	1.0	14.1	2.5	11.6	2.5	11.6	82%	82%
D2	1.0	14.0	2.4	10.6	3.4	11.6	75%	83%
D13	1.0	14.1	2.4	11.0	3.1	11.6	78%	83%
average	**1.1**	**14.1**	**2.8**	**11.1**	**3.0**	**11.3**	**79%**	**80%**

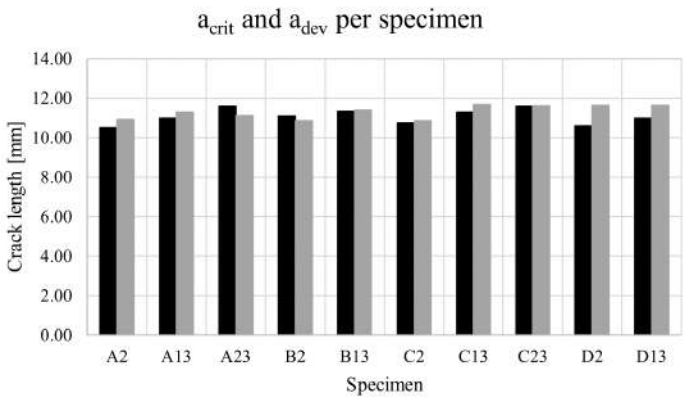

Figure 4.6: a_{crit} and a_{dev} for each specimen

for G_{Ic} at crack initiation, using both data reduction methods presented in **Section 3.6**. **Table 4.4** presents the most important values, their minimum and maximum values, the Standard Deviation (STD), Relative Standard Deviation (%STD) and the Standard Error (SE). The table containing the entire calculation can be found in **Appendix G-2**.

Table 4.4: Cumulative error calculation on specimen A2

Parameter	Symbol	Documented value	Min. value	Max. value	Unit	STD	%STD	SE
Specimen stiffness	S	545.584	542.856	545.570	N/mm	**1.919E+00**	**0.352%**	**6.069E-01**
Notch tip diameter	NTD	6.500	6.487	6.513	µm	**1.838E-02**	**0.283%**	**5.814E-03**
Characteristic length	$\overline{r}$	1.240	1.203	1.289	mm	**6.053E-02**	**4.880%**	**1.914E-02**
Critical mode I ERR (initiation)	G_{Ic}	1583.799	1576.281	1611.889	J/m^2	**2.518E+01**	**1.590%**	**7.962E+00**
Critical stress intensity factor	K_{Ic}	3.029	3.013	3.045	$MPa\sqrt{m}$	**2.244E-02**	**0.741%**	**7.096E-03**
Resistance at initiation (method 1)	G_{Ic}	854.414	852.634	867.070	J/m^2	**1.021E+01**	**1.195%**	**3.228E+00**
Resistance at initiation (method 2)	G_{Ic}	1028.910	1014.470	1054.730	J/m^2	**2.847E+01**	**2.767%**	**9.002E+00**

4.5 Fractography

Just like the preliminary specimens, the RR specimens have been subjected to SEM as well in the same way as the preliminary specimens were. First, the crack neatness is presented in **Figure 4.7**. What can be seen is that the crack shows little fiber/fiber bundle separation from the other side of the specimen, indicated by a smooth crack tip line. Furthermore, it can be seen that the top of most fibers are fractured by the blade in the process of repetitive cutting. The grey areas are cut carbon fibers, whereas the white areas represent the LMPAEK matrix material.

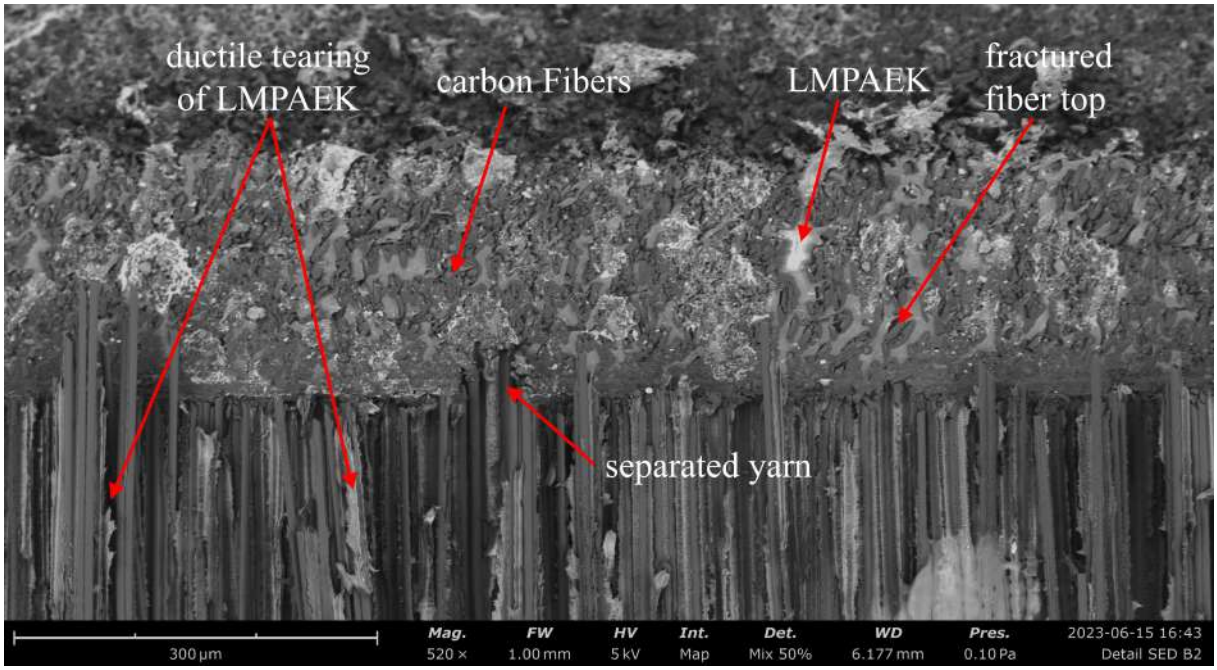

Figure 4.7: SEM picture of the pre-crack, viewed normal to the cracked surface

Figure 4.8 shows SEM images of the cracked surface of four RR specimens. As can be seen, the cracked surface is quite messy, having lots of pulled fibers/fiber bundles and the matrix seems to fracture in a ductile way. In contrary, the separation of the two specimen halves has been done by brittle fracture, clamping one end and swiftly removing the other with a hammer, as explained in **Section 3.5.1**. This transition from ductile crack propagation to brittle fracture, globally indicates the maximum crack length reached during testing. The all determining question is whether the measurements done from the side of the specimen, translates to an accurate crack length inside of the specimen. The first remark here is that the crack front by itself is not a straight line due to the local micro-structure around the crack front. The crack front cannot exactly be indicated due to the fact that separating the two specimen halves may have increased the crack front a bit before it fractured in a brittle way. However, the fracture of fibers/fiber bundles can be seen on the crack line. This fracture is due to the separation of the two halves. When

compared to the dotted red line, the seem to agree quite well, with some fiber bundles having fracture prior to the line and some after.

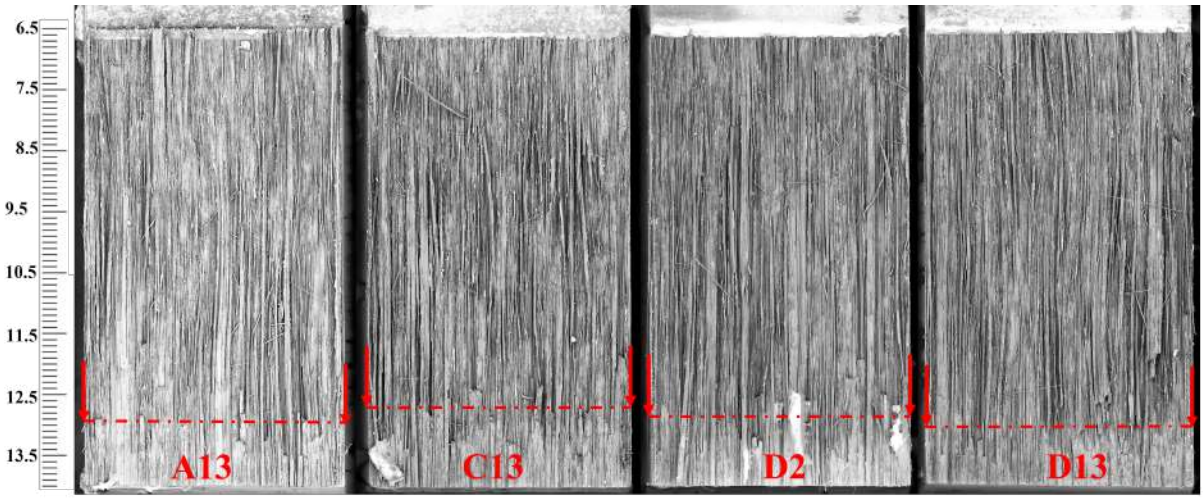

Figure 4.8: SEM images of the cracked surfaces, viewed normal to the cracked surface, with maximum reached crack length for several RR specimens

Figure 4.9 shows a SEM image of the fracture mechanics present in the propagation of intralaminar cracks. It can be seen that debonding of the fiber-matrix interface is a prominent failure. This, by lots of clean fibers, indicating debonding and debonded interfaces. Furthermore, ductile matrix tearing is present. It can be seen that the matrix material is pulled in a ductile manner by the pulled peaks, having large plastic deformation before fracture. Lastly, matrix residue is present on some fibers.

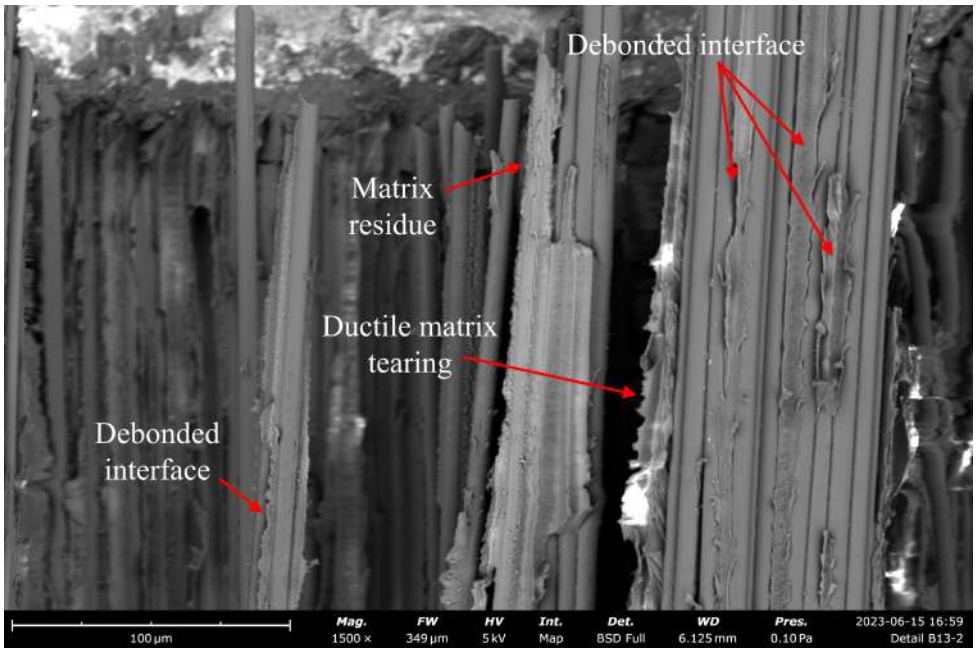

Figure 4.9: SEM images of the cracked surfaces, viewed normal to the cracked surface, showing: fiber-matrix interface debonding, ductile matrix failure and matrix residue

5 | Testing protocol and Round Robin recommendations

Since the ISO 13586 standard is already a very complete and proven standard on its own, it has been decided that instead of copying the standard largely, a testing protocol will be provided as and appendix with: specimen size recommendations, machining recommendations, pre-crack cutting recommendations, a crack length monitoring method and two calculation methods for the characterizing R-curve. The written ISO 13586 appendix is appended in **Appendix A**. This, to avoid repetition since every recommendation has been reviewed during this report.

5.1 Accordance with ISO 13586 and ISO 15024

This section will provide a list of items for the testing of Mode I longitudinal intralaminar fracture toughness of CFRPs that are in accordance with ISO 13586 and ISO 15024.

ISO 13586

1. First, the determination of G_{Ic} at fracture initiation will be done equally to what is described in the standard. This, using $\phi(a/w)$ as explained in **Section 2.3**.
2. Second, the determination of K_{Ic} at fracture initiation will be done equally to what is described in ISO 13586 as well. This using $f(a/w)$ and $\phi(a/w)$ as explained in **Section 2.3**.
3. Third, the standard testing conditions according to ISO 291 apply (i.e., standard atmosphere of 23°C ±2°C with 50% ±10% humidity).
4. Next, the determination of the uni-axial tensile- and compression properties σ_y of CF/LMPAEK will be done according to ISO 527-1 and ISO 604, just as described in ISO 13586. This is only necessary if the results are cross checked by the percentual difference of E_{stiff} and E_{fract}.
5. The machine requirements according to ISO 5893 apply for the Mode I longitudinal IFT testing as well (i.e., the constant displacement of 1mm/min shall differ maximum 0.2mm/min from the set value).
6. The requirements for the SENB setup geometry are in accordance with ISO 13586 (i.e the indentation of the rollers shall is minimized by the use of rollers with a large diameter of $> W/2$)
7. The measurement of the specimens itself (i.e., W, h and l) is in accordance as well. The mentioned dimensions shall be measured with an accuracy of 0.02mm.
8. Furthermore, $\frac{F_{max}}{F_5} < 1.1$, is checked as in ISO 13586. If more than 10% linearity is present, than the test shall be rejected.
9. Lastly, the application of the setup and specimen compliance correction (i.e., displacement correction) is applied to the measured force-displacement curve as in ISO 13586.

ISO 15024

1. The application of a CBT method is applied to the Mode I longitudinal IFT to calculate G_{Ic} for crack propagation as well. However, it is still in an experimental phase and more measurements shall be done to check the validity and its limits.

5.2 What should be done differently?

ISO 13586

1. First, ISO 2818 is not used for machining since the standard is for the use of polymers. Instead, for the machining of the more abrasive CFRP SENB specimens, it is recommended to use a 90 degree uncoated solid carbide chamfering cutter tool, with a feed rate of 200mm/min and a rotational speed of 2000rpm to produce clean cut surfaces.

2. The testing speed has been reduced to 1mm/min instead of the recommended 10mm/min. This ensures better crack tip tracking with LabVIEW.

3. For the specimen dimensions, the guidelines of ISO 13586 are adhered but the span S is increased (i.e., longer than necessary), to decrease specimen stiffness and subsequently the characteristic length $\overline{r}$. However, it is still questionable whether the notion of a plastic zone can be identified at all due to the highly anisotropic nature of a CFRP. Furthermore, the initial crack length a_0 is kept as small as possible within the limits, to allow for longer tracking without excessive plasticity.

4. Furthermore, the edited ESIS TC04 notching method for pre-cracking is used instead of the razor sliding/tapping method proposed in ISO 13586. This, to ensure higher accuracy and, above all, better consistency. Furthermore, the recommended pre-crack depth is 100µm. This value produced the sharpest NTD, inching closer to a naturally occurring intralaminar crack due to outside forces.

5. The measurement of crack length is done with microscopy on both sides of the specimen, while simultaneously investigating the pre-crack neatness.

6. Size criteria need not to be checked due to the questionable existence of a plastic zone by the anisotropic nature of a CFRP. However, it should be made sure that the crack length does not exceed $0.8W$ in the determination of the R-curve due to the effect of excessive plasticity in the ligament width.

7. The test report requirements are largely the same as ISO 13586, minus the size criteria check. However, additionally, the R-curves shall be presented (calculated by both methods).

8. The 'pop-in' phenomenon, as mentioned in the Annex of ISO 13586, needs not to be checked since it did not occur in any Mode I longitudinal intralaminar SENB test done in this research.

9. Finally, the cross check of results between E_{stiff} and E_{fract} to check the accuracy of the results shall not determine the validity of the test. This since the local micro-structure in intralaminar cracks influences the Young's modulus in this direction, deviating from the Young's modulus of LMPAEK. However, the values can be determined to see what the difference between both is.

5.3 Round-Robin recommendations

For the Round-Robin, several recommendations can be made:

1. At least ten specimens from different positions in the laminate should be tested. This, to avoid deviation of results due to local voids and/or different local thickness. The amount of ten specimens ensures a maximum error margin of 30% with a 95% probability out of population of 92 specimens (**Section 4.1**).

2. Furthermore, it is recommended to calculate the relative standard deviation (%STD) for all measurements and results. This gives insight into the variation and precision of values.

3. Finally, it has been decided to only focus on G_{Ic} and K_{Ic} at crack initiation during the Round-Robin. This, since no method to calculate G_{Ic} for crack propagation in SENB specimens exists, whereas a proven test standard for the G_{Ic} and K_{Ic} at crack initiation, does exist. However, more insight into the R-curve for CFRP SENB specimens is always welcome.

4. For further recommendations on testing and specimen preparation, the reader will be refered to the testing protocol in **Appendix A**.

6 | Discussion

This chapter will discuss several choices made and will reflect on the experimental methods and the Round-Robin results. The design of a testing standard is a resource intensive, non-straightforward process, requiring constant reflection and discussion regarding the choices made. As a reader, you have probably noticed that **Chapters 3** and **4** and **Appendix B** are written in a way of ongoing discussion to reflect the process of designing the test in a more fitting way. Besides, this reporting style has been chosen such that the information is still fresh for you as a reader, making it easier to understand. As a result, this chapter will not repeat the previous discussion but rather elaborate on other important points/findings that have not been discussed yet.

The points of discussion have been listed below. Each point will be introduced and afterwards discussed.

- First, in has been mentioned in **Section 2.6** that the two requirements for the application of LEFM are linear elastic material behaviour and a plane-strain condition at the crack tip. Furthermore, the section mentions the assumption of isotropy. The isotropic assumption could be violated by the following phenomena. First, stable crack propagation in longitudinal intralaminar cracks is limited due to the nature of a CFRP material. A crack could initiate by fiber-matrix debonding, encounter matrix-rich regions, and require a higher energy release rate G to propagate. Or a crack jumps a fiber or fiber bundle, and debonds along the other direction of the fiber or fiber bundle since it requires less energy, and causes fiber-bridging. This, in turn, halts the crack propagation when the strong fiber or fiber bundles encounter tension.

  In the testing of SENB specimens during this research the anisotropy of the material did not seem to influence the overall R-curve of the material much. What could be seen were some 'bumps' due to ply/fiber bridging on the crack propagation line in the force-displacement plots, however that did not change the overall shape and the crack propagation seems consistent. Furthermore, the influence of ply/fiber bridging is not that present in the chosen SENB geometry since the crack opening is small at all times. When compared to a DCB specimen, the crack opening is way larger, and the bridging fibers really influence the results significantly. This is a big advantage of using a SENB geometry.

- The SENB geometry however, only allows for a short CTP tracking (approximately 4.6mm with chosen dimensions) when assuming linear elasticity and calculating G_{Ic} using the CBT method. This since excessive plasticity is present at higher a/w ratios. When using the polynomial fit method to the $\frac{dU_2}{da}$ curve, the unrecoverable plastic deformation energy is not part of the equation, thus enabling longer tracking. However, what was noticed during testing is that at high a/w values, the crack does not propagate or only propagates very little due to the high compliance of the ligament width, indicating the limits of the SENB specimen.

- In **Section 3.5.1** it was decided that the RR specimen would be cut at a pre-crack depth of 0.1mm. This decision was based on the apparent trend of lower G_{Ic} and K_{Ic} at this pre-crack depth. However, it should be noted that the difference was only marginal. Furthermore, the ISO 13586 standard mentioned that for SFRPs, a NTD of <15µm, usually seemed to provide good values of G_{Ic} and K_{Ic}. It might be the case that the gain of an even sharper pre-crack is marginal and not exactly necessary. However, the lower the values of G_{Ic} and K_{Ic}, the closer the relation to reality.

- Furthermore, when pre-crack cutting the SENB specimens at a depth of 0.1mm, the criteria of a minimum pre-crack depth of 4xNTR, mentioned by ESIS TC04 and ISO 13586, had been violated.

However, the results of a pre-crack depth of 0.1mm proved promising compared to the results of a pre-crack depth of 0.8mm. It should be noted that this criteria is meant for isotropic polymer specimens, which, as seen in this report, does not always translate directly to CFRPs.

- When calculating the G_{Ic} values for crack initiation and G_{Ic} values for crack propagation, large differences can be observed. Where the average G_{Ic} for crack initiation is $1436 J/m^2$ (**Figure 4.1**), the first value of G_{Ic} for crack propagation is $920 J/m^2$ for method 1 and $900 J/m^2$ for method 2 (**Table 4.2**). This deviation has everything to do with the energy used for the calculation of G_{Ic}. ISO 13586 assumes $U_1 = U_3$ at fracture initiation due to spontaneous brittle fracture of polymers. However, when testing CFRP SENB specimens, there is residual stored elastic energy, due to the specimen not fracturing in a spontaneous brittle way. This raises the discussion on the incompatibility of both methods. The question arises whether a G_{Ic} value for initiation should be defined at all, since $U_1 \neq U_3$ at fracture initiation for CFRPs. The ISO 15024 for example, does not speak of G_{Ic} at fracture initiation either. Rather, an R-curve should be determined that determines the resistance to crack propagation at different crack lengths. What can be done however, is to define the required energy to fracture as U_3 at crack initiation. The usability of this required energy for fracture initiation in composite design is not straightforward since it is geometry dependent and a solution has to be found.

- Furthermore, the energy calibration factor $\phi(a/w)$, applied in the calculation of G_{Ic} at crack initiation to account for a difference in load-line compliance is still used. However, the application of such a factor for the G_{Ic} during crack propagation still requires research. It has been observed that the proposed CBT method is accurate for G_{Ic} values during crack propagation, but deviates from the actual G_{Ic} values after crack lengths of $0.8W$ due to excessive plasticity at the crack tip. Furthermore, it seems to deviate from the initiation values of G_{Ic} as well, albeit due to the polynomial fit expressions.

7 | Conclusion and recommendations

After completion of the this project and corresponding research, this chapter will first and foremost answer the main research question set in **Section 1.3**. By answering this question thoroughly, the sub-questions are answered as well. Thereafter, there will elaborated on several recommendations made for further research.

7.1 Conclusion

How can the longitudinal Mode I intralaminar fracture toughness and subsequent R-curve of CFRPs be determined with high precision and reproducibility at quasi-static loading rates?

First, research has shown that CT, SENB and DCB setups have been used in experimental research. Several relevant standards for the testing of fracture toughness are: ISO 13586 [2], ISO 15024 [3] and the ASTM equivalent, ASTM D5045 [49]. All three were used in the design of the test setup and protocol.

The longitudinal Mode I intralaminar fracture toughness K_{Ic} can be determined by the following. Single edge notched bending can be used as test geometry with fibers in crack direction, adhering to the ISO 13586 specimen dimension guidelines [2], except, a larger span S is used to decrease specimen stiffness and subsequently $\overline{r}$.

The initial notch in the specimen can be created by milling the entire depth in one go with a special holder, containing polymer sacrificial material to prevent burrs on the CFRP. The milling shall be done with a 90° uncoated solid carbide chamfering cutter tool at 2000rpm and a feed rate of 200mm/min. This ensures a neat surface finish.

Then, the pre-crack in the specimen can be created in a precise and consistent way with use of a adapted microtome and razor blades in a pre-cracking method brought forward by ESIS TC04 [50]. It is recommended to use one Stanley® carbide blade per specimen and only cut one specimen at a time. Furthermore, it is recommended to create a pre-crack of 0.1mm depth to allow for the sharpest notch tip diameter possible, subsequently decreasing K_{Ic}, closer resembling a naturally occurring crack.

The value of K_{Ic} at fracture initiation shall be calculated with use of the LEFM method presented in ISO 13586, however the size criteria need not to be checked since it is questionable if the notion of a plastic zone can be identified at all with CFRPs.

After testing, the setup- and specimen compliance shall be corrected for according to ISO 13586. For the determination of G_{Ic} during crack propagation, an algorithm in a LabVIEW implementation can be used that tracks the crack tip position by difference in contrast. For this contrast, the crack area needs to be prepared with a matte white spray paint.

The obtained data (time [s], force [N], displacement [mm], and crack length [mm]) can be reduced by 2 methods. The first method makes use of a scatter cross plot of the cumulative released energy U_2 over the crack length a, whereafter the polynomial fit that best fits the data is then differentiated exactly, yielding $R(a)$. The second method makes use of CBT theory, providing an equation for $G(a)$ assuming linear elasticity of the entire a/W regime. However, due to excessive plasticity at high a/W values, this method is valid up to a crack length of $0.8W$.

The use of a LabVIEW algorithm for crack tip tracking and an adapted microtome for pre-crack cutting ensures high precision and reproducibility. The critical Mode I energy release rate at initiation G_{Ic} has a Relative Standard Deviation (%STD) of $\sim$10%, with a %STD of 1.59% on the precision. Next, the critical stress intensity factor at initiation K_{Ic} has a %STD of $\sim$6%, with a %STD of 0.74% on the precision. Furthermore, the Notch Tip Diameter (NTD) and maximum force reached have a %STD of $\sim$23% and $\sim$6% respectively, with the latter having a %STD of 0.03% on the precision.

7.2 Recommendations

With knowledge from literature research in **Chapter 2**, the experimental methods applied in **Chapter 3** and **Appendix B** and the Round-Robin test results in **Chapter 4**, a list of several recommendations can be formulated for future work. The items below are first introduced, whereafter a short explanation has been given per item.

1. The size criteria, as introduced in **Section 3.2.1** regarding the relative size of the plastic zone compared to other parameters, have been deemed obsolete. If this really is the case, can be checked by altering the different dimensions within given dimension ranges in ISO 13586, whereafter it can be checked if the results for K_{Ic} and G_{Ic} at fracture initiation change within these ranges.

2. It is interesting to see whether the notion of a plastic zone can be identified at all for a CFRP and whether it correlates with the characteristic length $\overline{r}$. Therefore, it is recommended to perform a FEM plastic zone simulation with an anisotropic material with fibers and matrix material modelled separately in a random dispersion.

3. The two methods to calculate G_{Ic} during crack propagation seem to agree up to high a/w values at a crack length of $0.8W$. Afterwards, the method based on a CBT, overestimates the materials ability to store and release elastic energy U_3, causing the energy release rate to increase compared to the real life case. It is recommended to find correction factors for changing load-line compliance due to increased plasticity in calculating G_{Ic} based on this CBT method. This can be done by testing SENB specimens and unloading them at several CTPs. Then, the slope of this unloading line, being the compliance, would determine the actual change in compliance over crack length a. Finally, the CBT method formula for $C(a)$ can be compared with the real life data, and correction factors can be determined.

4. Another method to account for non-linearity is the application of EPFM and the corresponding J-integral. It is recommended that research into the application of EPFM is performed for future implementation of a SENB specimen in the longitudinal Mode I IFT.

5. Furthermore, it is recommended to create a LabVIEW implementation that takes the derivative of $\frac{dU_2}{da}$ automatically or periodically instead of trying to fit a polynomial equation afterwards. This reduces the required effort in calculating the R-curve.

6. It is recommended to compare the K_{Ic} results for crack initiation with those of a DCB test of the same material. This gives insight in whether the initiation of delamination fracture requires less stress than intralaminar fracture, or if the opposite is true. Furthermore, the comparison of the R-curves in both interlaminar as intralaminar fracture for the tested material in this research is interesting. This knowledge is paramount in the design and failure prediction of composite materials in the future.

7. The blades used in the pre-cracking of a SENB specimen with a microtome are Stanley® carbide blades. These blades have a high abrasion resistance but do suffer from occasional brittle failure. For further work in perfecting the pre-cracking method using a microtome it should be checked whether other blades provide just as sharp a crack when pre-cracking at 0.1mm depth and see if brittle failure occurs as well for these blades. If the pre-crack seems just as sharp and brittle failure occurs less or not at all with a certain other type of blade, these blades are preferred.

8. Next, the pre-cracking of a specimen by using the edited ESIS TC04 method provides accurate and consistent pre-cracks resulting in a relatively low K_{Ic}. However, another method used to simulate a naturally occurring crack is fatigue pre-cracking. Here, a specimen is cyclically loaded until a

certain pre-crack forms naturally. This method provides the most representable results of K_{Ic} at crack initiation due to the crack having formed naturally. However, the fatigue pre-cracking of a specimen takes a large amount of time compared to the pre-cracking with a microtome. In further application of the longitudinal Mode I IFT SENB test, the option of applying fatigue pre-cracking should definitely be researched.

9. Regarding the crack tip tracking, the SENB geometry enables little crack propagation. First, the initial pre-crack length should adhere the dimension guideline of $0.45W \leq a \leq 0.55W$ and second, the R-curve should not include crack lengths a larger than $0.8W$. That leaves $0.35W$ to generate a valid R-curve when assuming linear elastic material behaviour. To be able to track the propagation for a longer distance, other kinds of specimen geometries should be researched such as a special intralaminar DCB or a CT geometry. The added benefit of this is less noise/scatter in division by da in the $\frac{dU_2(a)}{da}$ in determination of $R(a)$. Furthermore, it is recommended to look into the smoothing of the $a(x)$ curve, prior to fitting a polynomial and taking the exact derivative, if the SENB geometry is used. This, either in LabVIEW or in data reduction.

10. Lastly, the definition of G_{Ic} at fracture initiation of a CFRP according to ISO 13586 is at least dubious, if not inapplicable, since fracture does not occur in a spontaneous brittle way, and thus residual stored elastic energy U_3 is left after fracture initiation. What can be defined however, is the energy to fracture initiation, being the work input U_1 to fracture initiation. The usability of this required energy for fracture initiation in composite design and failure prediction is not straightforward since it is geometry dependent and more research is needed into its usability in fracture mechanics.

Bibliography

[1] B. F. Dale. (2008) Fracture modes. [Online]. Available: https://en.wikipedia.org/wiki/File:Fracturemodesv2.svg

[2] *ISO 13586: Determination of Fracture Toughness (GIC and KIC): Linear Elastic Fracture Mechanics (LEFM) Approach*. Organización Internacional de Normalización, 2000. [Online]. Available: https://books.google.nl/books?id=Oo5JjwEACAAJ

[3] *ISO 15024: Fibre-reinforced plastic composites: Determination of mode I interlaminar fracture toughness GIC for UD reinforced materials*. Organización Internacional de Normalización, 2001. [Online]. Available: https://books.google.nl/books?id=ZW0oOAAACAAJ

[4] *ISO 17281: Plastics-Determination of fracture toughness (GIC and KIC) at moderately high loading rates (1 m/s)*. Organización Internacional de Normalización, 2018.

[5] (2023) Round robin test. [Online]. Available: https://www.centexbel.be/en/lexicon/round-robin-test

[6] (2023) Toray cetex® tc1225. [Online]. Available: https://www.toraytac.com/product-explorer/products/gXuK/Toray-Cetex-TC1225

[7] D. Uil, "Influence of loading rate on the longitudinal mode i intralaminar fracture toughness of cfrps and the applicability of an lefm approach," November 2022.

[8] G. Kirsch, *Die Theorie der Elastizität und die Bedürfnisse der Festigkeitslehre*. Springer, 1898. [Online]. Available: https://books.google.nl/books?id=pvBuPwAACAAJ

[9] C. Inglis, "Stresses in a plate due to the presence of cracks and sharp corners," 1913.

[10] A. A. Griffith, "The phenomena of rupture and flow in solids," *Philosophical Transactions of the Royal Society of London. Series A, Containing Papers of a Mathematical or Physical Character*, vol. 221, pp. 163–198, 1921. [Online]. Available: http://www.jstor.org/stable/91192

[11] H. M. Westergaard, "Bearing pressures and cracks: Bearing pressures through a slightly waved surface or through a nearly flat part of a cylinder, and related problems of cracks," 1939.

[12] G. R. Irwin, "Analysis of stresses and strains near the end of a crack traversing a plate," 1957.

[13] S. Suresh, *Fatigue of Materials*, ser. Cambridge Solid State Science. Cambridge University Press, 1998. [Online]. Available: https://books.google.nl/books?id=j4w6frFAiQcC

[14] B. McGinty. (2023) Stress intensity factor. [Online]. Available: https://www.fracturemechanics.org/sif.html

[15] M. Iwamoto, Q.-Q. Ni, T. Fujiwara, and K. Kurashiki, "Intralaminar fracture mechanism in unidirectional CFRP composites: Part I: Intralaminar toughness and AE characteristics," *Engineering Fracture Mechanics*, vol. 64, no. 6, pp. 721–745, 1999. [Online]. Available: https://www.sciencedirect.com/science/article/pii/S001379449900096X

[16] Y. Wang, Y. Wang, B. Han, B. Wan, G. Cai, and R. Chang, "In situ strain and damage monitoring of gfrp laminates incorporating carbon nanofibers under tension," *Polymers*, vol. 10, 7 2018.

[17] L. P. Canal, C. González, J. Segurado, and J. LLorca, "Intraply fracture of fiber-reinforced composites: Microscopic mechanisms and modeling," *Composites Science and Technology*, vol. 72, no. 11, pp. 1223–1232, 6 2012.

[18] A. C. Garg, "Intralaminar and interlaminar fracture in graphite/epoxy laminates," *Engineering Fracture Mechanics*, vol. 23, no. 4, pp. 719–733, 1986. [Online]. Available: https://www.sciencedirect.com/science/article/pii/0013794486901189

[19] J. L. Lataillade, M. Delaet, F. Collombet, and C. Wolfft, "Effects of the intralaminar shear loading rate on the damage of multi-ply composites," Tech. Rep. 6, 1996.

[20] M. Tanoglu, S. H. Mcknight, G. R. Palmese, and J. W. Gillespie, "A new technique to characterize the fiber/matrix interphase properties under high strain rates," 2000. [Online]. Available: www.elsevier.com/locate/compositesa

[21] G. Pappas and J. Botsis, "Intralaminar fracture of unidirectional carbon/epoxy composite: Experimental results and numerical analysis," *International Journal of Solids and Structures*, vol. 85-86, pp. 114–124, 5 2016.

[22] B. G. Falzon and P. Apruzzese, "Numerical analysis of intralaminar failure mechanisms in composite structures. Part I: FE implementation," *Composite Structures*, vol. 93, no. 2, pp. 1039–1046, 1 2011.

[23] S. Nemat-Nasser, "Introduction to high strain rate testing," Tech. Rep., 2000. [Online]. Available: https://www.researchgate.net/publication/285472544

[24] A. Faye, S. Basu, and V. Parameswaran, "Effect of loading rate on dynamic fracture toughness of polycarbonate," in *Conference Proceedings of the Society for Experimental Mechanics Series*, vol. 1, 2014, pp. 139–145.

[25] H. Wada, "Determination of dynamic fracture toughness for PMMA," Tech. Rep. 6, 1992.

[26] T. Kobayashi, H. Miyata, K. Kikusawa, and T. Higashihara, "Instrumented impact test and evaluation of fracture toughness in PMMA," Tech. Rep., 1989.

[27] T. Weerasooriya, P. Moy, D. Casem, M. Cheng, and W. Chen, "Fracture Toughness for PMMA as a Function of Loading Rate," Tech. Rep., 2006. [Online]. Available: https://www.researchgate.net/publication/268361274

[28] B. R. K. Blackman, A. Pavan, J. G. Williams, Z. Major, and R. W. Lang, "Fracture of Polymers, Composites and Adhesives II rate dependent fracture toughness of plastics," Tech. Rep., 2003.

[29] C. Kanchanomai, S. Rattananon, and M. Soni, "Effects of loading rate on fracture behavior and mechanism of thermoset epoxy resin," *Polymer Testing*, vol. 24, no. 7, pp. 886–892, 10 2005.

[30] J. Zhou, Y. Wang, and Y. Xia, "Mode I fracture toughness of PMMA at high loading rates," in *Journal of Materials Science*, vol. 41, no. 24, 12 2006, pp. 8363–8366.

[31] H. Wada, M. Seika, T. Kennedy, C. Calder, and K. Murase, "Investigation of loading rate and plate thickness effects on dynamic fracture toughness of pmma," *Engineering Fracture Mechanics*, vol. 54, no. 6, pp. 805–811, 1996. [Online]. Available: https://www.sciencedirect.com/science/article/pii/0013794495002448

[32] H. Wada, M. Seika, C. Calder, and T. Kennedy, "Measurement of impact fracture toughness for pmma with single-point bending test using an air gun," *Engineering Fracture Mechanics*, vol. 46, no. 4, pp. 715–719, 1993. [Online]. Available: https://www.sciencedirect.com/science/article/pii/001379449390178U

[33] D. Rittel, H. Maigre, D. Rittel, and H. Maigre, "An investigation of dynamic crack initiation in PMMA," *PMMA. Mechanics of Materials*, vol. 23, no. 3, 1996. [Online]. Available: https://hal.archives-ouvertes.fr/hal-00111525

[34] S. Huang, S.-N. Luo, and K. Xia, "Dynamic fracture initiation toughness and propagation toughness of PMMA," *Society for Experimental Mechanics - SEM Annual Conference and Exposition on Experimental and Applied Mechanics 2009*, vol. 3, pp. 1491–1499, 1 2009.

[35] M. Yazici, "Loading rate sensitivity of high strength fibers and fiber/matrix interfaces," *Journal of Reinforced Plastics and Composites*, vol. 28, no. 15, pp. 1869–1880, 8 2009.

[36] S. Tamrakar, B. Z. Haque, and J. W. Gillespie, "High rate test method for fiber-matrix interface characterization," *Polymer Testing*, vol. 52, pp. 174–183, 7 2016.

[37] Z. Jendli, J. Fitoussi, F. Meraghni, and D. Baptiste, "Anisotropic strain rate effects on the fibre-matrix interface decohesion in sheet moulding compound composites," *Composites Science and Technology*, vol. 65, no. 3-4, pp. 387–393, 3 2005.

[38] J.-M. Chu, B. Claus, N. Parab, D. O'Brien, T. Sun, K. Fezzaa, and W. Chen, "Visualization of dynamic fiber-matrix interfacial shear debonding," *Journal of Materials Science*, vol. 53, 04 2018.

[39] S.-L. Gao and J.-K. Kim, "Cooling rate influences in carbon fibre/peek composites. part 1. crystallinity and interface adhesion," *Composites Part A: Applied Science and Manufacturing*, vol. 31, no. 6, pp. 517–530, 2000. [Online]. Available: https://www.sciencedirect.com/science/article/pii/S1359835X00000099

[40] T. Q. Li, M. Q. Zhang, K. Zhang, and H. M. Zeng, "The dependence of the fracture toughness of thermoplastic composite laminates on interfacial interaction," *Composites Science and Technology*, vol. 60, no. 3, pp. 465–476, 2000. [Online]. Available: https://www.sciencedirect.com/science/article/pii/S0266353899001475

[41] S. D. Park, M. Todo, K. Arakawa, and M. Koganemaru, "Effect of crystallinity and loading-rate on mode i fracture behavior of poly(lactic acid)," *Polymer*, vol. 47, no. 4, pp. 1357–1363, 2 2006.

[42] P. Beguelin and H. H. Kausch, "The effect of the loading rate on the fracture toughness of poly(methyl methacrylate), polyacetal, polyetheretherketone and modified pvc," *Journal of Materials Science*, vol. 29, pp. 91–98, 1994. [Online]. Available: https://doi.org/10.1007/BF00356577

[43] J. G. Williams, "Fracture mechanics of polymers," *Ellis Horwood Limited, Market Cross House, Cooper St, Chichester, West Sussex, PO 19, 1 EB, UK, 1984. 302*, 1984.

[44] Z. Suo. (2014) Linear elastic fracture mechanics. [Online]. Available: https://imechanica.org/files/Linear%20elastic%20fracture%20mechanics%202014%2003%2008.pdf

[45] A. R. Shahani, R. Abolfathitabar, and H. Shooshtar, "On the validity of lefm methods to investigate the fracture behavior of angle-ply laminates," *Composites Part B: Engineering*, vol. 160, pp. 249–253, 3 2019.

[46] G. Frossard, J. Cugnoni, T. Gmür, and J. Botsis, "Ply thickness dependence of the intralaminar fracture in thin-ply carbon-epoxy laminates," *Composites Part A: Applied Science and Manufacturing*, vol. 109, pp. 95–104, 2018. [Online]. Available: https://www.sciencedirect.com/science/article/pii/S1359835X18300952

[47] M. W. Czabaj and J. G. Ratcliffe, "Comparison of intralaminar and interlaminar mode i fracture toughnesses of a unidirectional im7/8552 carbon/epoxy composite," *Composites Science and Technology*, vol. 89, pp. 15–23, 2013. [Online]. Available: https://www.sciencedirect.com/science/article/pii/S0266353813003709

[48] M. Iwamoto, Q.-Q. Ni, T. Fujiwara, and K. Kurashiki, "Intralaminar fracture mechanism in unidirectional CFRP composites — part II: analysis," *Engineering Fracture Mechanics*, vol. 64, no. 6, pp. 747–764, 1999. [Online]. Available: https://www.sciencedirect.com/science/article/pii/S0013794499000971

[49] D20 Committee, *Test methods for plane-strain fracture toughness and strain energy release rate of plastic materials*, West Conshohocken, PA, 2022.

[50] R. de Oliveira, "Notching of polymers." ESIS, September 2019.

[51] I. S. University. (2023) Fracture toughness. [Online]. Available: https://www.nde-ed.org/Physics/Materials/Mechanical/FractureToughness.xhtml

[52] W. Brown, Ed., *Review of Developments in Plane Strain Fracture Toughness Testing*. ASTM International, Jan. 1970. [Online]. Available: https://doi.org/10.1520/stp463-eb

[53] S. K. Kudari and K. G. Kodancha, "3d finite element analysis on crack-tip plastic zone," *International Journal of Engineering, Science and Technology*, vol. 2, no. 6, Feb. 2011. [Online]. Available: https://doi.org/10.4314/ijest.v2i6.63698

[54] F. Zúñiga, J. Kalthoff, A. Fernández-Canteli, J. Grasa, and M. doblaré, "Three dimensional finite element calculations of crack tip plastic zones and k ic specimen size requirements," 07 2023.

[55] S. Kudari and K. Kodancha, "Effect of specimen thickness on plastic zone," *17th European Conference on Fracture 2008: Multilevel Approach to Fracture of Materials, Components and Structures*, vol. 1, pp. 530–538, 01 2008.

[56] J. Wieringa, "Measurement of the deformation rate dependency of the fracture toughness of continuous fibre reinforced polymers," 2021.

[57] *ISO 2818: Preparation of test specimens by machining*. Organización Internacional de Normalización, 2018. [Online]. Available: www.iso.org

[58] M. M. Houck and J. A. Siegel, "Paint analysis," *Fundamentals of Forensic Science*, pp. 405–426, 2015.

[59] Instron. (2023) Ceast specimen preparation notching machines. [Online]. Available: https://www.instron.com/en/products/testing-accessories/specimen-measuring-preparation/specimen-preparation-systems/ceast-specimen-preparation-notching-machines

[60] A. Bakker, "Compatible compliance and stress intensity expressions for the standard three-point bend specimen," *Fatigue & Fracture of Engineering Materials & Structures*, vol. 13, pp. 145 – 154, 04 1990.

[61] J. Nairn, "Analytical and numerical modeling of r curves for cracks with bridging zones," *International Journal of Fracture*, vol. 155, pp. 167–181, 02 2009.

[62] E. HEARN, "Chapter 11 - strain energy," in *Mechanics of Materials 1 (Third Edition)*, third edition ed., E. HEARN, Ed. Oxford: Butterworth-Heinemann, 1997, pp. 254–296. [Online]. Available: https://www.sciencedirect.com/science/article/pii/B9780750632652500128

[63] Cuemath. (2023) Sample size formula. [Online]. Available: https://www.cuemath.com%2Fsample-size-formula%2F

[64] J. Franke. (2023) Depth of field (dof), angle of view, and equivalent lens calculator. [Online]. Available: https://www.pointsinfocus.com/tools/depth-of-field-and-equivalent-lens-calculator/

A | Testing Protocol: Determining the longitudinal Mode I longitudinal intralaminar fracture toughness of a Continuous Fiber Reinforced Polymer (CFRP) with an LEFM approach

Testing Protocol: Determining the longitudinal Mode I longitudinal intralaminar fracture toughness of a Continuous Fiber Reinforced Polymer (CFRP) with an LEFM approach

Author: Dennis Uil, d.uil@student.utwente.nl

1 Introduction

this document will provide a guideline for testing of the longitudinal Mode I intralaminar fracture toughness and crack propagation resistance, characterized by the R-curve, of Continuous Fiber Reinforced Polymers (CFRPs) based on a Linear Elastic Fracture Mechanics (LEFM) approach. The guidelines in this protocol have been based on the ISO 13586:2018 standard for the determination of Mode I fracture toughness of Polymers and Short Fiber Reinforced Polymers (SFRPs). Rather, than repeating the ISO 13586 standard for a large proportion, this document aims to fill to the role of an appendix for this standard. For certain guidelines, that are equal for the testing of polymers as they are for the testing of CFRPs, this protocol will refer to the ISO 13586 standard. This means that any references to sections, tables, figures and equations, will refer to ISO 13586, unless indicated otherwise. Any deviations from the standard will be explained in this document.

2 Scope

This document specifies the principles for determining the fracture toughness of plastics in the crack opening Mode (Mode I) under defined conditions. A test method with pre-cracked specimens is defined, namely three-point-bending tests, or known as Single Edge Notched Bending (SENB).

This protocol is valid for CFRPs, either with rigid and semi-rigid thermoplastic matrix materials. Certain restrictions on the linearity of the load-displacement diagram, on the specimen geometry are imposed to ensure validity. This, since the protocol assumes linear elastic material behaviour of the cracked material and a state of plane strain at the crack tip. Finally, the crack needs to be sharp enough so that an even sharper crack does not result in significantly lower values of the measured properties, approaching a naturally formed longitudinal intralaminar crack.

3 Test specimen geometry

The test specimen SENB geometry, (ie., width W, overall length l, thickness h, and crack length a) should be according to the geometry guidelines presented in Figure 1. It is usually convenient to make the thickness h of the test specimens equal to the thickness of a laminate. The crack length a should preferably be in the range given by $0.45 \leq a/W \leq 0.55$. Good results have been obtained by a specimen length l of 70mm, width W of 14mm, and thickness h of $4.3mm$.

4 Specimen preparation

The section sets forth the steps needing to be taking in the preparation of specimens.

1. **Sawing the laminate:** First, the specimens shall be cut from the laminate in rectangular shapes. Good results have been obtained using a water cooled diamond blade saw. Good care shall be taken in cutting the specimens parallel to the fiber direction. Furthermore, each specimen shall be named in a consistent way.

2. **Specimen dimension documentation:** For each specimen, the height W, thickness h and length l shall be measured to the nearest 0.02mm using a micrometer. This, by measuring twice on each side of the specimen for all parameters. these values shall be documented following ISO 13586.

3. **Machining of the initial notch:** for the creation of the initial notch, a 90° v-notch geometry can be used. Previous tests have indicated good results with this geometry. The initial notch can be created by milling the specimen with a 90° 6mm uncoated solid carbide chamfering cutter tool. The recommended feed rate is 200mm/min. With a lower feed rate and a thermoplastic matrix material, the risk of damaging the surface by melting the material increases rapidly. Furthermore, a rotational speed of 2000rpm provided good results.

   It is recommended that for the specimen with specimen length l of 70mm, width W of 14mm, and thickness h of 4.3mm, an initial v-notch of 6.5mm is milled.

   It is preferable to create the notch geometry at an equal distance from the side of the specimen for each specimen. This can be done with a special holder, containing a 90° angle. This holder can be placed in the clamp of a milling machine. The holder has two sides, exactly 90° apart from each other. This ensures that the notch is at a constant distance from the left side of the specimens. The specimens shall be stacked as depicted in **Figure A.1** on the left. Between the specimens, several pieces of PMMA plastic are placed. This is done to mainly avoids burs on the composite SENB specimens. Next, the specimens are clamped by 2 bolts and a bridging piece of steel. Between the specimens and this piece of steel, a thin part of triplex is placed to avoid damaging the composite material while clamping. This can be seen in **Figure A.1** on the right. The holder itself is then placed in a milling machine, and the designated clamp fixates the specimens.

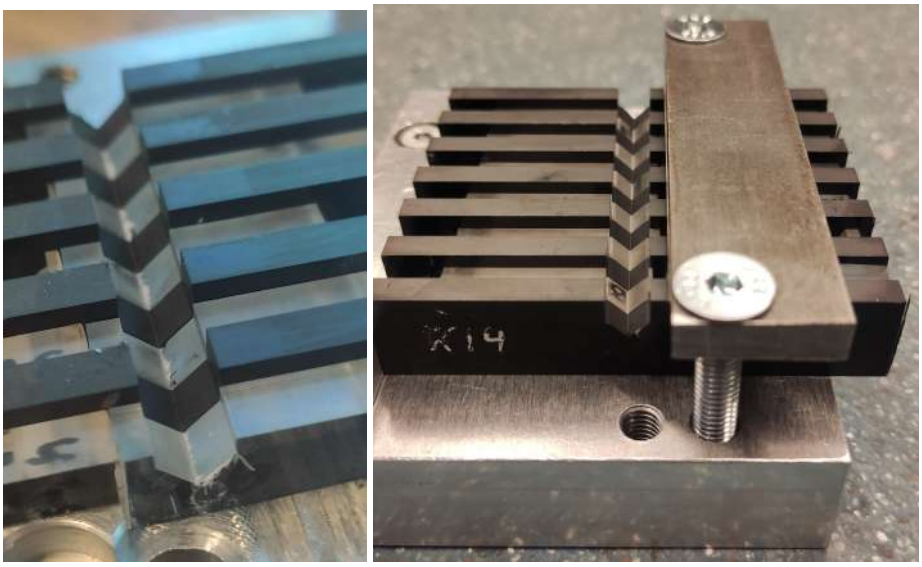

Figure A.1: Left: PMMA material between specimens to prevent burs, Right: clamping method prior to machining SENB specimens

5 Pre-crack cutting overview

In order to create a sufficiently sharp and, above all, consistent pre-crack on all specimens, the use of an adapted microtome and cutting blades is recommended. This method is brought forward by ESIS TC04 [50]. The sharper this crack can be, the closer it is to a crack that would form due to outside forces. In the world of fracture toughness tests, this is a topic of major importance. When a sharp pre-crack cannot be

formed, the resulting K_{Ic} is meaningless since the material would crack at a lower K_{Ic} in a real world application. In general it can be stated that the sharper the pre-crack, the lower the K_{Ic}.

The cutting cycle is presented in **Figure A.2** on the left. Furthermore, the used microtome itself is presented on the right in the same figure. One cycle consists of a forward step of 20 µm for the first millimeters to cut and a forward step of 10 µm for the final 0.1mm of the pre-crack. The cutting is performed in step 2, where the blade slices through the material. Step 3 is the step out of the material, or retraction. Finally, step 4 brings the blade back up to its first position, whereafter the cycle is repeated. The depth of the cut can be controlled by counting the number of cycles. For more information on this cutting method, the ESIS TC04 documentation can be consulted [50]. However, the steps and details in this protocol should be adhered to for the pre-crack cutting of CFRPs.

The blades are sharpened at an angle range θ and the angle range α as depicted in **Figure A.2**. Lowering θ, increases friction and non-perpendicular notches and create blunt crack tips, whereas increasing θ, results in the risk of damage to the blade. Lowering α would result in pushing/ploughing into the specimen, whereas increasing α would again increase the risk of damage to the blade. This all means that the original cutting surface of the blade is not the intended cutting surface in this method and the blade needs to be sharpened by wet sanding.

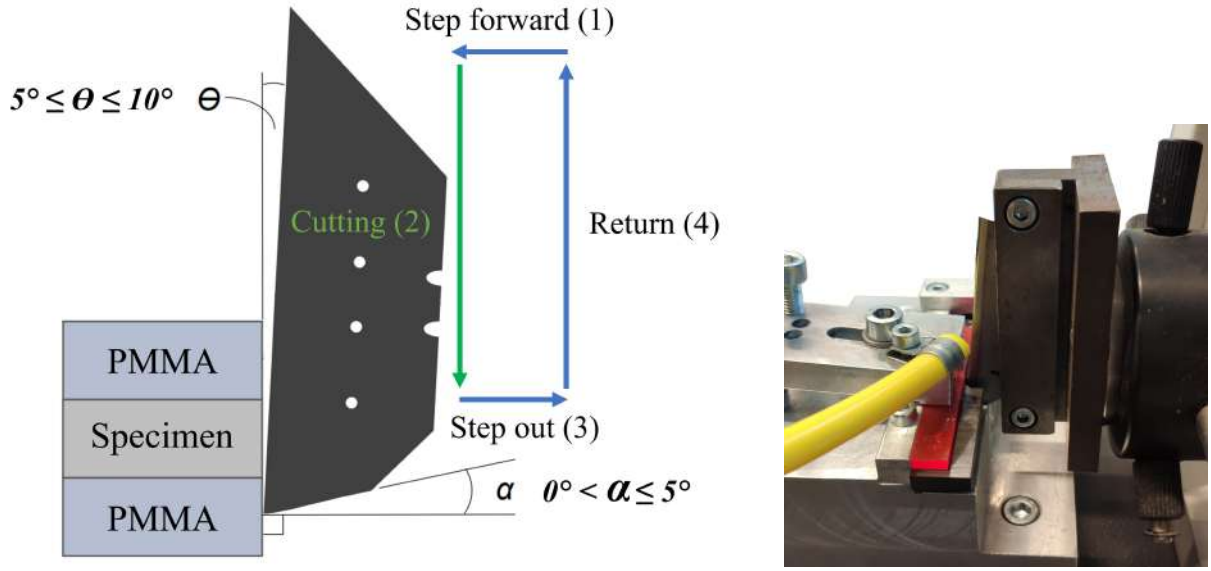

Figure A.2: Left: Blade orientation and cutting cycle steps [50], Right: microtome used in preparing SENB specimens

The various steps to create a pre-crack with use of a microtome are presented below. for more details, the ESIS TC04 method [50] can be consulted.

6 Blade preparation

This section elaborates on the blade preparation method used. The ESIS TC04 method provides more information [50].

1. **Microscopic blade examination before sharpening (if new blades are used, this step might be skipped):** The recommended blades to use in the pre-crack cutting are Stanley® Carbide blades. Before blade sharpening, the blades shall be microscopically examined for possible defects or amount of material to be removed due to damage in a previous cutting cycle.

2. **Blade sharpening:** The blades shall be sharpened at the angles in **Figure A.2** by wet sanding on a rotating platform. Silicon Carbide (SiC) sanding papers showed good results. The initial

millimeters to be removed, can be done with paper size 320. It was observed that the removal of 0.5mm takes 60 seconds at 150rpm with this paper. After removal of the initial millimeters, the blade can be sharpened by using paper sizes 1000, 2000 and 4000. This, all at 30 seconds each respectively (using paper 4000 is not and essential step).

3. **Microscopic blade examination after sharpening:** The cutting surface of the blades shall be observed for sharpness from the side and normal to the surface by microscopic examination, to see if the cutting surface is sufficiently sharp and does not contain defects.

7 Sacrificial polymer material cutting

In pre-crack cutting with use of an adapted microtome, sacrificial polymer material beams are placed on either side of the specimen, to prevent composite burs and damage due to clamping. Good results have been obtained with using PMMA beams. These beams shall either be sized by machining or laser cutting. The length shall equal the length l of a CFRP SENB specimen. The width W should equal or be larger than the ligament width of the SENB specimen, prior to pre-crack cutting. Here the ligament width is equal to the specimen width W minus the depth of the initially machined notch. The width W of the polymer material shall be checked with a micrometer.

8 Pre-crack cutting steps using an adapted microtome

1. **Blade placement in microtome:** The blade is placed in the specially adapted microtome, good care shall be taken not to damage the cutting surface in the process.

2. **Cleaning the cutting slot:** The detached burs from the previous cutting cycle shall be removed by compressed air.

3. **Zero-ing the microtome blade:** One piece of polymer sacrificial material is placed in the dedicated holder. Then, the microtome is advanced by hand per cycle until the blade is flush with the polymer material, indicating the position where the pre-crack should start if the polymer is cut to a width W of $W - a_0$. If the polymer sacrificial material has a longer width, calculate the amount of cycles to be cut before the CFRP material is reached. To check whether the blade is flush with the polymer rectangle, visual confirmation of a small scratch suffices. Furthermore, listening for a scratching sound works as well.

4. **determining the horizontal position of the pre-crack cut:** Prior to pre-crack cutting, the horizontal length from the side of the specimen to the tip of the initial v-notch shall be determined by microscopic examination. This for the final positioning of the specimen in the pre-crack cutting setup.

5. **Clamping:** The micrometer on the side of the dedicated fixture is set to accommodate the microscopically examined horizontal length in the previous step. This was found to provide the most accurate results in placing the blade as close to 'in plane' position of the initial notch tip as possible. Then, the two pieces of polymer material plus the specimen to be cut are placed in dedicated fixture according to **Figure A.2**. Make sure the specimen and polymer material sits flush against the holder. Afterwards the stack is clamped.

6. **pre-crack cutting:** The counted cycles on the microtome are set to 0, and the valve is opened to allow for compressed air through the vortex tube to eject burrs. It should be checked that the forward movement per cycle on the microtome is set to 20µm for the initial micrometers, then the cutting is started and the cycles are counted until 100µm is left to be cut.

Practice and microscopic examination have found a pre-crack depth of 100µm to result in the sharpest pre-crack possible for CFRPs, using Stanley® Carbide blades, subsequently closer resembling a natural crack. It is thus recommended to cut the pre-crack to this depth.

7. **Retraction:**

   After reaching the pre-crack depth the cutting is stopped, and the blade is retracted, whereafter the specimen including, the polymer sacrificial material is taken out of the dedicated holder. The loose burrs can be removed by compressed air.

9 Testing of the specimens

This section will elaborate on the testing of the specimens. For the machine requirements and required precision, the ISO 13586 standard can be followed.

1. **Specimen and machine compliance correction:** Regarding the Specimen and machine compliance correction method, the reader is referred to ISO 13586. It is noted that the correction should be performed for each change in material or testing circumstances such as temperature or humidity
2. **Testing conditioning:** Regarding the testing conditions, the ISO 13586 standard can be followed. As a guideline, the preferred atmosphere is (23±2)°C and (50±10)° relative humidity.
3. **Testing speed:** Good results for the crack length detection reading have been obtained with a constant displacement of 1mm/min.
4. **Determination of the crack initiation force:** For the determination of the crack initiation force, the reader is referred to ISO 13586. Furthermore, the mentioned condition of maximum 10% linearity present should be adhered to. If this is exceeded, the corresponding specimen shall be rejected and another one shall be tested in its place.

10 Data reduction to obtain G_{Ic} and K_{Ic} at fracture initiation

For the data reduction to obtain G_{Ic} and K_{Ic} at fracture initiation, the reader is referred to the ISO 13586 standard. Furthermore, it should be noted that the size criteria of the plastic do not have to be checked since it is questionable if the notion of a plastic zone can be identified at all with a CFRP. Similarly, the cross check of results by checking the difference of E_{fract} and E_{stiff} to be less than 15%, shall not determine the validity of the test.

11 Data reduction to obtain G_{Ic} during crack propagation, forming the R-curve

The following section provides two methods to determine the R-curve of a CFRP SENB specimen. Both methods will require a method to determine the Crack Tip Position (CTP).

11.1 Crack length monitoring

For the calculation of G_{Ic} during crack propagation, and determining an R-curve for the material. In addition to the force, displacement and time, the crack length a shall be monitored as well during crack propagation. The monitoring of this parameter is precise activity. To obtain a precise result for G_{Ic}, and to obtain a precise R-cure, the crack length a shall be measured with a precision of 0.2mm or less.

An implementation in LabVIEW with a precision of 0.1mm and high repeatability for determining the CTP using a camera is presented in **Appendices B** and **F**.

11.2 Method 1: R-curve determination by direct observation of the load, displacement and crack length

The ISO 13586 standard assumes all work put into the displacement of the system to be transferred into crack propagation, resulting in Equation (1) in section 6.2 of the standard. However, when reviewing the energy balance in the system, it follows that during crack propagation, not all energy dissipates at once at fracture initiation since residual stiffness is present.

The value of G_{Ic} can be determined by a cumulative area method. This method is presented in **Figure A.3b**. First, **Figure A.3a** presents the energies in intralaminar SENB testing. The area under the orange line in this figure represents the cumulative energy U_1 and is equal to the total work done by the loading rig given by **Equation (A.1)**.

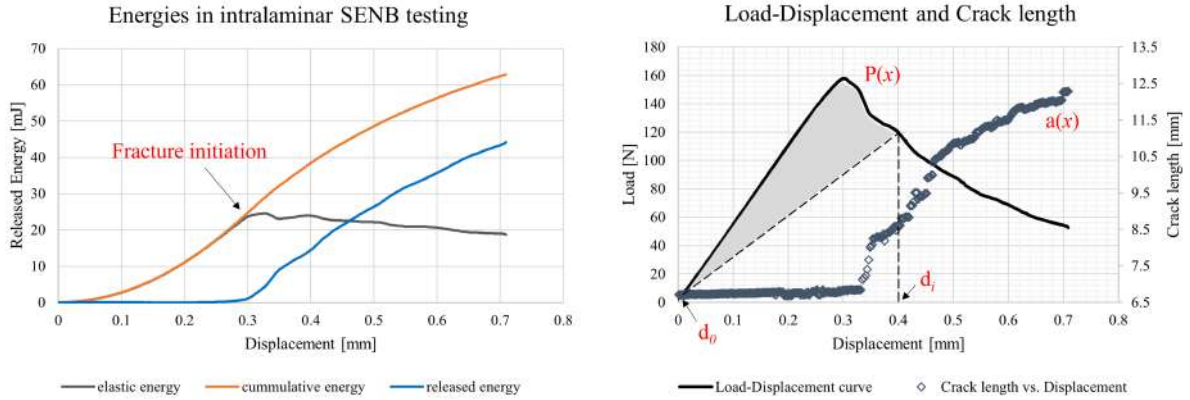

(a) Different Energies present in intralaminar SENB testing. Notice that released energy U_2 is >0 when crack propagation starts

(b) Force-Displacement plot with crack length on secondary y-axis. The grey area denotes the released energy U up to displacement d_i

Figure A.3: Energies in intralaminar SENB testing and Load-Displacement plot

$$U_1(d_i) = \int_{d_0}^{d_i} P(x)\,dx \approx \sum_{i=0}^{d_i-1} \left\{ (d_{i+1} - d_i) \left\{ P(d_i) + \frac{P(d_{i+1}) - P(d_i)}{2} \right\} \right\} \tag{A.1}$$

Then, the area under the grey line in **Figure A.3a** represents the elastic energy in the specimen (i.e., the energy stored in elastic deformation). **Equation (A.2)** yields the elastic energy U_3 at each displacement d_i.

$$U_3(d_i) = \frac{P(d_i)}{2}(d_i - d_0) \tag{A.2}$$

Finally, the cumulative released energy U_2 at displacement d_i by fracture of the material and subsequent crack propagation is equal to the area under the blue curve and given by **Equation (A.3)**.

$$U_2(d_i) = U_1(d_i) - U_3(d_i) \approx \sum_{i=0}^{d_i-1} \left\{ (d_{i+1} - d_i) \left\{ P(d_i) + \frac{P(d_{i+1}) - P(d_i)}{2} \right\} \right\} - \frac{P(d_i)}{2}(d_i - d_0) \tag{A.3}$$

The cumulative released energy between d_o and d_i is presented in **Figure A.3b** by the shaded area. The area of elastic energy within the same boundaries is presented by the area bound by the x-axis and the 2 dotted lines. Furthermore, an example of the crack propagation is presented by blue diamonds with values on the second y-axis.

The R-curve, can be obtained by plotting the cumulative released energy $U_2(d_i)$ against crack length $a(d_i)$ to obtain $U_2(a)$ as presented by the example in **Figure A.4**. Then, the R-curve is obtained by **Equation (A.4)**.

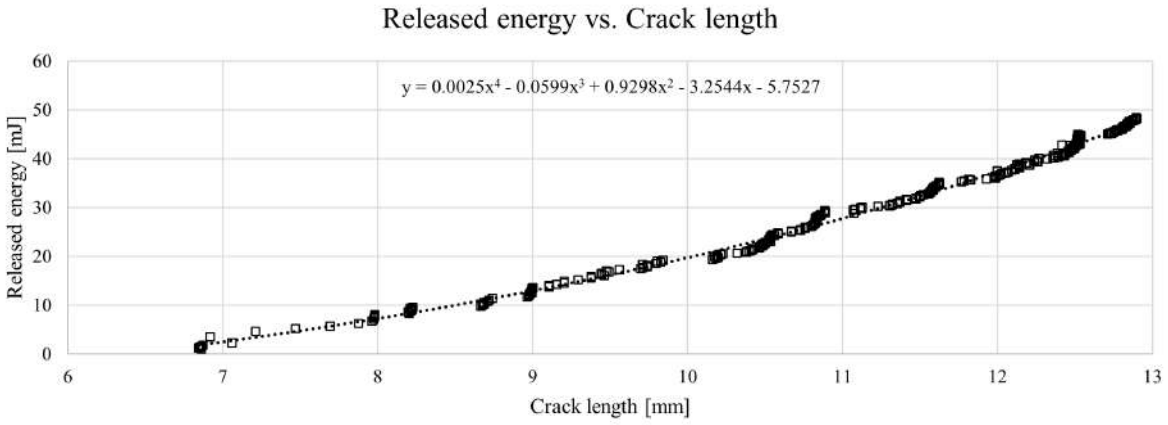

Figure A.4: The cumulative released energy U plotted over the crack length a

$$R(a) = \frac{1}{B}\frac{dU_2(a)}{da} = \frac{1}{B}U_2'(a) \tag{A.4}$$

The derivative $\frac{dU_2(a)}{da}$ can be obtained by a polynomial fit over $U_2(a)$ and taking the exact derivative. Furthermore, other promising results have been obtained by using a linear fit over a sliding window in the data and taking the derivative over this linear fit.

11.3 Method 2: R-curve determination by Corrected Beam Theory (CBT)

Another method to obtain the R-curve is by a Corrected Beam Theory (CBT). However, this method assumes linear elasticity and it should be noted that the method is valid for a SENB geometry where the $a < 0.8W$. For values of a larger than $0.8W$, the effect of excessive plastic deformation in the ligament width causes the R-curve to deviate from reality.

Figure A.5 displays the free body diagram of a SENB specimen. In the equations that will follow, the values of A, B, C, D, and E are the horizontal positions of the letters, measured from $A = 0$.

The compliance $C(a)$ at crack length a can be obtained by **Equation (A.5)**.

$$C(a) = \frac{u}{P} = \frac{PD^3I_2(a) - PB^3I_1 - 11PD^3I_1 + 12D^2BI_1 - 24PD^2EI_1}{12E_yI_1I_2(a)P} \tag{A.5}$$

The derivative of **Equation (A.5)** is obtained by **Equation (A.6)**.

$$\frac{dC(a)}{da} = -3\frac{24D^2E + 11D^3 - 12BD^2 + B^3}{B^*E_y(a-W)^4} \tag{A.6}$$

Finally, the energy release rate G_{Ic} as function of crack length is given by **Equation (A.7)**.

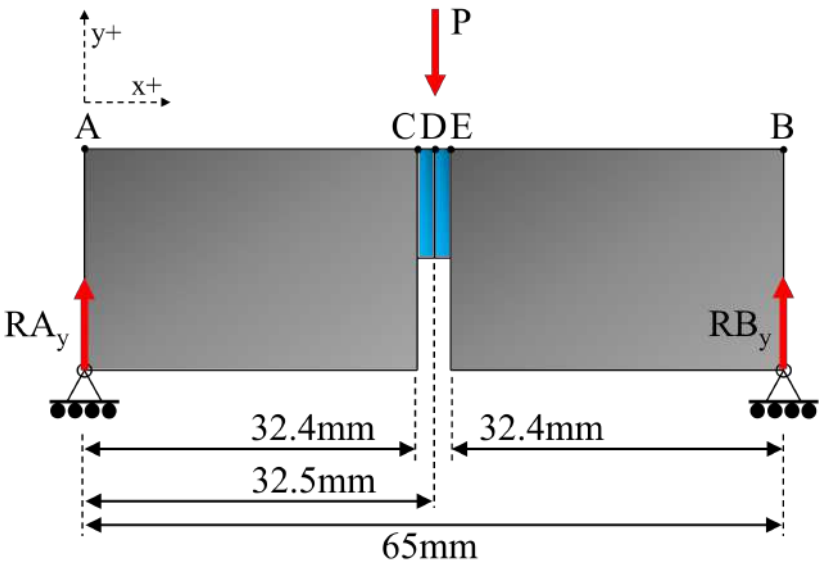

Figure A.5: Free body diagram of a SENB specimen

$$R(a) = G(a) = \frac{P^2}{2B^*}\frac{dC}{da} = -\frac{3P^2\left(24D^2E + 11D^3 - 12BD^2 + B^3\right)}{2B^{*2}E_y(a-W)^4} \tag{A.7}$$

11.4 Reporting

After testing, the ISO 13586 standard can be followed regarding the parameters and measurements to be reported. Furthermore, it is recommended to document the R-curves and load-displacement curves. Lastly, a standard deviation on the results shall be added such that the precision of the results is known.

B | Crack tip tracking algorithm

B-1 Crack tip tracking LabVIEW algorithm

To be able to accurately determine the crack length a during testing of a SENB specimen, it has been chosen to design a computer algorithm in LabVIEW. NI instruments' LabVIEW provides a useful package called NI Vision. This package enables the user to perform real time image processing in which each acquired camera frame is analysed in a way the user specifies in the algorithm, enabling real time measurement of the crack tip position en subsequently the crack length. The steps taken in this algorithm will be explained here. This section will furthermore explain the crack tip tracking algorithm and the experimental methods used to optimize this algorithm. For the algorithm's user-interface, the author refers the reader to **Appendix F**.

1.1 Crack tip position acquisition

The calculation of the crack tip position and subsequent crack length is done is 10 steps.

1. First, the algorithm acquires a still image ready for image processing from a live video feed of the side of the specimen as depicted in **Figure B.1**

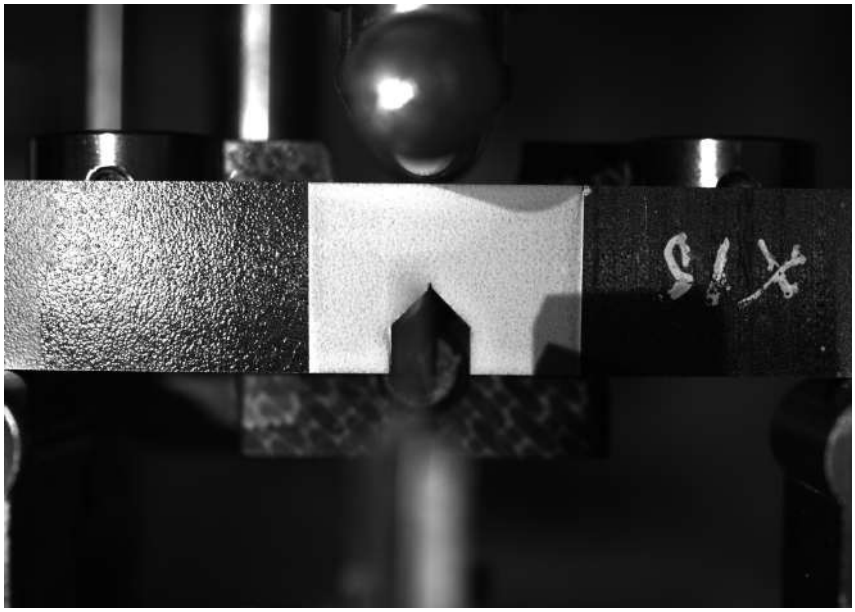

Figure B.1: Still image acquired for live video feed, prior to image processing

2. The subVI *IMAQ Find Edge 2*, detects the top and bottom of the specimen by abrupt changes in contrast in a previously defined Region of Interest (ROI). An ROI is simply a selected area in the total visible area by the camera. This sub-function has several parameters to detect the edge in the correct way, taking into account the lighting, contrast and camera resolution. The selection of this ROI is depicted in **Figure B.2** by the green box on the left.

3. Next, mathematical equations are determined for the tangents to both specimen sides. This is done by extracting the x- and y-coordinate in pixels of the first point and end point of each line. Next, calculating the gradient using $\frac{dy}{dx}$ and calculating c_i in the function $y = \frac{dy}{dx}x + c_i$ by substituting a known point on the tangent.

4. Since the specimen bends during the 3 point bend test, the angle of the top and bottom tangent changes during testing. Due to this phenomena, the distance cannot simply be calculated by taking

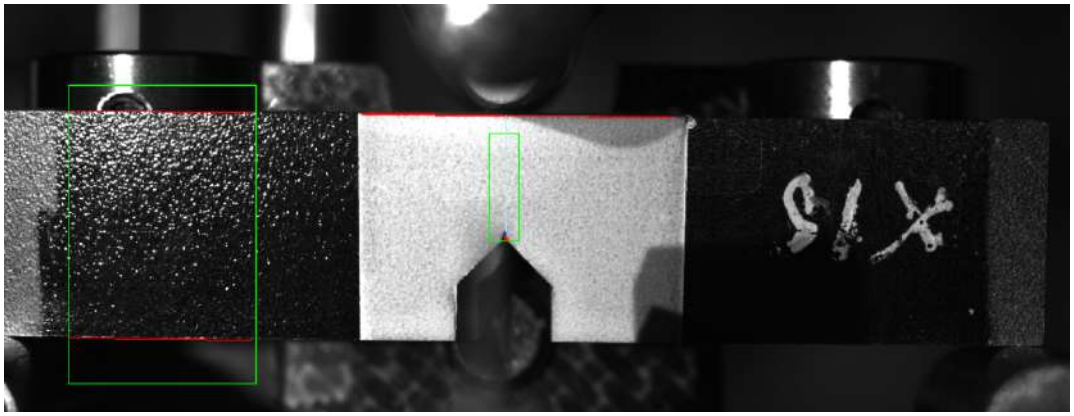

Figure B.2: Camera still live view, with overlay-ed ROIs, and active crack tip tracking

the distance between 2 y-coordinates of points on both tangents. The distance between two parallel lines, being the specimen height in pixels, is instead calculated by applying calculus. The formula for the distance between two parallel lines in pixels, using the 2 previously determined equations, is as in **Equation (B.1)**.

$$d = \frac{|c_2 - c_1|}{\sqrt{1 + \left(\frac{\frac{dy_1}{dx_1} + \frac{dy_2}{dx_2}}{2}\right)^2}} \tag{B.1}$$

In this equation, subscript $i = 1 \vee i = 2$ refers to the equation of the tangent to the top of the specimen: $y_i = \frac{dy_i}{dx_i}x + c_i$, where $i = 1$ for the tangent to the top of the specimen and $i = 2$ for the tangent to the bottom of the specimen. This step is visualized in **Figure B.3**.

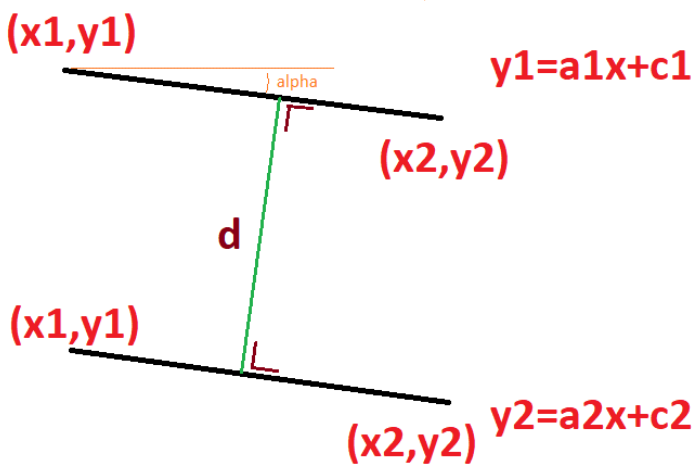

Figure B.3: Visualization of specimen height calculation with use of **Equation (B.1)**.

5. Next, in two previously defined extra ROIs situated at the top of the specimen, another 2 tangents are detected using the same method as described in step 1. Both ROIs are selected such that the region ends at the approximate point of loading. The selection of these ROIs is depicted in **Figure B.2** by the green boxes on top of the specimen. Then when the tangents are fitted, the y-coordinates of the tangents at the end of the ROIs, thus close to point of loading, are averaged. This results in the y-coordinate of the point of indentation/loading.

6. In another previously defined ROI, reaching from the v-notch and cut pre-crack initiation to just below the top of the specimen, encapsulating the area to be cracked, the crack itself is detected. The ROI does not reach the top of the specimen, since it has been found that a crack does barely propagate in the top region, caused by increased compliance. In this ROI, the *IMAQ Rake 3* subVI searches from left to right for difference in contrast. The option 'rising edges' is selected, prompting the function to search for a sequence of points where the contrast changes from black to white in the ROI. Then all these points of changing contrast are overlayed on the actual image, resulting in the crack line. The detection and overlay of points is presented in **Figure B.4**. This subVI/sub-algorithm can be tweaked to accommodate for differences in lighting, contrast, image quality and resolution, thus enabling it to fit the exact conditions when a new specimen is placed.

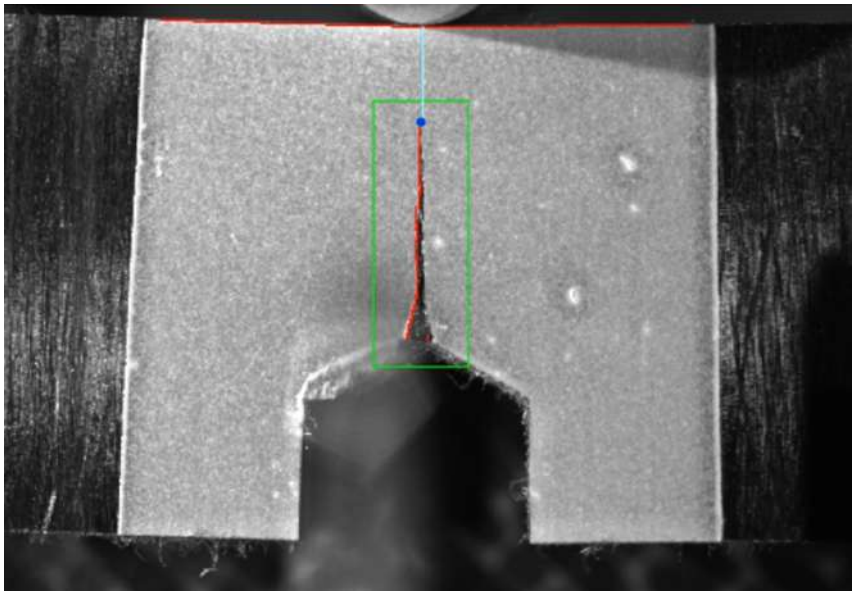

Figure B.4: Overlay-ed points detected as crack (red), and CTP (blue)

7. In the array of all these found points, the y-coordinates are extracted and the point with the lowest y-coordinate is selected as the y-value in pixels of the Crack Tip Position (CTP). This, since the y-axis of an image is flipped with respect to a normal xy-plot.

8. The ligament width in pixels is then defined as the y-coordinate of the CTP in pixels minus the y-coordinate of the loading point in pixels, explained in step 5.

9. Finally the crack length of the specimen is then the distance measured in step 5, being the specimen height in pixels, minus the ligament width in pixels in step 8. This results in the distance in pixels from the bottom of the specimen to the CTP.

10. To convert this distance in pixels to a value in real world coordinates (i.e. millimeters), a camera and lens distortion correction needs to be applied. This since the used camera lens has a barrel distortion. A simple $\frac{mm}{px}$ ratio does not suffice since the correction to be applied in case of a barrel distortion is not constant but dependent on the position in the captured frame. Therefore, the function *IMAQ Convert Pixel to Real World* is used, where a barrel distortion correction is applied. This function returns the real world distance, being the actual crack length. More on this barrel distortion correction can be found in **Appendix 1.4**.

1.2 Contrast and CTP detection optimization

When detecting edges of the specimen and detecting a propagating crack, it is important to ensure high contrast differences between the side of the specimen and the crack itself. This, such that the crack propagation algorithm does not mistake a non-crack pixel with a crack itself. In short, it can be said that a higher contrast eases the detection of a crack and enables the use of a lower threshold in whether a pixel is detected as a crack or not. In essence, one would like the specimen to be as light as possible and the crack to be as dark as possible or vice versa. However, in reality, this is a challenge.

The CF/LMPAEK material has a dark finish itself, thus making crack detection without any coating or such a contrast layer really difficult. Several methods have been tried to ensure proper contrast between the specimen and the crack itself.

1. First, the lighting conditions have been altered to try and create a reflection on the flat surface of the specimen. However, this proved quite difficult. An external light source has been placed at a very narrow angle of attack with the specimen, directly in front of the specimen and as a global illumination. Neither of the methods proved useful in bettering the contrast between the specimen and the crack itself.

2. Next, Tipp-Ex (typewriter correction fluid) has been applied on a specimen. Typp-ex has a very brittle nature when dry which provides a perfect coating when trying the follow the crack propagation. When, for example, an elastic or relatively elastic paint is applied, it might not tear/fracture along with the extent of the specimen itself. All one would be measuring in such an instance is the crack propagation through a layer of paint.

   The applied Typp-Ex layer provided better contrast results than trying to create better contrast just by changing the lighting. However, Typp-ex is viscous and thick when applied to the specimen. When trying to create a smooth layer on the side of the specimen, the Typp-ex needs to be diluted with either water or isopropanol. Otherwise a rough layer is applied, resulting in unwanted shadows, subsequently mistakenly detected as cracks.

3. Finally, several spray paints are applied on the specimen. Previous research has shown that matte white paint provided the best surface finish and results. Although matte white paint is more elastic than Typp-ex, it proves to follow the extent of crack propagation quite well, that is, at least not significantly deviating from the extent of crack propagation when using Typp-ex. Next to that, it can be applied in a very even and smooth thin layer, since it can be spray painted on the specimen. For example, **Figure B.5** depicts the difference in surface neatness detected by the camera between using TyppEx or matte white spray paint.

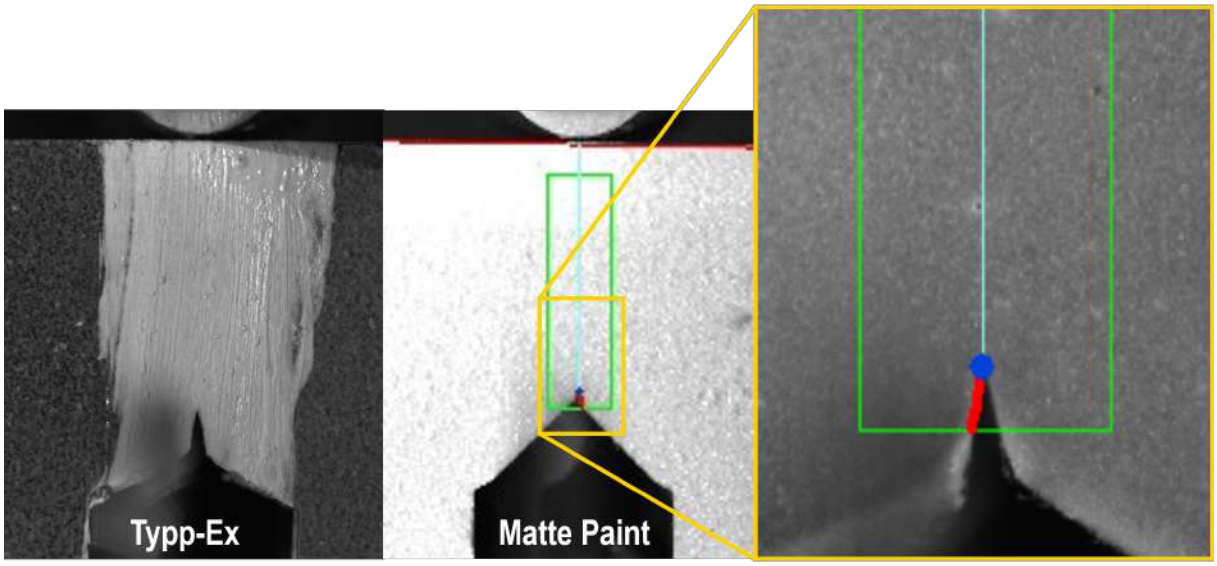

Figure B.5: Direct comparison between surface smoothness when using Typp-ex and matte white spray paint

To find the best combination of tracking sensitivity, lighting, and applied contrast layer, the crack propagation plots are analyzed. They provide a direct feedback whether a combination of parameters work or not and therefore these graphs are chosen as a measurement of what works best. **Figure B.6** shows a direct comparison of the crack propagation graph of 5 different combinations of tracking sensitivity, lighting and contrast layer. As can be seen in the plot of Specimens X2, X4, and X5, the tracking is not smooth (i.e., the plot skips values vertically). The skipping of crack length vertically is a results of a combination of parameters that made it difficult for the algorithm to track the crack propagation. What could be seen with the naked eye, was that the crack propagated already before the software was able to keep up with the crack. As soon as the crack opened a bit more, the detected crack tip position would suddenly jump to the next point, indicating a certain sensitivity threshold either in contrast or tracking function parameters.

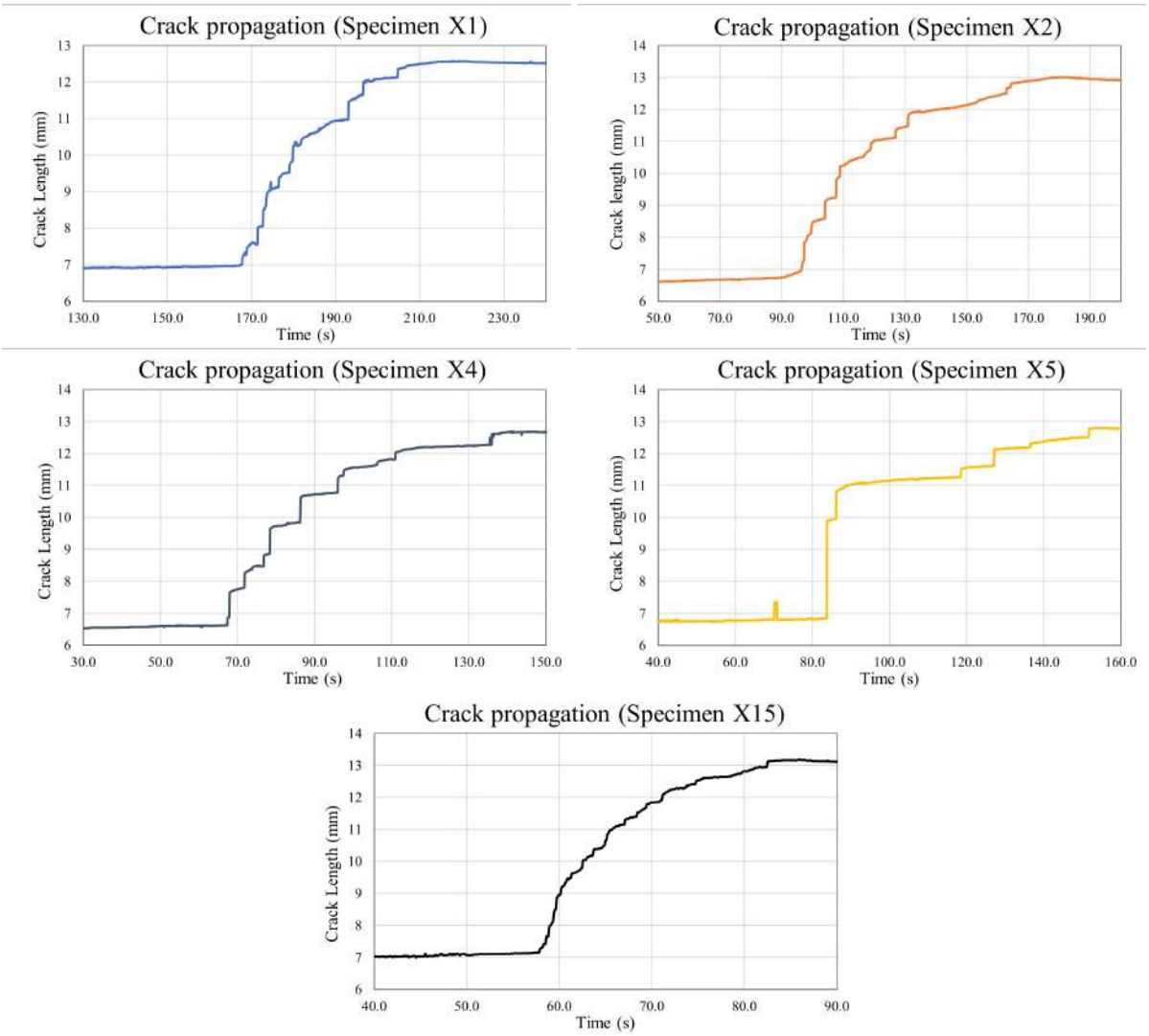

Figure B.6: Direct comparison of crack propagation tracking results of specimens X1, X2, X4, X5, and X15

As can be seen in **Figure B.6**, the combination of more sensitive tracking, general lighting and a thicker layer of matte white paint provided the best results. furthermore, the tracking settings have been altered after each test and with specimen X15, the 14th iteration, the results were smooth and consistent enough such that the settings were adopted for the Round-Robin tests as well. Concluding, it can be said that the matte white paint, proved to be the most successful in providing the best contrast difference between the specimen itself and the crack front. Therefore, every specimen from specimen X8 onward (as can be seen in **Table 3.5** in **Section 3.5**), including the Round-Robin specimens, has been tested with this method.

1.3 Regions of interest

When checking whether a certain pixel is a crack or not, the software makes use of prior defined Regions Of Interest (ROIs). An ROI is simply a selected area in the total visible area by the camera. When selecting a smaller ROI to perform the image processing functions in, it results in less computing power needed and a faster algorithm. It is therefore paramount to select the needed ROIs as small as possible. The Different ROIs, as reported in **Appendix 1.1** are depicted in **Figure B.2**. As can be seen, these are indeed selected as small as possible.

1.4 Lens and camera correction

As mentioned earlier, the algorithm needs to compensate for the phenomenon known as barrel lens distortion to be able to actually perform measurements in real world units. Barrel distortion causes the acquired image to be warped. When performing accurate measurements, this phenomenon needs to be countered. After setting up the correct distance between the lens and the specimen, this distance is measured and taken as a starting point for calibration. The calibration is done by taking a single picture of an 17 by 8 dot pattern, equally spaced by 4 millimeters. Then in LabVIEW itself, using the *Vision Assistant*, the software calculates the offset for each point from its real world position, with the given equal spacing of 4 mm. This offset for each point is visually shown in **Figure B.7** by the red arrows. By doing this, a calibrated image can be exported that contains the calibration information. In the actual algorithm itself, this calibrated image, containing the calibration information, can be loaded in and applied to a live acquired image. However, calibrating and transforming each image that enters the algorithm is a CPU heavy task and will drastically decrease the amount of frames the algorithm can handle per second and subsequently decrease performance. With live crack tip tracking, this is unwanted. Therefore it has been chosen to not correct the image at all.

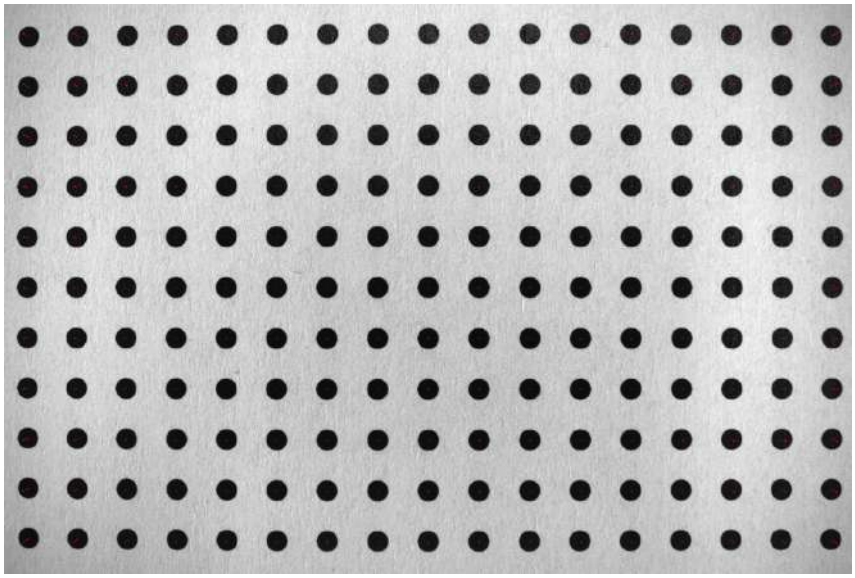

Figure B.7: Point-by-point offset camera correction

Instead, the measurements that the algorithm performs are converted from pixel values to real world units, eliminating the need to correct each single frame. This since the only necessary conversion has to be applied to the measurements. The pixel values are converted to real world units before calculating the distance between them since a distance itself contains no information about its position on an acquired frame, thus it is unknown what the calibration should be. Finally, after converting pixel values, containing a x- and y-coordinate, by the SubVI *IMAQ Convert Pixel to Real World*, the distances are measured and displayed.

1.5 CTP Accuracy and precision

When measuring the crack length of the specimen, the accuracy of these measurements plays a role as well. The lens correction itself and the measurements in the software have an accuracy and precision. This section will provide a worst case error analysis on performed measurements. The list below states all reasonably possible errors:

1. The applied lens correction, using point distortion correction, has a mean error of 0.0149mm

with a standard deviation of $9.099 * 10^{-5}$mm (calculated by LabVIEW). The maximum error is 0.0154mm.

2. The lens distance is set at 105mm measured with a caliper having a precision of 0.05mm. This is the same distance where the barrel distortion correction was applied. Afterwards, the measured distance from top to the bottom of the specimen, after applying the lens distortion correction, was displayed. Then the camera was moved in position until the displayed specimen height agreed with the measured specimen height to the nearest 0.075mm.

3. The detection of crack tip position seemed to be precise up to a pixel. What was observed is that the CTP would switch between 2 pixels due to them being very similar in contrast. Then, the precision of the CTP measurement itself can be set to ± 1 pixel. The field of view at lens distance of 105mm is 55.8x37.2mm [64]. At this distance, each pixel corresponds to $\frac{55.8mm}{5536px.} = 0.010\frac{mm}{px}$ (here 5536 is the number of horizontal pixels on the sensor), meaning the accuracy of ± 1 pixel translates to an accuracy of $\pm$0.01mm pixel.

4. Finally, the accuracy of the CTP has everything to do with the assumption that the fracture through the paint layer occurs at the same time as the fracture on the specimen itself. No visible excessive strain strain due to a ductile paint layer, or visible lagging has been observed. Therefore, it has been assumed the paint fractures in a brittle way, following the CTP. It is practically impossible to determine what the accuracy might be.

The final cumulative precision of a measured CTP position is: 0.0154mm + 0.075mm + 0.01mm $\approx$ 0.1mm.

B-2 Data output and further usage

After performing a test on a specimen, the data is saved in an MS excel file and sorted neatly by elapsed time [s], force [N], displacement [mm] and crack length [mm] in different columns. The four columns containing data can be copied to another Excel sheet where the Energy Release Rate G_{Ic} and Fracture Toughness K_{Ic} are automatically calculated for the specimen adhering to the LEFM method. This by following the ISO 13586 standard's procedure and the R-curve is calculated by means of the area method as described in **Section 3.6**. Furthermore, the live view itself can be recorded for later use. The data flow in the crack length determination process is presented in **Figure B.8**.

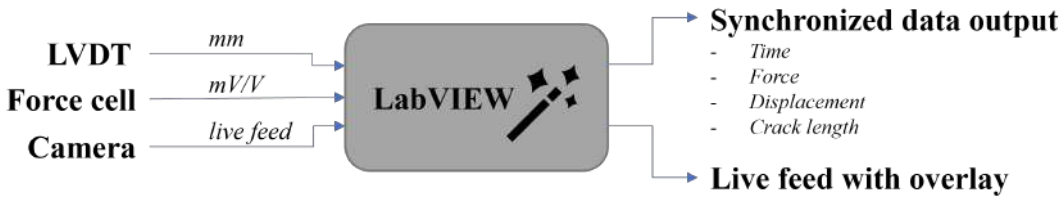

Figure B.8: Data flow in the crack length determination process

E | Preliminary and Round-Robin specimen dimensions

E-1 Preliminary specimen dimensions

Table E.1 presents the dimension of the Round-Robin specimens. Here the dimensions are in millimeter unless indicated otherwise.

Table E.1: Preliminary specimen dimensions

Specimen	ID	pre-crack	w_1	w_2	h_1	h_2	a_0 front	a_0 back	a_0 avg.	$W_1 - a_0$	$W_2 - a_0$	$W_{avg.}$	h_{avg}	$W - a_0$ avg.	NTD [µm]
X1	1	0.800	14.403	14.41	4.37	4.274	6.474	6.522	6.498	7.905	7.912	14.4065	4.322	7.9085	15
X2	2	0.800	14.344	14.369	4.374	4.291	6.36	6.36	6.36	7.984	8.009	14.3565	4.3325	7.9965	14
X3	3	0.800	14.32	14.36	4.375	4.31	6.583	6.608	6.5955	7.7245	7.7645	14.34	4.3425	7.7445	19
X4	4	0.800	14.327	14.355	4.391	4.319	6.409	6.372	6.3905	7.9365	7.9645	14.341	4.355	7.9505	15
X5	5	0.800	14.325	14.360	4.397	4.333	6.38	6.39	6.385	7.94	7.975	14.3425	4.365	7.9575	7
X6	6	0.800	14.342	14.383	4.392	4.339	6.548	6.532	6.54	7.802	7.843	14.3625	4.3655	7.8225	20
X7	7	0.800	14.328	14.365	4.405	4.34	6.413	6.426	6.4195	7.9085	7.9455	14.3465	4.3725	7.927	23
X8	8	0.100	14.352	14.365	4.41	4.38	6.626	6.568	6.597	7.755	7.768	14.3585	4.395	7.7615	8
X9	9	0.100	14.355	14.365	4.405	4.375	6.648	6.658	6.653	7.702	7.712	14.36	4.39	7.707	8
X10	10	0.200	14.33	14.365	4.405	4.375	6.743	6.753	6.748	7.582	7.617	14.3475	4.39	7.5995	20
X11	11	0.550	14.34	14.375	4.398	4.378	7.042	7.074	7.058	7.282	7.317	14.3575	4.388	7.2995	30
X12	12	0.400	14.355	14.38	4.39	4.375	7.001	6.998	6.9995	7.3555	7.3805	14.3675	4.3825	7.368	20
X13	13	0.400	14.34	14.375	4.389	4.375	6.949	6.99	6.9695	7.3705	7.4055	14.3575	4.382	7.388	13
X14	14	0.200	14.335	14.36	4.385	4.37	6.814	6.806	6.81	7.525	7.55	14.3475	4.3775	7.5375	16
X15	15	0.200	14.342	14.35	4.382	4.367	6.764	6.724	6.744	7.598	7.606	14.346	4.3745	7.602	14
X16	16	0.200	14.325	14.371	4.369	4.35	6.679	6.718	6.6985	7.6265	7.6725	14.348	4.3595	7.6495	14
X17	17	0.100	14.345	14.385	4.387	4.354	6.604	6.597	6.6005	7.7445	7.7845	14.365	4.3705	7.7645	4
X18	18	0.100	14.322	14.361	4.37	4.333	6.497	6.544	6.5205	7.8015	7.8405	14.3415	4.3515	7.821	4
X19	19	0.000	14.328	14.348	4.37	4.327	6.5	6.5	6.5	7.828	7.848	14.338	4.3485	7.838	1000
								Average	**6.636**	**7.704**	**7.732**	**14.354**	**4.367**	**7.718**	
								σ	**0.196**	**0.190**	**0.191**	**0.010**	**0.015**	**0.190**	
								%STD	**2.96%**	**2.47%**	**2.47%**	**0.07%**	**0.34%**	**2.47%**	

E-2 Round Robin specimen dimensions

Table E.2 presents the dimension of the Round-Robin specimens. Here the dimensions are in millimeter unless indicated otherwise.

Table E.2: Round-Robin specimen dimensions

Specimen	ID	w_1	w_2	w_3	h_1	h_2	h_3	a_0 front	a_0 back	a_0 avg.	$w_{avg.}$	$h_{avg.}$	l	NTD front [µm]	NTD back [µm]
A2	1	14.017	14.040	14.052	4.295	4.293	4.297	6.628	6.628	6.628	14.036	4.295	71.750	6.500	10.200
A13	2	14.073	14.076	14.097	4.298	4.294	4.294	6.667	6.665	6.666	14.082	4.295	71.520	8.700	11.300
A23	3	14.043	14.089	14.118	4.282	4.297	4.282	6.710	6.732	6.721	14.083	4.287	71.000	7.100	?
B2	4	14.059	14.060	14.069	4.289	4.288	4.279	6.643	6.694	6.669	14.063	4.285	70.100	9.300	8.100
B13	5	14.079	14.086	14.086	4.294	4.301	4.311	6.715	6.671	6.693	14.084	4.302	70.080	5.600	6.600
C2	6	14.053	14.046	14.044	4.289	4.290	4.273	6.622	6.668	6.645	14.048	4.284	70.080	9.800	?
C13	7	14.065	14.082	14.084	4.317	4.329	4.331	6.671	6.690	6.681	14.077	4.326	70.060	7.500	10.600
C23	8	14.073	14.075	14.079	4.294	4.290	4.298	6.686	6.738	6.712	14.076	4.294	70.440	12.500	12.700
D2	9	14.055	14.050	14.020	4.273	4.269	4.280	6.647	6.667	6.657	14.042	4.274	70.140	8.200	7.100
D13	10	14.071	14.055	14.036	4.328	4.323	4.320	6.700	6.691	6.696	14.054	4.324	70.120	9.600	?
									Average	**6.677**	**14.064**	**4.297**	**70.529**	**8.480**	
									σ	**0.029**	**0.018**	**0.017**	**0.652**	**1.973**	
									%STD	**0.44%**	**0.13%**	**0.39%**	**0.92%**	**23.27%**	

F | LabVIEW user-interface

F-1 Front panel

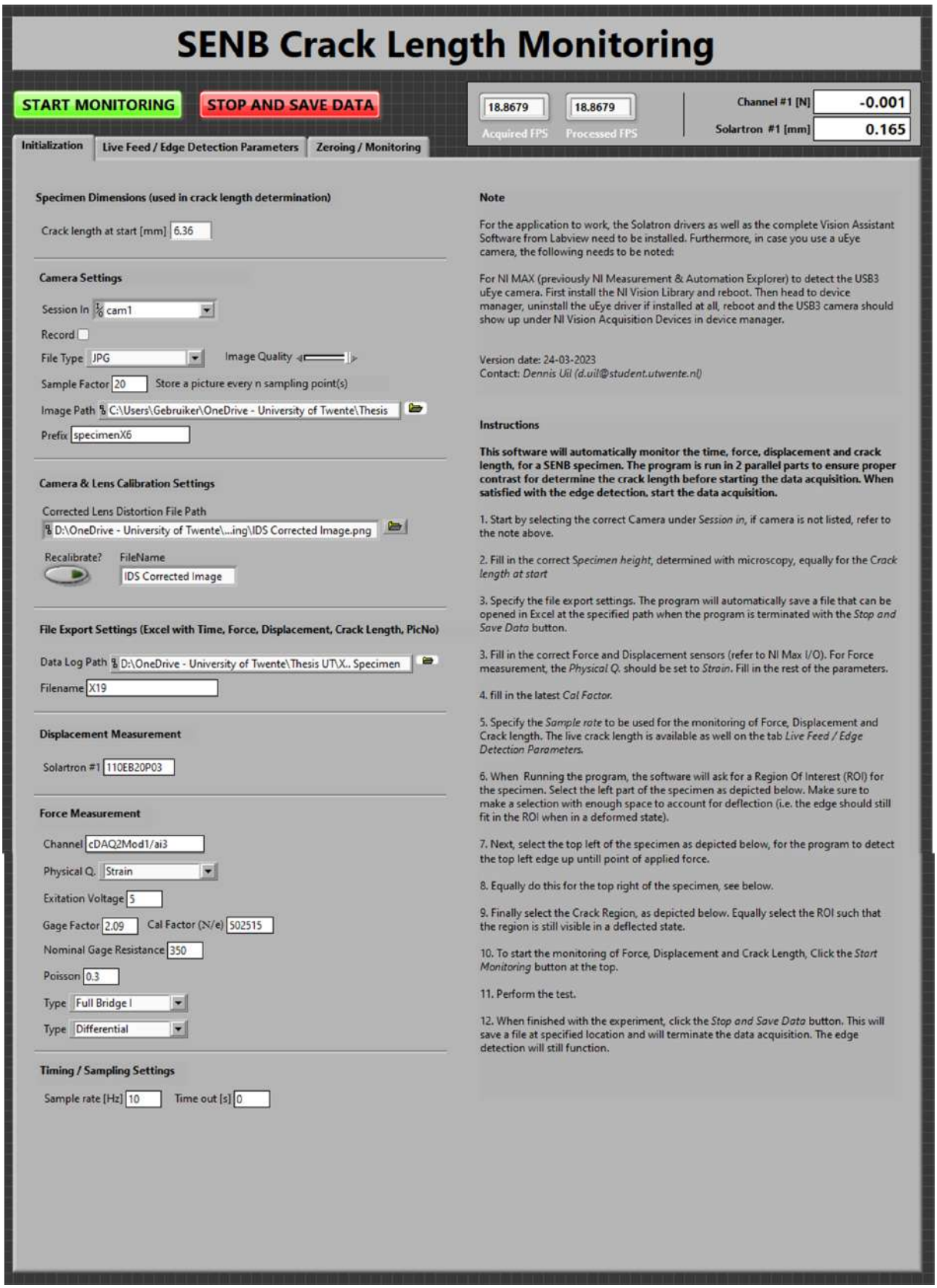

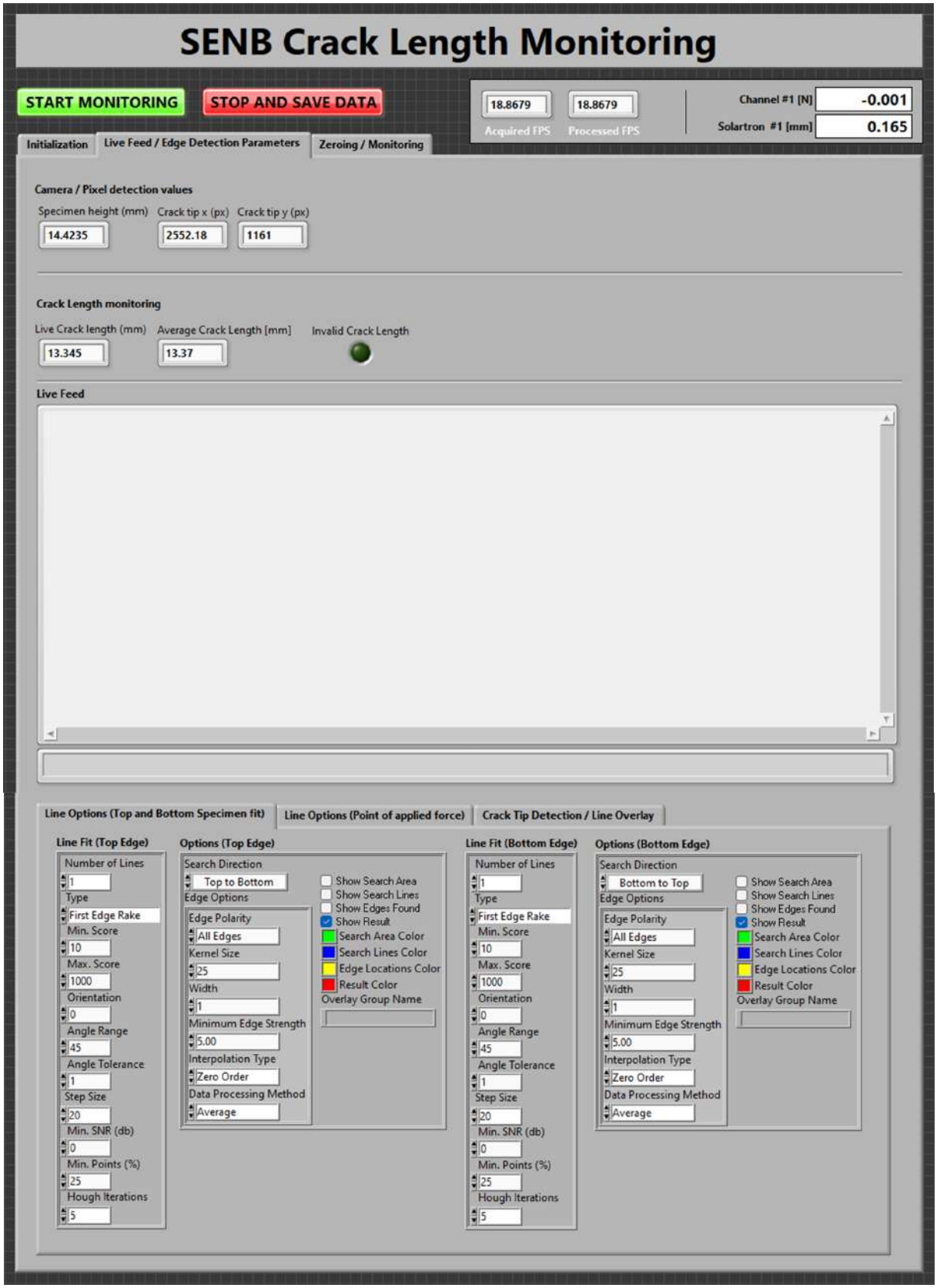
SENB Crack Length Monitoring
START MONITORING
STOP AND SAVE DATA
18.8679
Acquired FPS
18.8679
Processed FPS
Channel #1 [N]
-0.001
Solartron #1 [mm]
0.165
Initialization
Live Feed / Edge Detection Parameters
Zeroing / Monitoring
Camera / Pixel detection values
Specimen height (mm)
14.4235
Crack tip x (px)
2552.18
Crack tip y (px)
1161
Crack Length monitoring
Live Crack length (mm)
13.345
Average Crack Length [mm]
13.37
Invalid Crack Length
Live Feed
Line Options (Top and Bottom Specimen fit)
Line Options (Point of applied force)
Crack Tip Detection / Line Overlay
Line Fit (Top Edge)
Number of Lines
1
Type
First Edge Rake
Min. Score
10
Max. Score
1000
Orientation
0
Angle Range
45
Angle Tolerance
1
Step Size
20
Min. SNR (db)
0
Min. Points (%)
25
Hough Iterations
5
Options (Top Edge)
Search Direction
Top to Bottom
Edge Options
Edge Polarity
All Edges
Kernel Size
25
Width
1
Minimum Edge Strength
5.00
Interpolation Type
Zero Order
Data Processing Method
Average
Show Search Area
Show Search Lines
Show Edges Found
Show Result
Search Area Color
Search Lines Color
Edge Locations Color
Result Color
Overlay Group Name
Line Fit (Bottom Edge)
Number of Lines
1
Type
First Edge Rake
Min. Score
10
Max. Score
1000
Orientation
0
Angle Range
45
Angle Tolerance
1
Step Size
20
Min. SNR (db)
0
Min. Points (%)
25
Hough Iterations
5
Options (Bottom Edge)
Search Direction
Bottom to Top
Edge Options
Edge Polarity
All Edges
Kernel Size
25
Width
1
Minimum Edge Strength
5.00
Interpolation Type
Zero Order
Data Processing Method
Average
Show Search Area
Show Search Lines
Show Edges Found
Show Result
Search Area Color
Search Lines Color
Edge Locations Color
Result Color
Overlay Group Name

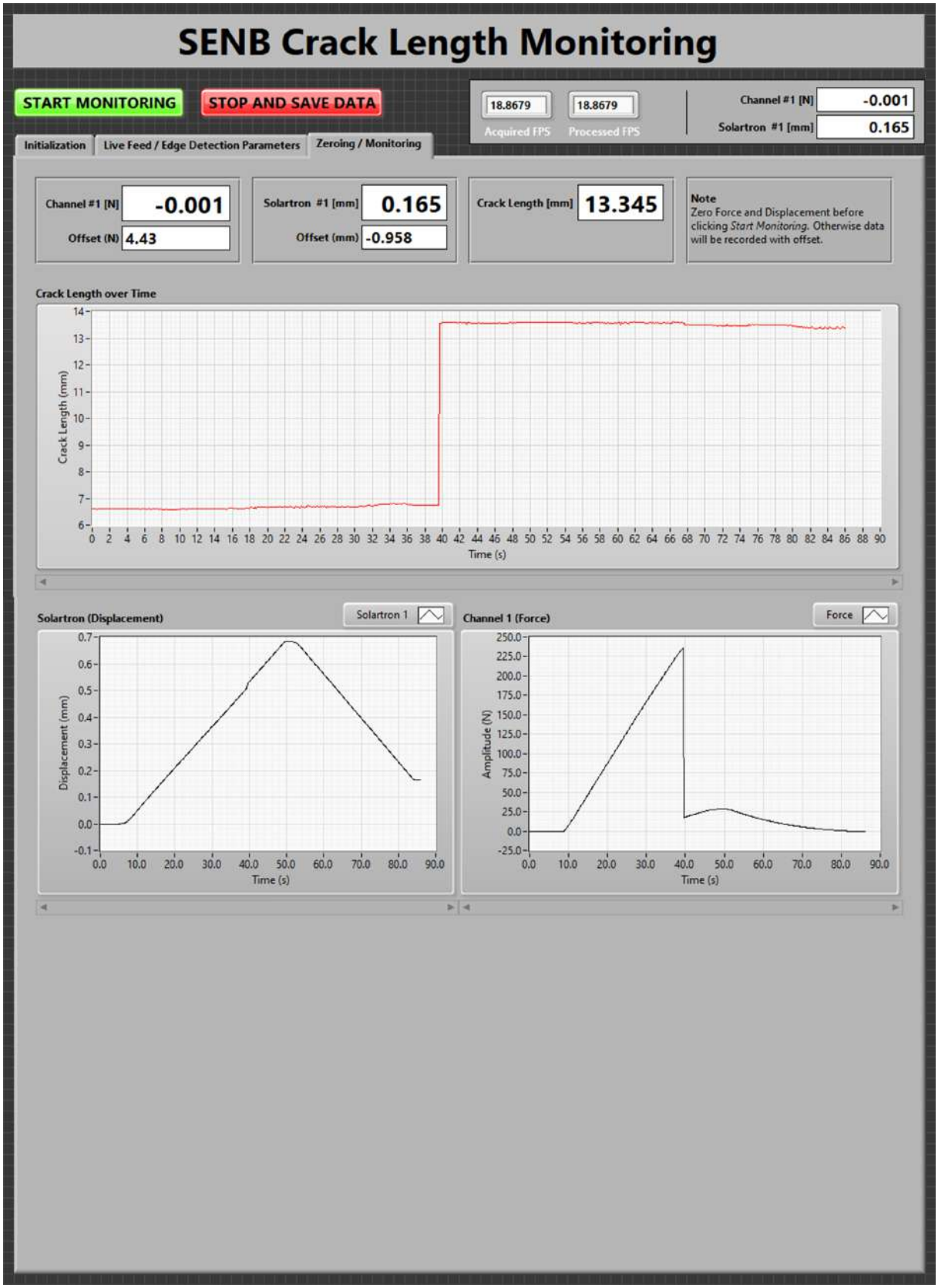
SENB Crack Length Monitoring
START MONITORING
STOP AND SAVE DATA
18.8679
Acquired FPS
18.8679
Processed FPS
Channel #1 [N]
-0.001
Solartron #1 [mm]
0.165
Initialization
Live Feed / Edge Detection Parameters
Zeroing / Monitoring
Channel #1 [N]
-0.001
Offset (N)
4.43
Solartron #1 [mm]
0.165
Offset (mm)
-0.958
Crack Length [mm]
13.345
Note
Zero Force and Displacement before clicking Start Monitoring. Otherwise data will be recorded with offset.
Crack Length over Time
Crack Length (mm)
Time (s)
Solartron (Displacement)
Solartron 1
Displacement (mm)
Time (s)
Channel 1 (Force)
Force
Amplitude (N)
Time (s)

G | Error calculation

G-1 Error calculation on parameters

Table G.1 presents several parameters with their precision. The right side of the table states what causes the precision.

Table G.1: Precision ranges for various parameters used in calculations

Parameter	Symbol	precision ±	Unit	Cause
Force	P	0.020	%	Load cell precision
	sum	**0.020**	**N**	
Notch tip diameter	NTD	0.010	mm	Difficulty determining CTP
		0.003	mm	Microscope calibration
	sum	**0.013**	**mm**	
Initial crack length	a_0	0.010	mm	Difficulty determining a_0
		0.003	mm	Microscope calibration
	sum	**0.013**	**mm**	
Specimen width	h	0.001	mm	Micrometer precision
		0.005	mm	Measurement precision
	sum	**0.006**	**mm**	
Specimen height	W	0.001	mm	Micrometer precision
		0.005	mm	Measurement precision
	sum	**0.006**	**mm**	
Displacement	δ	0.0001	mm	LVDT precision
		0.00005	mm	LVDT resolution
	sum	**0.00015**	**mm**	
Linear fit on displ. corr.	-	0.500	%	R^2 value
	sum	**0.500**	**%**	
Stiffness fit (CC)	-	0.500	%	R^2 value
	sum	**0.500**	**%**	
Measured crack length	a	0.100	mm	Camera/lens distance + distortion correction
	sum	**0.100**	**mm**	
Poly. fit $\frac{dU_2}{da}$	-	0.500	%	R^2 value
	sum	**0.500**	**%**	
Span (B in CBT)	S	0.050	mm	Caliper precision
	sum	**0.050**	**mm**	

G-2 Sample error calculation on specimen A2

Table G.2 table will provide a sample calculation of the cumulative precision error on the mentioned parameters. The standard deviation σ, relative standard deviation $\%STD$ and the standard error SE are given.

Table G.2: Cumulative error calculation on specimen A2

Parameter	Symbol	Actual value	Min. value	Max. value	Unit	STD	%STD	SE
Specimen width	h	4.295	4.289	4.301	mm	**8.485E-03**	**0.198%**	**2.683E-03**
Specimen height	W	14.036	14.030	14.042	mm	**8.485E-03**	**0.060%**	**2.683E-03**
Maximum force	F	157.765	157.734	157.797	N	**4.462E-02**	**0.028%**	**1.411E-02**
a_0/w	$\alpha(a_0/W)$	0.472	0.471	0.473	-	**1.595E-03**	**0.338%**	**5.045E-04**
A	-	31.410	31.195	31.627	-	**3.052E-01**	**0.972%**	**9.650E-02**
$dA/d\alpha$	-	191.293	190.006	192.592	-	**1.828E+00**	**0.956%**	**5.782E-01**
Energy correction factor	$\phi(a_0/w)$	0.262	0.261	0.262	-	**9.054E-04**	**0.346%**	**2.863E-04**
Displacement at break	δ_b	0.965	0.965	0.965	mm	**2.121E-04**	**0.022%**	**6.708E-05**
Specimen stiffness fit	-	0.589	0.586	0.589	mm	**2.071E-03**	**0.352%**	**6.549E-04**
Setup stiffness fit	-	4.660E-04	4.637E-04	4.660E-04	mm/N	**1.639E-06**	**0.352%**	**5.184E-07**
zero-ed displ. at break	δ_{b0}	0.376	0.376	0.379	mm	**2.177E-03**	**0.578%**	**6.884E-04**
corrected displ. at break	δ_{b0c}	0.303	0.303	0.306	mm	**2.456E-03**	**0.811%**	**7.768E-04**
Energy to break	W_b	24.982	24.970	25.317	mJ	**2.453E-01**	**0.982%**	**7.756E-02**
Geometry correction factor	$f(a_0/W)$	9.770	9.736	9.803	-	**4.736E-02**	**0.485%**	**1.498E-02**
Uni-axial tensile stress	σ_y	90.000	89.550	90.450	MPa	**6.364E-01**	**0.707%**	**2.012E-01**
Span	S	65.000	64.950	65.050	mm	**7.071E-02**	**0.109%**	**2.236E-02**
Change of U_2 over a at a_0	$\frac{dU_2(a_0)}{da}$	3.670	3.667	3.719	J/m^2	**3.655E-02**	**0.996%**	**1.156E-02**
Compliance at a_0	$C(a_0)$	0.258	0.270	0.247	mm/N	**1.648E-02**	**6.380%**	**5.212E-03**
Change of C over a at a_0	$\frac{dC(a_0)}{da}$	0.048	0.051	0.045	1/N	**3.872E-03**	**8.103%**	**1.224E-03**
Specimen stiffness	S	545.584	542.856	545.570	N/mm	**1.919E+00**	**0.352%**	**6.069E-01**
Notch tip diameter	NTD	6.500	6.487	6.513	µm	**1.838E-02**	**0.283%**	**5.814E-03**
Characteristic length	$\overline{r}$	1.240	1.203	1.289	mm	**6.053E-02**	**4.880%**	**1.914E-02**
Critical mode I ERR (initiation)	G_{Ic}	1583.799	1576.281	1611.889	J/m^2	**2.518E+01**	**1.590%**	**7.962E+00**
Critical stress intensity factor	K_{Ic}	3.029	3.013	3.045	$MPa\sqrt{m}$	**2.244E-02**	**0.741%**	**7.096E-03**
Resistance at initiation (method 1)	G_{Ic}	854.414	852.634	867.070	J/m^2	**1.021E+01**	**1.195%**	**3.228E+00**
Resistance at initiation (method 2)	G_{Ic}	1028.910	1014.470	1054.730	J/m^2	**2.847E+01**	**2.767%**	**9.002E+00**